REPORT DOCUMENTATION PAGE	Form Approved OMB No. 0704-0188

1. AGENCY USE ONLY *(Leave blank)*	2. REPORT DATE	3. REPORT TYPE AND DATES COVERED
	11.Jan.99	DISSERTATION

4. TITLE AND SUBTITLE
DIPOLE-DIPOLE INTERACTIONS IN A FROZEN RYDBERG GAS

5. FUNDING NUMBERS

6. AUTHOR(S)
CAPT LOWELL JOHN R

7. PERFORMING ORGANIZATION NAME(S) AND ADDRESS(ES)
UNIVERSITY OF VIRGINIA

8. PERFORMING ORGANIZATION REPORT NUMBER

9. SPONSORING/MONITORING AGENCY NAME(S) AND ADDRESS(ES)
THE DEPARTMENT OF THE AIR FORCE
AFIT/CIA, BLDG 125
2950 P STREET
WPAFB OH 45433

10. SPONSORING/MONITORING AGENCY REPORT NUMBER
FY99-58

11. SUPPLEMENTARY NOTES

12a. DISTRIBUTION AVAILABILITY STATEMENT
Unlimited distribution
In Accordance With AFI 35-205/AFIT Sup 1

12b. DISTRIBUTION CODE

13. ABSTRACT *(Maximum 200 words)*

14. SUBJECT TERMS	15. NUMBER OF PAGES
	16. PRICE CODE

17. SECURITY CLASSIFICATION OF REPORT	18. SECURITY CLASSIFICATION OF THIS PAGE	19. SECURITY CLASSIFICATION OF ABSTRACT	20. LIMITATION OF ABSTRACT

Dipole-Dipole Interactions in a Frozen Rydberg Gas

John Rubrecht Lowell
Maple Valley, WA

B.S., United States Air Force Academy, 1990
M.S., The Ohio State University, 1991

A Dissertation presented to the Graduate Faculty of the
University of Virginia in Candidacy for the Degree of
Doctor of Philosophy

Department of Physics

University of Virginia
May, 1998

_____

_____

_____

_____

Abstract

We investigate here the characteristics of energy resonant dipole-dipole interactions between Rydberg atoms in Magneto-Optical Trap. These resonant processes occur in a kinetic energy regime in which the atoms may be considered stationary over the time scale of the experiment. Coupled with the long range of the interactions considered, this leads to multi-atom interactions becoming non-negligible. A simple model is outlined to provide insight into the effects of these multi-atom interactions which lead to some interesting behaviors. Experiments which examine the broadening of the dipole-dipole resonances and observe the time dependence of the interaction signal are discussed. Examination of adiabatic character of population transfer caused by slewing across the resonance is discussed in another experiment, as is the scaling behavior of the resonance linewidths and on-resonant signal growth rates. We end by discussing an experiment which takes advantage of some of the characteristics of these interactions to measure the tensor polarizability of Rydberg states of Rb.

Acknowledgments

In the greater scheme of things, undertakings such as this are never achieved in a vacuum. As such, it is imperative to recognize the contributions of the people who served as the air which allowed this project to breathe.

First and foremost, I would like to thank my wife Elizabeth, whose patient and steadfast support has been with me during the late nights, the early mornings, and all the times in between. She pushed me to work when I needed to get something done, and to play when I needed to rest. I could not envision having done this without her. I would also like to thank my parents, Yogi and Elaine. They instilled in me a desire to push myself and a thirst for knowledge from a very young age, and have gently guided me along every stage of my journey here. I have also been inspired by the achievements of my siblings, Jeff, Margaret, and Rob. I couldn't ask for a better family.

I would also like to thank my other family, especially my mother-in-law, Carol. I am truly fortunate to have become a member a group of people as fun and supportive as this family. Thank you Libby, Andrew, Rick, Nancy, Emily, Doug, Noel, Lydia, Michael, Maisha, Byron, and MJ.

I was extremely fortunate to have worked with the large and talented group of people I have come to know here. These included my lab neighbors Warren Griffith and Mike Noel, with whom lunch turned into a daily discussion of whatever seemed interesting at the time, and from whom I learned a great deal about experimental physics. Bob Jones has served as a second advisor during my stay, helping solve numerous potential problems long before they occurred, and asking the difficult questions that I didn't want to answer. Other colleagues whose help aided my journey include Bobby Anderson (who built the trap the first time), Jim Veale, Duncan Tate, and Elena Murgu, as well as the other members of our atomic physics group: Michael, Lung, Victor, Matt, Tom, Jon, and Robert. I would also like to thank some of the past and present members of the department's support staff, including Rick Marshall, Sybil Hale, Lucille Mills, Bobby Floyd, and George Plum.

I would like to thank my colleages from the LABCEDE group: Steve Lipson, Pete Armstrong, Jim Dodd, Ron Lockwood, Steve Miller, and Bill Blumberg. They encouraged me to pursue this goal, helped me to understand the difference between good research and bad, and played a large part in my decision to attend UVA.

I would also like to thank the United States Air Force Academy Department of Physics for sponsoring my stay here, and for allowing me the opportunity to teach there. These have been the opportunities of a lifetime, and I would have been crazy to turn them down.

Finally, I thank my advisor, Tom Gallagher, whose understanding and experimen-

tal abilities have been the driving force behind my efforts. I am greatly indebted to him for the time and effort he has spent teaching me, and I have been honored with the opportunity to work for him. To paraphrase a certain quote, "The fact that X has published a paper with Tom Gallagher does not necessarily tell you anything about X."

Contents

1 Introduction 1
1.1 Rydberg Atoms . . . 2
1.1.1 Bohr's Model . . . 3
1.1.2 Properties of Rydberg Atoms . . . 6
1.2 Energy Resonant Dipole-Dipole Interactions . . . 10
1.2.1 A Simple Classical Picture . . . 12
1.2.2 A Simple Quantum Mechanical Picture . . . 14
1.3 Ultra-cold collisions . . . 16
1.4 Summary . . . 20

2 Experimental Apparatus 21
2.1 Outline . . . 21
2.2 Magneto-optical trap . . . 22
2.2.1 Theory of Operation . . . 23
2.2.2 Description of MOT apparatus . . . 29
2.3 Production and Detection of Rydberg Atoms . . . 36
2.3.1 Dye Lasers . . . 39
2.3.2 Electric Field Generation . . . 50
2.3.3 Charged particle detection . . . 52

3 Quasistatic Resonant Dipole-Dipole Interactions 54
3.1 Introduction . . . 54
3.2 Description of Energy Transfer Process . . . 56
3.2.1 Resonant Energy Transfer in a Quasistatic Picture . . . 58
3.2.2 Resonant Energy Transfer in a Four-Atom System . . . 61
3.3 Experiment description . . . 68
3.4 Data acquisition and analysis . . . 69
3.4.1 Resonance scans and linewidth scaling with density . . . 70
3.4.2 Signal development with allowed interaction time . . . 73
3.4.3 Time dependance of lineshapes . . . 75
3.5 Summary . . . 78

4 A Series of Dipole-Dipole Interactions: n Dependence **80**
4.1 Introduction 80
4.1.1 Multi-atom description of np resonances 82
4.2 Adiabatic Population Transfer 87
4.2.1 Landau-Zener Theory 88
4.2.2 Population Transfer Measurements 91
4.3 Scaling of Resonance Widths 97
4.4 On-Resonant Signal Devlopment 102
4.5 Summary 106

5 Tensor Polarizability of Rubidium d-states **108**
5.1 Introduction 108
5.2 Theory 108
5.3 Experimental Discussion 112
5.4 Data Analysis 118
5.5 Results 122
5.6 Summary 123

6 Summary **124**

Bibliography **126**

List of Figures

Figure	Title	Page
1.1	Schematic Representation of Energy Resonant Collision	11
1.2	Diagram of dipole-dipole collision	12
1.3	Pump-probe experiment to monitor ultracold collisions	18
2.1	Spatial confinement force in magneto-optical trap	27
2.2	Rb hyperfine levels	28
2.3	External cavity for diode lasers	32
2.4	Arrangement of Trapping Lasers	34
2.5	Rydberg state excitation scheme	37
2.6	Diagram of Hänsch cavity laser	40
2.7	Schematic diagram of Littman cavity laser	42
2.8	Pivot point for continuous mechanical tuning	45
2.9	Short-cavity dye laser design	48
2.10	Schematic of trap region	50
3.1	Resonant Transfer Energy Levels	56
3.2	Diagram of Four-Atom Interaction	61
3.3	Energy Levels of Binary Quasistatic Interaction	63
3.4	Energy Levels with One Coupling	65
3.5	Energy Levels of 4-Atoms System with Multiple Couplings	67
3.6	Energy resonances at various trap densities	71
3.7	Resonance Widths as a Function of Initial State Density	73
3.8	On-resonant signal time evolution	74
3.9	Resonance widths for various interaction times	77
3.10	Resonance widths for allowed interaction times	78
4.1	Diagram of Four-Atom Interaction for np Resonances	83
4.2	Energy Levels for $26p$ and $30p$ Resonances	86
4.3	Example of an Avoided Level Crossing	88
4.4	Timing Diagram for Population Transfer Measurements	91
4.5	Example Population Transfer Measurement	93

4.6 Slew Rate Dependence of Population Transfer: $26p$ 94
4.7 Measured κ from Population Transfer 95
4.8 Example $30p$ Resonance Scans 100
4.9 Density Dependence of Resonance Widths 101
4.10 Example $30p$ On-Resonance Signal Growth Scans 104
4.11 Density Dependence of On-Resonance Signal Development 105

5.1 $24d + 24d \rightarrow 23k + 25p$ Resonances 113
5.2 $24d + 24d \rightarrow 23, 9 + 25p$ Resonances with $|m_j| = \frac{1}{2}, \frac{3}{2}$ 115
5.3 $24d(k{=}9)$ Resonance Observation 116
5.4 $24d(k{=}9)$ Molecular States Including Fine Structure 117
5.5 Energy splittings for measured resonances with the $24d$ state 120
5.6 Measured values for $\alpha_2(nd)$ for n =23 to 33 121

List of Tables

Table	Title	Page
1.1	Quantum defects for low-ℓ states of Rb	9
1.2	Scaling properties of Rydberg atoms	9
2.1	Lifetime parameters for Rb	38
2.2	Parts List for Short-Cavity Dye Laser	47
4.1	Resonance Positions for $np_{3/2} + np_{3/2} \rightarrow ns + (n+1)s$	81
4.2	Fit parameters for Population Transfer Measurements	96
4.3	Dipole Matrix Elements for $np_{3/2} + np_{3/2} \rightarrow ns + (n+1)s$ Resonances	98
4.4	Resonance Widths for $26p$ and $30p$ Interactions	103
4.5	Measured Parameters for On-resonant Signal Growth	106
5.1	Measured values for $\alpha_2(nd)$	122

Chapter 1

Introduction

> *We go about our daily lives understanding almost nothing of the world. We give little thought to the machinery that generates the sunlight that makes life possible, to the gravity that glues us to an Earth that would otherwise send us spinning off into space, or to the atoms of which we are made and on whose stability we fundamentally depend. Except for children (who don't know enough not to ask the important questions), few of us spend much time wondering why nature is the way it is; where the cosmos came from, or whether it was always here; if time will one day flow backward and effects precede causes; or whether there are ultimate limits to what humans can know.*
> *... But much of philosophy and science has been driven by such inquiries. An increasing number of adults are willing to ask questions of this sort, and occasionally they get some astonishing answers.*
> –*Carl Sagan*[1]

While we do not profess to arrive at astonishing answers which illuminate the very core of our existence, this is an attempt to ask some interesting questions about a very small part of how nature works; how do atoms interact with each other. In specific, we are investigating characteristics of energy resonant dipole-dipole interactions between atoms in states with high principal quantum numbers, or Rydberg atoms. Put another way, we are looking at interactions which alter only the internal structure, or energy, of the atoms involved, but leave their kinetic energy intact. The interesting portion

of the questions we are asking is how do these interactions proceed in a relatively dense gas composed of atoms which may be characterized as having an extremely low temperature, less than a thousandth of a degree above absolute zero. This low temperature means that the atoms are essentially not moving relative to each other, and, along with the exaggerated properties of the Rydberg atoms, appears to be the source of the interesting properties we have observed.

Before we describe these experiments, we shall discuss in more detail the properties of Rydberg atoms, the characteristics of energy resonant interactions, and the nature of extremely low temperature, or ultracold, collisions. With this framework in place, we shall then go on to discuss our investigations in more depth.

1.1 Rydberg Atoms

While not entirely understood at the time, observations of atoms in states of high principal quantum number, n, were made as early as 1885, when Balmer observed that the wavelengths of the visible absorption lines of hydrogen were given by (*c.f.* [2])

$$\lambda = \frac{bn^2}{n^2 - 4}, \tag{1.1}$$

where b =364.56 Å and n represents the principal quantum number of the upper state of the transition. It was in part the work of J. R. Rydberg that helped to understand this formula, as well as formula describing other series of atomic spectral

lines, most notably those of sodium. Rydberg demonstrated that the spectral lines of these different atoms were related by the overall energy scale used to describe them, and that there should exist a general expression for these different series, although he did not really understand why. What seemed amazing at the time was that he was right, all the experimental observations could be described by one energy scale. That energy scale is defined by what is now called the Rydberg constant, denoted Ry, which has the value of 109737.3 cm^{-1}, where the wavenumber (with the unit cm^{-1}) is the inverse of the wavelength of light in vacuum. This constant is used to describe the wavenumbers of all series of spectral lines for all atoms, which may be written in general form as

$$\pm\nu = \frac{Ry}{(n-\delta_\ell)^2} - \frac{Ry}{(n'-\delta_{\ell'})^2}, \tag{1.2}$$

where δ_ℓ and $\delta_{\ell'}$ are experimentally determined values (now known to be the quantum defects) which give the locations of the series of atomic lines for different atoms. The Balmer lines are given by this formula if $\delta_\ell = \delta_{\ell'} = 0$ and $n = 2$.

1.1.1 Bohr's Model

It was not until the work of Neils Bohr over twenty years later and his proposed model for the hydrogen atom that a physical picture could be attatched to the states of high n, which have come to be called Rydberg states. While we now know that Bohr's theory is not precisely correct, it does accurately predict the properties of

the Rydberg states. The theoretical construct known as the Bohr atom has as its foundation an electron moving in a classical circular orbit around a nucleus (or ionic core for non-hydrogenic atoms). In order to account for the observations of distinct spectral lines in hydrogen, Bohr assumed that only distinct orbits could occur, and that any spectral transition had to correspond to a jump from one orbit to another. As a final assumption, Bohr assumed that the orbits could only have angular momenta corresponding to an integer number of units of $\hbar$, Planck's constant divided by 2π.

From classical mechanics, a circular orbit occurs when all of the kinetic energy contributes to the angular momentum of the orbit (i.e. $\dot{r} = 0$). This implies the condition

$$\frac{mv^2}{r} = \frac{kZe^2}{r^2}, \tag{1.3}$$

where Z is the charge of the ionic core and k is related to the permittivity of free space, ϵ_0, by $k = 1/4\pi\epsilon_0$. The requirement of quantized angular momentum may be expressed as

$$mvr = n\hbar. \tag{1.4}$$

Combining Eqs. 1.6 and 1.4, we get several crucial results. The first is the radius of an atomic orbit is given by

$$r = \frac{n^2\hbar^2}{Ze^2mk} = \frac{a_0}{Z}n^2, \tag{1.5}$$

where a_0 is the Bohr radius which equals 0.531 Å. Thus have calculated the scale

of atomic lengths from fundamental constants. We also see that Rydberg states are physically much larger than the ground state atoms. For instance, an atom in the $33s$ state will have a radius of 58 nm, over 1000 times that of a ground state atom. It is not uncommon for Rydberg atoms to be well over a micron in diameter.

We can also write down the energy of our atom in its circular orbit as the sum of the kinetic and potential energies

$$W = \frac{mv^2}{2} - \frac{kZe^2}{r} = -\frac{mk^2Z^2e^4}{2n^2\hbar^2}, \tag{1.6}$$

which allows us to calculate the difference betwen the bound energy levels n and n'. This is given by

$$\Delta W = \left[\frac{mk^2Z^2e^4}{2\hbar^2}\right]\left(\frac{1}{n^2} - \frac{1}{(n')^2}\right). \tag{1.7}$$

Comparing this result to Eq. 1.2, we recognize immediately that the term in brackets is 1 Ry when $Z = 1$. With a theoretical model, we have calculated that all atoms will have an energy scale defined by 1 Ry, as had been experimentally verified twenty years earlier. Further, this lets us calculate the difference in energy between states n and $(n+1)$, which scales approximately as n^{-3}.

Another point which becomes apparent using this simple model is that atoms in Rydberg states are quite susceptible to electric fields. In fact, relatively modest electric fields are capable of ionizing Rydberg atoms, stripping the electron from the ionic core about which it was orbiting. This is called field ionization of the atom, and

we can derive some basic information about it by considering an atom in an electric field along a well-defined axis. The presence of the field lowers the potential felt on one side of the ionic core, such that atoms with energies lower than the saddle point of the potential, $V_s = -2\sqrt{kE}$ remain in classically bound orbits. Thus atoms placed in a field greater than

$$E_c = \frac{(Ry)^2}{4kn^4} \tag{1.8}$$

are ionized by the presence of the field.

1.1.2 Properties of Rydberg Atoms

There is another result we may glean from our classical model. The Bohr model we discussed above assumes the ionic core, about which the outer electron orbits, is a point charge. In fact, for the alkali atoms such as sodium, potassium, rubidium, etc., this is inherently not true. The ionic core for these alkali atoms is formed by the nucleus and a closed, tightly bound shell of electrons, having a net charge of $+1e$. This size difference manifests itself in several ways. The most important is the energy shift of the low orbital angular momentum states, or states of low ℓ. The orbits with low angular momentum will be elliptical rather than circular in nature, implying the outermost, or valence, electron will at times be close to the ionic core. It is possible that the electron will even penetrate into the core for some portion of its orbit, and during this time will see a decidedly different charge distribution. We

would expect this to noticeably alter the energy states of the atom, which in fact it does. Core penetration and core polarization (which is due to the electron coming close to, but not penetrating, the ionic core) decrease the energy of a state with low orbital angular momentum relative to those of high orbital angular momentum. This effect is summed up by the following equation, which is given in atomic units, a unit system conveniently devised such that all of the parameters for the ground state of hydrogen are equal to one, thus 1 $Ry \equiv 1/2$. We shall use atomic units throughout this work, converting to more convenient units when necessary. For a definitive list of the values of atomic units see Ref. [3].

The decreased energy of the lower angular momentum states relative to the higher angular momentum states is given by

$$W(n,\ell) = -\frac{1}{2(n-\delta_\ell)^2}. \tag{1.9}$$

Here δ_ℓ is the quantum defect for a series of states with orbital angular momentum ℓ, which measures the effectiveness of the core penetration and polarization in altering the energy levels of those states. This equation is a very good approximation to the energy levels for even the most rigorous quantum mechanical calculations, and yet it is essentially the same as what Rydberg found over 100 years ago. For a more rigourous derivation of this effect, the reader is advised to consult Gallagher[4] or Stebbings and Dunning[5].

Now that we have established that we can calculate many of the properties of Rydberg atoms, we can discuss the notation used to describe them. We know now that the quantum mechanical state of a spinless one (valence) electron atom is expressed by a set of quantum numbers which describe certain properties. These include n, the principal quantum number, ℓ, which describes the orbital angular momentum of the valence electron, and m, which describes the projection of the angular momentum vector $\boldsymbol{\ell}$, onto the z-axis. Traditionally, states with orbital angular momentum $\ell = 0, 1, 2, 3, \ldots$ are referred to by the letters $s, p, d, f, \ldots$, respectively. We now consider how the inclusion of the spin of the valence electron changes this description. In alkali atoms, the valence electron spin, $\boldsymbol{s}$, couples to the valence electron orbital angular momentum, $\boldsymbol{\ell}$, such that $\boldsymbol{j} = \boldsymbol{\ell} + \boldsymbol{s}$, and thus $m_j = m_\ell + m_s$, where $m_\ell = m$ as previously defined. For states with $\ell > 0$, the quantized values of spin, $\pm 1/2$, lift an energy degeneracy so that $j = l \pm 1/2$, and lead to fine structure (or spin-orbit) splittings in the energy levels. States are specified by $n\ell_j$, for example $25s_{1/2}$ or $25p_{3/2}$.

With this notation in mind, we can list the quantum defects for the lowest angular momentum states of the atoms used in the experiments which are discussed in this work, rubidium atoms. Rubidium has two natural isotopes, ^{85}Rb and ^{87}Rb; however, we only use ^{85}Rb atoms for reasons which will become clear later, and as such, we refer to ^{85}Rb atoms as Rb. The relevent quantum defects for Rb are

Without resorting to further derivation, some other scaling properties of Rydberg

	$s_{1/2}$	$p_{1/2}$	$p_{3/2}$	$d_{3/2,5/2}$	$f_{5/2,7/2}$
δ_ℓ	3.13109	2.65456	2.64145	1.347157	0.016312

Table 1.1: Quantum defects for low-ℓ states of Rb[4].

atoms are listed in Table 1.2. The results provide some insight into why Rydberg atoms make interesting experimental subjects. These highly exaggerated properties make it possible to observe interactions that are unheard of in other systems, and at times make it possible to test fundamental precepts of physics, including the interaction of atoms with both strong and weak electromagnetic fields[6], and the transition between classical and quantum mechanic descriptions of a system.

Property	n dependence	Rb(25d)
Binding Energy	n^{-2}	0.024 eV
Energy between adjacent n states	n^{-3}	1.02 e-3 eV
Orbital Radius	n^2	934.5 a_0
Geometric Cross Section	n^4	8.73 e6 a_0^2
Dipole Moment $\langle nd\|er\|np\rangle$	n^2	759 ea_0
Polarizability	n^7	0.66 MHz/(V/cm)^2
Radiative Lifetime	n^3	17.2 μs
Fine Structure Interval	n^{-3}	-691.2 MHz

Table 1.2: Scaling properties of Rydberg atoms, with examples for Rb. Adapted from Gallagher[4].

1.2 Energy Resonant Dipole-Dipole Interactions

We now turn our attention to the characteristics of energy resonant interactions between Rydberg atoms. At higher translational energies than we are examining, these interactions would be described as resonant energy transfer collisions, and have long been studied as they play an important role in the development of many gas lasers, including CO_2 and He-Ne lasers. Resonant energy transfer collisions occur when the colliding species change only their internal energy, rather than their kinetic energy as typically occurs with atomic scattering reactions. They are also a common form of population transfer in upper atmospheric processes, where energy resonances between ro-vibrational levels of molecules provide for rapid population redistribution[7, 8].

The resonant collisions we are studying occur between two Rydberg atoms, each in a well-defined, but not necessarily identical, initial state, say $|n_1\ell_1 m_{j,1}\rangle$ and $|n_2\ell_2 m_{j,2}\rangle$, with energies W_1 and W_2. The dipole moment of atom 1 interacts with the dipole moment of atom 2 as they pass near each other. This dipole-dipole interaction causes atom 1 and atom 2 to undergo a dipole transition to the states $|n_1'\ell_1' m_{j,1}'\rangle$ and $|n_2\ell_2 m_{j,2}\rangle$, with energies W_1' and W_2', respectively. The condition of energy resonance implies $W_1+W_2 = W_1'+W_2'$, while the dipole transitions require that $\Delta\ell_i = \pm 1$ and $\Delta m_{j,i} = 0, \pm 1$. In an ideal experiment, we imagine that the energy of one or all of the atoms is altered by some parameter which we may control in a continuous manner, call it ξ, in such a way that at some value of this parameter, the condition of

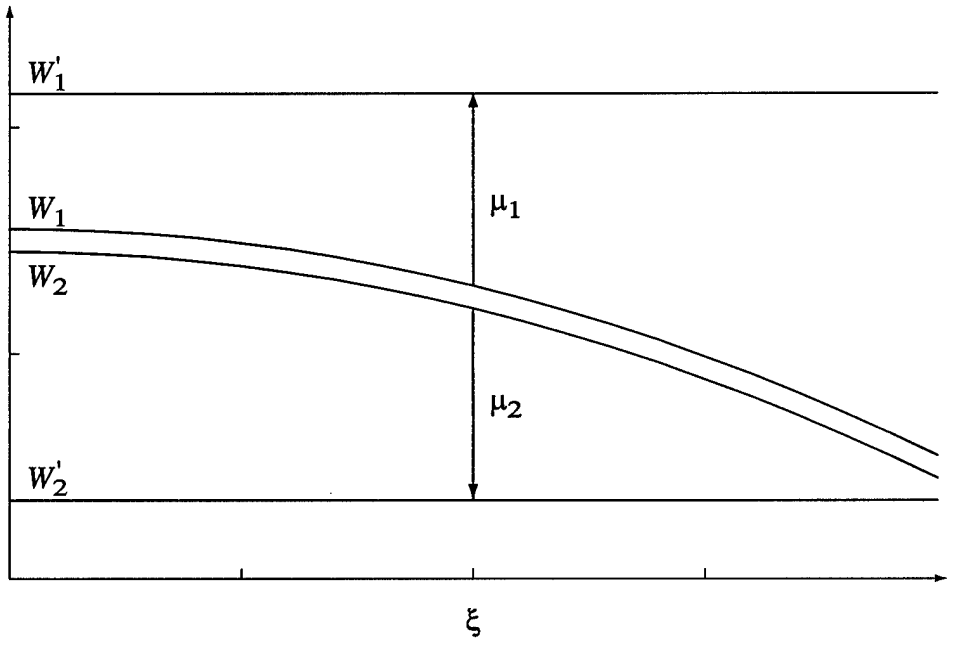

Figure 1.1: Schematic representation of an ideal energy resonant collision. Shown are the atomic energy levels as they scale with a controllable parameter ξ. Notice that $|W_1' - W_1| = |W_2' - W_2|$ at the indicated resonance position. The arrows show the transfer of population with the dipole matrix element labeled. For clarity, the degenerate transition in which atom 1 goes to state $2'$ and atom 2 goes to state $1'$ is not shown.

energy resonance is met and the cross section for the energy resonant collision reaches a maximum. This is shown schematically in Fig. 1.1.

The Stark shift of the densely spaced energy levels in Rydberg atoms (see Sec. 5.2 for a discussion about the Stark shift of energy levels in an atom) allows one to realize such an ideal experiment, as was done with Na atoms by Safinya, *et al.* in 1981[9]. As an illustration of such a collision between two Rydberg atoms, let us consider the following process in Rb:

$$np_{3/2} + np_{3/2} \rightarrow ns_{1/2} + (n+1)s_{1/2}. \tag{1.10}$$

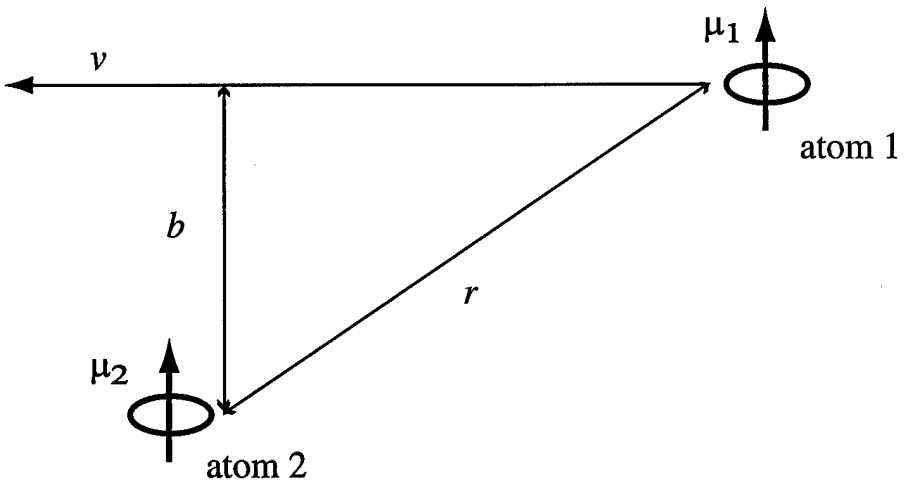

Figure 1.2: Diagram showing the geometry of a simplified dipole-dipole collision.

Each of these states is dipole coupled, and with a few simple assumptions, we can calculate some characteristics of their interaction. For more detailed calculations, the interested reader should consult Gallagher[10] or Veale[11].

1.2.1 A Simple Classical Picture

We start by assuming that we are tuned to the resonant electric field, and that the two atoms (which we call atom 1 and atom 2 for lack of a better name like Pete or Steve) are approaching each other with a relative velocity v and at an impact parameter b, as shown in Fig. 1.2. In order to treat the problem classically, we note that the dipole matrix elements, which in atomic units are written $\langle np|r|ns\rangle$ and $\langle np|r|(n+1)s\rangle$, may be viewed as oscillating classical dipoles, with the dipole moment equal to the matrix element, and the frequency of the oscillation corresponding to the transition

frequency[10]. Thus we may write $\langle np|r|ns\rangle = \mu_1$ and $\langle np|r|(n+1)s\rangle = \mu_2$. If we view atom 2 as being fixed in space, the passage of atom 1, with its classically oscillating dipole, will induce the dipole transition in atom 2. Atom 1 produces a field $E_1 = \mu_1/r^3$ at the position of atom 2, where r is the separation between the atoms. This resonant field will drive the transition in atom 2 provided the interaction strength is sufficient. This interaction strength is

$$\mu_2 E_1 = \frac{\mu_1 \mu_2}{r^3}. \tag{1.11}$$

We make the simplifying assumption that the field is given by

$$E_1 = \tfrac{\mu_1}{b^3}, \quad r \leq \frac{\sqrt{5}}{2} b \tag{1.12}$$

$$E_1 = 0, \quad r > \frac{\sqrt{5}}{2} b, \tag{1.13}$$

which has the same time integrated interaction strength as the dipole potential. The length scale defined by Eq. 1.12 implies that atom 2 only interacts with atom 1 for a time $t = b/v$. Atom 2 will undergo a transition if the time integrated interaction is near one, or $E_1 \mu_2 t \approx 1$ [10]. Substituting in known values gives us the transition condition

$$\frac{\mu_1 \mu_2}{b^3} \frac{b}{v} = \frac{\mu_1 \mu_2}{v b^2} \approx 1. \tag{1.14}$$

Equation 1.14 allows us to estimate the cross section, giving

$$\sigma_R = \pi b^2 \approx b^2 = \frac{\mu_1 \mu_2}{v}. \tag{1.15}$$

While the collision time is given by

$$t = \frac{\sqrt{\mu_1 \mu_2}}{v^{3/2}} = \frac{1}{\Delta\nu}. \tag{1.16}$$

1.2.2 A Simple Quantum Mechanical Picture

A slightly more refined model will allow us to calculate the form of the lineshape of the collisional resonance. The method is essentially as presented in Gallagher[10]. We again begin with the assumption of two atoms moving in a straight line with an impact parameter, b. Our goal is to calculate the probability of transition $P(b)$ for a given impact parameter. Integration over all possible impact parameters will give us the cross section. We start the problem by constructing the direct product states for the initial and final states of the atoms involved in the interaction. We refer to these as molecular states, and write them as

$$|\psi_i\rangle = |np_{3/2}\rangle_1 |np_{3/2}\rangle_2, \text{ and } \quad |\psi_f\rangle = |ns_{1/2}\rangle_1 |(n+1)s_{1/2}\rangle_2. \tag{1.17}$$

These states are the solutions to the time-independent Schrödinger equation with Hamiltonian $\mathcal{H}_0 = \mathcal{H}_1 + \mathcal{H}_2$, where $\mathcal{H}_i$ is the non-interacting Hamiltonian for atom i in an electric field. The interacting Hamiltonian then becomes $\mathcal{H} = \mathcal{H}_0 + V_{\text{dipole}}$, or

$$\mathcal{H} = \mathcal{H}_0 + \frac{\boldsymbol{\mu_1} \cdot \boldsymbol{\mu_2}}{r^3} - 3\frac{(\boldsymbol{\mu_1} \cdot \mathbf{r})(\boldsymbol{\mu_2} \cdot \mathbf{r})}{r^5}. \tag{1.18}$$

The last two terms are the vector forms of the dipole-dipole interaction[12].

We now seek to solve the time-dependent Schrödinger equation, $H\Psi = i\partial\Psi/\partial t$, which for the states we have defined in Eq. 1.17, gives us solutions of the form

$$\Psi = C_i(t)|\psi_i\rangle + C_f(t)|\psi_f\rangle, \tag{1.19}$$

in which all of the time dependence is contained in the coefficients $C_i(t)$ and $C_f(t)$. The time-dependent Schrödinger equation then becomes

$$\begin{pmatrix} C_i \\ C_f \end{pmatrix} \begin{pmatrix} W_i + V_{ii} & V_{fi} \\ V_{if} & W_f + V_{ff} \end{pmatrix} = i \begin{pmatrix} \dot{C}_i \\ \dot{C}_f \end{pmatrix}, \tag{1.20}$$

where W_j represents the energy of the initial or final molecular state, and $V_{jk} = \langle\psi_j|V|\psi_k\rangle$, the (time-dependent) matrix element of V connecting the two molecular states j and k.

In general Eq. 1.20 is analytically insoluble, except for a few cases. One of these

is defined by the potential of Eqs. 1.12 and 1.13, in which case $V_{ii} = V_{ff} = 0$. For small interactions, our assumption of a straight line trajectory will hold, which allows us to write $r = \sqrt{b^2 + (vt)^2}$. With the initial condition $C_i(0) = 1, C_f(0) = 0$, we find after a time $t > b/v$

$$P(b) = |C_f|^2 = \frac{|V_{if}|^2}{\Omega^2} \sin^2\left(\frac{\Omega b}{v}\right), \tag{1.21}$$

where

$$\Omega = \frac{1}{2}\sqrt{(W_i - W_f)^2 + 4|V_{if}|^2}, \tag{1.22}$$

is the Rabi frequency of the collision. The form of Eq. 1.21 implies that the resonant collisions have Lorentzian lineshapes with width $\Delta\nu \approx \sqrt{v^3/\mu_1\mu_2}$, as we determined in Eq. 1.16.

With these basic properties of energy resonant dipole-dipole collisions in mind, let us now turn our attention to collisions which occur between atoms with very little kinetic energy.

1.3 Ultra-cold collisions

With the advent of laser cooling and trapping techniques, it has become possible to observe collsions between atoms in energy regimes previously unthinkable. Atoms with temperatures of $\approx$ 100 μK are readily attainable using standard cooling and trapping techniques, such as those outlined in Sec. 2.2. Collisions in which the ki-

netic energies of the colliding atoms are ≈ 1 mK or less have been accepted within the general community as "*ultracold collisions*," and their study has led to some interesting discoveries[13]. Experiments have taken advantage of the long collision times to form bound molecular states via photoassociation[14, 15, 16]. Further excitation from these bound molecular states can lead to photoassociative ionization and subsequent ejection of the ion from the trap[17, 18]. Additional efforts have centered on use of optical fields to prevent or alter collisions which result in trap loss[19, 20, 21]. We shall attempt to very briefly highlight some of the properties of these collisions and contrast them to the energy resonant interactions we observe in the following chapters.

Although all alkali atoms have been used in ultracold collision experiments, we use Rb atoms as an example here. We will consider ultracold collisions occuring principally between Rb atoms in the ground state, $5s$, and the excited state, $5p$, produced by the trapping lasers. These collisions are dipole-dipole in nature, and hence their interaction has the form of Eq. 1.11, however the relavent dipole moments are typically $\mu \approx \mu' \sim 3ea_0$[22]. Using the results of Eq. 1.16, we see this implies that the collisions are of duration $t_c \sim$ 30-50 ns, in excess of the 27 ns lifetime of the $5p$ excited state. As such, collisions are frequently terminated by the spontaneous emission of a photon taking the $5p$ atom back into the $5s$ ground state[23]. However, should the atoms continue to small internuclear separations, the spontaneous decay will be red-shifted due to the well in the $5s + 5p$ potential. This process transfers

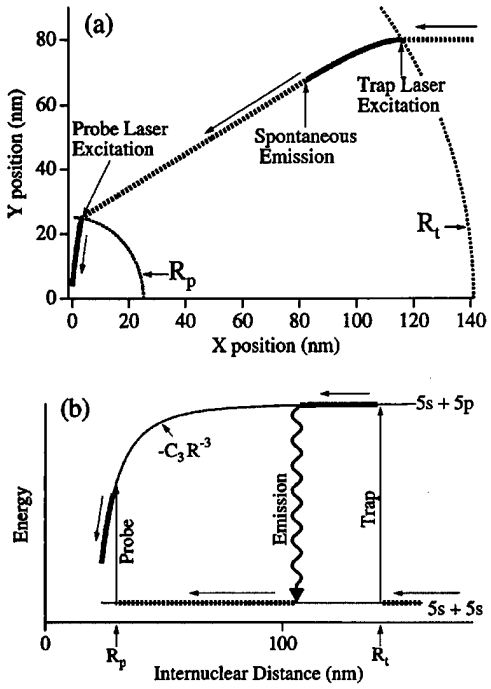

Figure 1.3: (a) Typical classical trajectory of an atomic collision showing the flux enhancement effect. The solid (dashed) line indicates the atoms trajectory while in the excited (ground) state. The incoming atom approaches from the right. The atom pair is excited at R_t by the trap laser pulse and is accelerated by the attractive long-range potential. After spontaneous decay, it proceeds to R_p, where it may be excited again by a probe laser pulse. The atom pair is then accelerated quickly into short range, where either RE (Radiative Escape from the Trap) or ΔJ (fine-structure change) may occur, leading to trap loss. (b) Molecular potential diagram for the same process. Taken from Ref. [26].

enough potential energy into the kinetic energy of one of the trapped atoms to eject it from the trap. Collisions such as these are often monitored by detecting changes in the rate at which atoms are lost from the trap. More thorough theoretical treatments are given by Gallagher and Pritchard[24], and Julienne *et al*[25].

One such experiment by Gensemer and Gould uses a pump-probe arrangement to directly measure an enhancement in the population of atoms at close internuclear separations[26], as shown in Fig. 1.3. By initiating the collisions at large separations,

they are able to monitor the dependence of the trap loss signal on the delay between pulses. They have, in effect, designed an experiment which takes advantage of the difference between the attractive and repulsive potential energy curves of the dipole-dipole interaction. The strength of interaction is sufficient to accelerate the pair of atoms to a relatively high energy ($\sim$ 1 K)[23].

An intriguing point is raised by these experiments. The dipole moments of the interactions we shall discuss in the remainder of this work are stronger by factors between 100 to 1000, depending on the system discussed. As such, there are two key differences between the cold collisions discussed above and those we shall discuss. First, the effective range of the interaction scales as the product of the dipole moments; in typical ultracold collisions these are $\sim$ 100 nm, whereas in our experiments these numbers are more typically $\sim$ 10 μm. This can exceed the average internuclear separation, making the role of multi-atom interactions much more important, as we shall see in Chap 3. Second, the forces involved in the collisions also scale as the product of the dipole moments; the typical ultracold collision experiment can produce changes in the kinetic energy of the colliding atoms of $\sim$ 1 K; should our experiments result in similar impact parameters, the interactions we study could produce changes in excess of $\sim$ 100 K.

1.4 Summary

Having explored some of the more interesting general properties of Rydberg atoms, the characteristics of energy resonant dipole-dipole interactions between atoms, and the unusual traits of ultracold collisions, we are now ready to discuss the experiments which make up the remainder of this work. We start this discussion by outlining how the experiments were performed, including a look at how we produced the frozen Rydberg gas. Next we discuss a pair of experiments which highlight the multi-atom nature of the dipole-dipole interactions in our frozen Rydberg gas. We then discuss an experiment which takes advantage of some of the characteristics of these interactions to measure fine-structure splittings in Rydberg states of Rb. Finally, we end with a look toward the future, examining potential follow-on experiments to further elucidate the nature of these dipole-dipole interactions.

Chapter 2

Experimental Apparatus

2.1 Outline

In this chapter we shall describe the experimental apparatus used to perform the experiments described in the following chapters. We begin with a section discussing the magneto-optical trap (or MOT) used. In this section, we shall describe both the theory behind laser cooling and trapping and its application to our apparatus. Finally, we outline the calibration of the monitoring apparatus used to characterize the trapped atoms.

We then discuss the preparation and measurement of the Rydberg atoms produced from the trapped atoms. We briefly describe the dye lasers used to excite the Rb atoms into the required Rydberg states. This section also includes a description of the generation of the electric fields used both to tune the atomic energy levels and to

measure the results of the interactions studied. We shall end this section by describing the detection and measurement of the Rydberg atoms.

2.2 Magneto-optical trap

The idea that one could use lasers to slow or cool atoms was independantly suggested by Theodore Hänsch and Arthur Schawlow[27] and Hans Dehmelt and David Wineland[28] in 1975. As early as 1978, laser cooling of ions had been reported by several groups[29, 30]. By 1981, Phillips, *et. al.*[31] had successfully cooled a sodium beam in one dimension using resonant laser pressure. Chu, *et. al.*[32] demonstrated the three-dimensional cooling and confinement of neutral atoms via resonant light pressure. Shortly thereafter, in 1987, the first magneto-optical trap was demonstrated[33] in which near-resonant light was used to provide a linear restoring confinement force by exploiting the magnetic structure of the atoms. Rapid advancement has followed these discoveries, and led to the awarding of the 1997 Nobel Prize jointly to William Phillips, Steven Chu, and Claude Cohen-Tannoudji for their pioneering work in the field. Several good review articles [34, 35, 36] and special journal issues[37, 38] have been devoted to laser cooling and trapping of neutral atoms, and will point the reader towards other references.

2.2.1 Theory of Operation

Laser Cooling of Atoms

Laser cooling of neutral atoms results from the conservation of momentum between the atoms and the photons of a laser beam. The simplest type of cooling, "Doppler cooling" can be described in terms of a two-level atomic system, having simply a ground state, $|g\rangle$, and an excited state, $|e\rangle$. While in reality there exists no such system, it may be approximated using dipole selection rules for transitions between states of angular momentum J and $J+1$ and given the absorption of circularly polarized light. Then atoms in the $|g, m_j = \pm J\rangle$ sublevel can only be excited to the $|e, m_j = \pm(J+1)\rangle$ sublevel, which can then only decay to the $|g, m_j = \pm J\rangle$ sublevel.

The absorption of a photon from the laser field will impart a momentum $\hbar\mathbf{k}_L$ to the atom, where $\mathbf{k}_L$ is the wave vector of the photons in the laser field. The excited atom can return to the ground state through either stimulated or spontaneous emission. Should the atom emit a photon stimulated by the laser field, the emitted photon will rejoin the laser field in the same mode and the atom will lose $\hbar\mathbf{k}_L$ momentum, resulting in no net change in the atom. However, the spontaneous emission of a photon of momentum $\hbar\mathbf{k}_s$ is an isotropic process, so on average, the atom will experience no net change in momentum from the emission of a spontaneous photon. Thus the net process of absorption of a photon from the laser field and spontaneous decay will, on average, result in a change in momentum of $\Delta p = \hbar\mathbf{k}_L$. For a ^{85}Rb atom the resulting

change in velocity is 0.6 cm/s. The average force exerted by the laser beam depends on the rate of spontaneous decay, which is given by the product of the probability of being in the excited state, ϱ_e, and the decay rate of the upper state, γ_e (which is the inverse of the lifetime of the state, τ_e). For steady-state processes, $\varrho_e = 1/2$, and the maximum possible acceleration of the atom has magnitude

$$a_{doppler} = \frac{\hbar k_L \gamma_e}{2m} = 1.1 \times 10^5 \mathrm{m/s}^2. \tag{2.1}$$

The force we have described with our simplified picture exists only when the laser is resonant with the Doppler-shifted atomic transition. For cold atoms and symetrically overlapping lasers detuned slightly to the red of the atomic transition, the force will provide viscous dampening of the atomic motion, forming what is known as an optical molasses. However, the process of spontaneous emission will cause the atoms to diffuse out of the overlap region. The temperature limit for this cooling process, T_D, or Doppler temperature, is determined by the balance between the cooling force and the momentum diffusion of the atoms, and can be estimated from the uncertainty in energy of the spontaneously emitted photon, $\hbar\gamma_e$. In fact this limit is given by[39]

$$k_B T_D = \frac{1}{2}\hbar\gamma_e, \tag{2.2}$$

which is about 141 μK for Rb atoms.

It was quickly realized that atoms in an optical molasses were reaching temperatures far below this Doppler limit[40]. In fact, molasses temperature were measered at several times the recoil limit, T_R, which is defined as the temperature corresponding to the energy transfer between the laser photon and the cooled atom. For Rb, $T_R = 181$ nK. The discrepancy was explained by Claude Cohen-Tannoudji and Jean Dalibard as resulting from what is termed "Sisyphus cooling" or polarization gradient cooling[41]. The mechanism is a complicated result of spatial variations in the polarization gradients of the laser field, the changes in the energy levels of the atom due to the presence of the photons (light shifts), and the optical pumping rates between the two levels involved in the cooling. We now turn our attention to how we can constrain the motion of laser-cooled atoms to a specific region of space, forming an atomic trap.

Magneto-Optic Trapping

The first demonstrated neutral atom trap utilized a quadrupolar magnetic field to provide a restoring force for the atoms in the trap[42]. An atom with a magnetic dipole moment $\boldsymbol{\mu}$ will experience a force when placed in a magnetic field gradient. When the dipole moment of the atom is aligned with the field, the atom is attracted to the region of minimal field, while atoms anti-aligned with the field are repelled from the field strength minimum. A quadrupolar magnetic field provides a region of local field strength minimum and a gradient that is nearly linear in all directions.

The first magneto-optical trap utilized the viscous cooling force of near-resonant laser light and the spatially varying magnetic field of the magnetic dipole trap to provide a means for simultaneously confining and damping atomic motion. The quadrupolar field produces Zeeman shifts in the atomic energy levels which vary linearly with the displacement of the atom from the field minimum. When combined with appropriately polarized near-resonant lasers, these energy shifts provide a restoring force for confinement of the atoms.

A simple example demonstrates this principle: consider that the ground state of an atom, $|g\rangle$, has angular momentum $J = 0$, and $|m_j| = 0$, while the excited state, $|e\rangle$, has $J = 1$ and $|m_j| = 0, \pm 1$. The quadrupolar magnetic field will vary linearly along the z-axis as $B(z) = B_o z$. The Zeeman effect will cause the upper state energy levels to separate as shown in Fig. 2.1. These atoms are placed in a region of space which has a laser beam of polarization σ^+ travelling in the $+z$ direction, and one of polarization σ^- travelling the opposite direction. We shall use the polarization sign convention used in the laser cooling and trapping literature, in which light of polarization σ^+ induces a transition from the $|m_j| = 0$ ground state to the $|m_j = +1|$ state, and σ^- induces a transition to the $|m_j = -1|$ state

The oppositely polarized lasers will result in a spatial dependance of the detunings to the upper state sublevels when the cooling lasers are detuned from the zero-field resonance. An atom is more likely to absorb light with a smaller detuning from resonance, thus light from one of the lasers will be absorbed at a higher rate, resulting

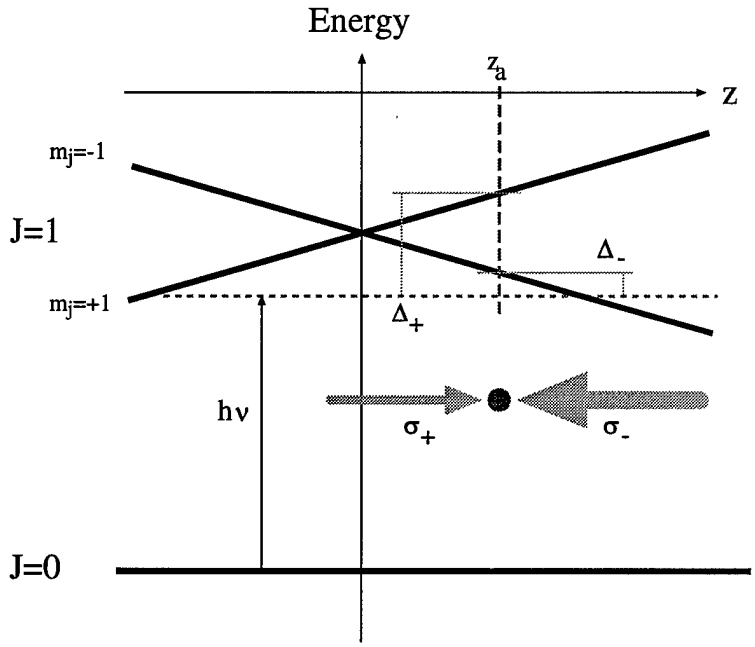

Figure 2.1: Schematic diagram depicting the spatially confining force felt by an atom in a magneto-optical trap. Consider the atom shown to have two levels, a $J = 0$ ground state and a $J = 1$ excited state, having two $|m_j|$ sublevels and moving near the zero of a quadropolar magnetic field. There are two counter-propagating laser beams of frequency ν, with opposing circular polarizations. The laser incident from the left has polarization σ^+, defined to promote transition to the $|m_j = +1|$ state, while the laser incident from the right has polarization σ^-, which promotes transition to the $|m_j = -1|$ state. The asymmetry in detunings for the two transitions results in an imbalanced optical force which varies with the position of the atom. For example, at $z = z_a$, the atom will experience a larger scattering rate for the σ^- transition and will be accelerated toward $z = 0$. The figure is taken from Bradley and Hulet[36].

in a spatially varying restoring force which effectively traps the atom along that axis. Generalizing this idea to three dimensions results in a Magneto-Optical trap, or MOT.

To build a ^{85}Rb MOT, one must take into acount that it is not strictly a two level atom. ^{85}Rb has 37 protons and electrons with an atomic mass of 84.911 amu. The first 36 electrons occupy closed subshells. It therefore occupies the ground $5s$ state. It has a total angular momentum of $J = L + S = 1/2$, while the nucleus has spin

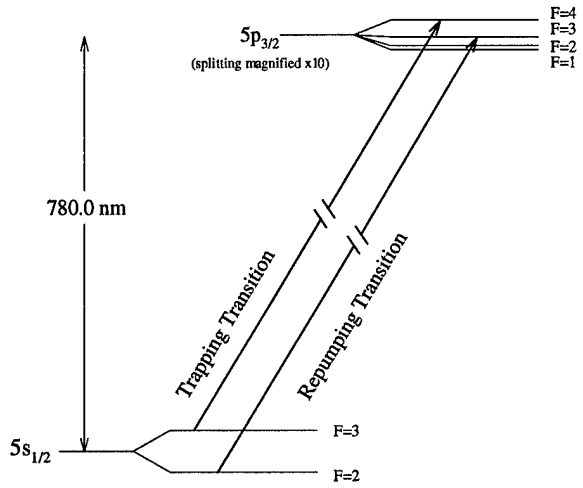

Figure 2.2: Hyperfine levels of Rb with the trapping and repump transitions marked. The spacing between the $5s_{1/2}$ and $5p_{3/2}$ levels is not to scale, and the splitting between the $5p_{3/2}$ sublevels has been magnified by ten. The spacings between the $5s_{1/2}$ sublevels is 3036 MHz, while the spacing between the $5p_{3/2}$ sublevels are, in order, 29, 63, and 121 MHz.

$I = 5/2$. The total spin, F is formed by coupling J to I. The ground $5s_{1/2}$ state can have $F = 2$ or 3, while the excited $5p_{3/2}$ state can have $F = 1$, 2, 3, or 4. The lasers used for cooling and trapping the atoms are tuned ~5 MHz to the red of the Rb $F = 3 \rightarrow 4$ transition between the $5s_{1/2}$ ground level and the $5p_{3/2}$ level. This transition has a wavelength of 780.0 nm. However, the $5p_{3/2}$, $F = 3$ level is 120 MHz from the $F = 4$ level, resulting in some (0.1 %) population transfer to the $F = 3$ level. Spontaneous decay out of this sublevel will result in the atom being in the $5s_{1/2}$, $F = 2$ sublevel, which is 3 GHz from the $F = 3$ sublevel. Thus all atoms in the $F = 2$ sublevel of the $5s_{1/2}$ state will have no interaction with the cooling and trapping lasers, and thus will escape from confinement. In order to compensate for this loss mechanism, one must also introduce a "repumping" laser tuned to the Rb $5s_{1/2}$, F

$= 2 \rightarrow 5p_{3/2}$, $F = 3$ transition, as shown in Fig. 2.2. This laser is aligned to overlap the region defined by the intersection of the six trapping lasers.

2.2.2 Description of MOT apparatus

Vacuum System

In our MOT, the Rb atoms were introduced into a room temperature stainless steel vacuum chamber held at a background pressure of 10^{-8} torr by heating a sidearm containing $\approx$ 1 g of Rb to approximately 45°C. Heating the sidearm was necessary in order to increase the fill rate of the trap, thus preventing excessive depletion from the field ionization during the course of an experiment. The vacuum chamber was manufactured by Nor-Cal Products, Inc., with ultra-high vacuum (UHV) compatible components[43]. All of the flanges use conflat-style connections to maintain the necessary pressure. There are eight windows providing optical access through 4 axes: x, y, z, and $(x + y)$. The electrical connections are made via two Varian electrical feedthroughs located on the $(x - y)$ axis.

In order to minimize collisional losses from the MOT, the background pressure must be kept as low as possible. It is therefore impractical to use a mechanical roughing pump and diffusion pump combination, as these would result in oil backstreaming into the vacuum chamber. The most logical choice for vacuum pump is then a sputter-ion pump, which has no moving parts and is relatively inexpensive. A sputter-ion

pump operates by placing a large potential difference between stainless steel anodes and two cathodes, one of titanium and one tantalum. Atoms or molecules which travel between the anode and cathode are ionized and imbedded into the cathode. Pumping speed and overall pump lifetime are then determined by the total surface area of the two cathodes. Sputter-ion pumps are extremely efficient at pumping light atoms and inert gasses, and have the minor disadvantage of pumping Rb. One must take care not to load the pump with the output of the Rb source continuously, as this will severely degrade the lifetime of the pump. The vacuum chamber used in these experiments uses a Perkin-Elmer Differential Ion Pump, with a nominal pumping speed of 20 liters/sec. The ion pump is powered by a Perkin-Elmer 5 kV ion pump power supply.

Sputter-ion pumps are unable to operate at pressures above about 10 mTorr, so a roughing system must be used to achieve this pressure. In order to keep the vacuum system clean, a battery of molecular-sieve (sorption) pumps is used for rough pumping. These pumps are filled with pellets of artificial zeolite, a material with a large surface area to mass ratio ($\approx$ 1000 m^2/g with a typical pump holding 5-10 g). Cooling the zeolite with liquid nitrogen causes most gases to adhere to the zeolite and be removed from the chamber volume. Sorption pumps do not pump H_2, He, or Ne well, but using a battery of three pumps consecutively can bring the chamber pressure down to below 1 mTorr, which is sufficient for starting the sputter-ion pump.

The sorption pump battery is attatched to the chamber with an all-metal UHV

valve. After the roughing operation is completed, the valve may be closed and the sorption pump battery removed for more convenient access to the MOT chamber.

Cooling and Trapping Lasers

As stated in Sec. 2.2.1, lasers operating at 780.0 nm are needed to cool and trap Rb atoms. There are two potential sources of light at that wavelength, a continuous-wave (cw) Ti:Sapphire laser or AlGaAs diode lasers. Due to their extremely low cost and relative ease of use, we have chosen to use diode lasers to provide the trapping laser fields. The lasers have powers from 25 to 50 mW and are available commercially from Sharp and Spectra Diode Labs (SDL), with natural linewidths of about 30 MHz. The wavelength of the laser output of a given laser diode can be tuned by adjusting the temperature of the diode and the current density. Adjusting the temperature of the laser has two effects: the gain curve of the laser is shifted by 0.25 nm/K, and the cavity length changes by 0.06 nm/K[44]. The difference in these tuning rates causes discontinuous changes in the cavity modes which are supported by the diode, or "mode hops".

The trapping scheme outlined in Sec. 2.2.1 requires lasers with a linewidth less than the 5.89 MHz natural linewidth of the atomic resonance. This can be done by placing the diode laser in an external cavity, thus reducing the ratio of the spontaneous emission rate to the number of photons in a given cavity mode, and therefore the linewidth of the laser. We use an external cavity design from Carl Wieman's group[45],

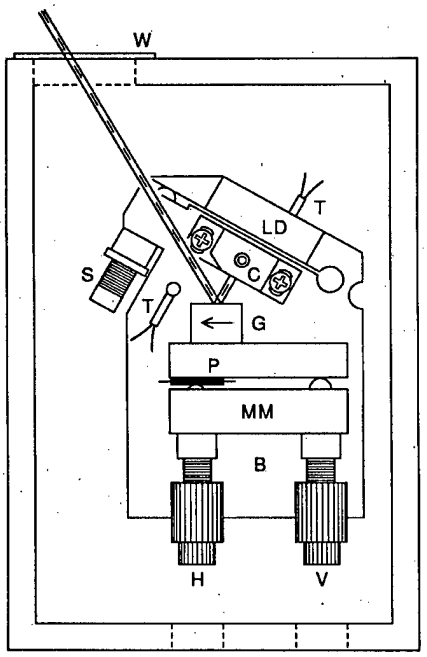

Figure 2.3: Top view of laser diode in external cavity from MacAdam, *et. al.*[45]. The laser diode is denoted LD, with collimating lens C. The fine screw S adjusts the relative positions of the diode and the lens. The grating is mounted with blaze in the direction indicated by the arrow on a mirror mount (MM). A piezo-electric disk (P) is sandwiched behind the horizontal adjustment screw to provide fine electronic scanning of the output wavelength. The entire apparatus is placed in a box and covered to protect it from air currents. The window (W) is antireflection coated at 780 nm. A thermistor (T) monitors the temperature of the diode and assembly.

as shown in Fig. 2.3, which utilizes a diffraction grating as one surface of the cavity, and the high-reflectivity back surface of the diode as the second. The front face of the diode has an antireflection coating on the front surface, which permits the extinction of the internal "free running" mode of the diode by the higher Q of the external cavity. Further wavelength selectivity is achieved by using a diffraction grating as the second surface of the cavity and feeding back the Littrow order of the diffracted

light. The resulting linewidths are typically well below 1 MHz; Anderson measured a linewidth of less than 100 kHz using these lasers[43].

The frequency of the trapping and repump lasers is controlled by frequency locking to the sideband of the Rb $F = 3 \rightarrow 4$ and Rb $F = 2 \rightarrow 3$ transitions using a saturated absorption setup[46] and an active feedback loop[45]. A portion of the output of a master laser is used for frequency locking to each of the transitions. The remaining light is used to injection lock slave lasers. For the trapping transition, the master laser is a Sharp LT024MD0 25 mW diode laser placed in an external cavity, while two SDL 5401-G1 50 mW laser diodes cool the atomic vapor. The trapping beams typically have 10 mW of power and are approximately 9 mm in diameter. The repump laser is also an SDL 50 mW diode laser, and is injection locked to a frequency-stabilized Sharp 25 mW master diode laser in the external cavity configuration. The SDL repump slave beam typically has 35 mW of power and is typically 23 mm in diameter. The geometry of the components used for generation of the trapping and repump laser beams are shown in Fig. 2.4

Magnetic Field Production

The quadropolar magnetic field required to trap the Rb atoms was produced by a pair of magnet coils placed in the anti-Helmholtz configuration. In this configuration a co-axial pair of coils separated by distance $2A$ and with radius R have equal currents I running in opposing directions. The axial and radial components of the magnetic

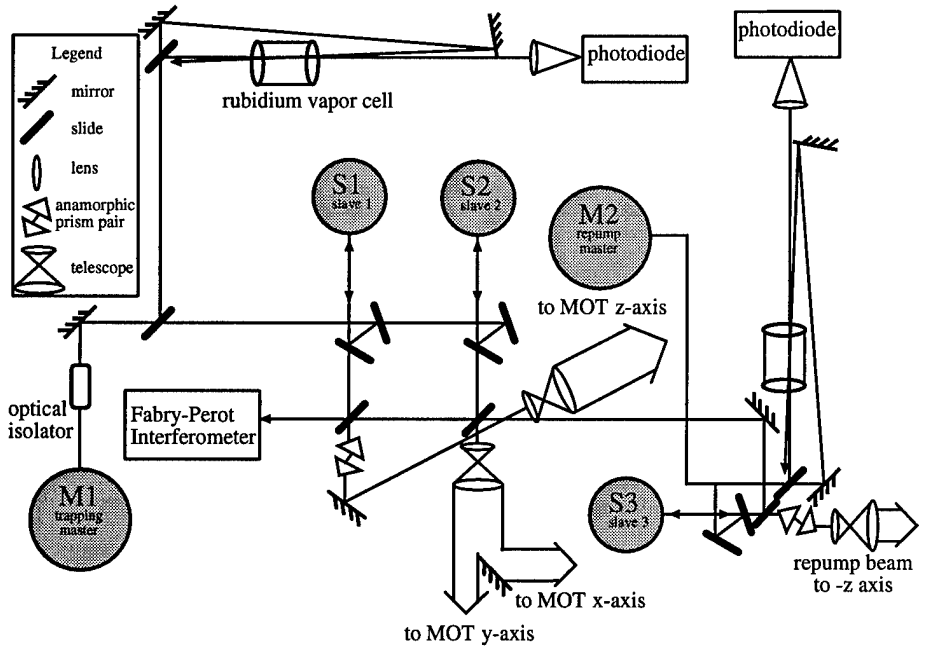

Figure 2.4: Depiction of the geometry of the lasers used for cooling and trapping. Included are the saturated absorption vapor cells, the injection-locking setup, and the Fabry-Perot interferometer used to monitor the laser output.

field generated by such an arrangement are given by[47]

$$B_z = b_1 z + b_3 \left(z^3 + \frac{3z\rho^2}{2} \right) + \cdots, \tag{2.3}$$

and

$$B_\rho = -b_1 \left(\frac{\rho}{2} \right) + b_3 \left(\frac{-3\rho z^2}{2} + \frac{3\rho^2 z}{8} \right) + \cdots, \tag{2.4}$$

where the coefficients are

$$b_1 = \frac{3\mu_0 I A R^2}{(R^2 + A^2)^{5/2}}, \tag{2.5}$$

and

$$b_3 = b_1 \times \frac{5\left(4A^2 - 3R^2\right)}{6\left(R^2 + A^2\right)^2}. \tag{2.6}$$

The coils used on the MOT have 12 turns (three coils of four turns) of 1/8 inch o.d. copper automotive tubing covered with shrink-wrap insulation held in place by an aluminum form. The turns have an effective radius of 10.16 cm. The coils are separated by $2A = 14$ cm, and have 100 amperes of current running through them. Placing these values into Eqs. 2.3 and 2.5 indicate typical axial field gradients of 11.5 G/cm, and equatorial field gradients of 6.75 G/cm.

In order to provide adequate heat dissipation in the magnet coils, water from a closed-loop heat exchanger is circulated through the coils. Operating temperatures of the magnet coils range from 28°C in the winter to 40°C in the summertime. Failure to monitor the operating temperature can lead to the catastrophic melting of the insulation, which requires re-wrapping the magnet coils.

Additional coils are placed on the chamber to null any stray magnetic fields and to provide fine control over the position of the trapped atoms in the vacuum chamber. These coils are positioned to provide fields along the z and $(x - y)$ axes. They are made of ribbon cable and have about 150 and 1250 turns, typically carry currents of 0.5 and 0.1 amperes, and typically produce fields of up to 0.75 and 2 G, respectively.

Monitoring the Trapped Atoms

By imaging the radiation from the spontaneous decay of the trapped atoms onto a linear CCD array, we are able to measure the number of atoms in the $5p_{3/2}$ state in the trap. The system was calibrated by imaging the radiation from one of the frequency stabilized diode lasers onto the head of a pin, and measuring the power collected, as well as its spatial extent. The system has a calibration factor of 3587 atoms/(V·μs) plus an additional factor of 6.61 for a filter placed in front of the CCD array to block the 480 nm pulsed laser light. Using this calibration factor, we infer that the trap has a typical radius of 750 μm, with a population ranging from 2×10^4 to 6×10^6 atoms. The resulting densities range from 3×10^7 to 2×10^9 atoms/cc, respectively.

2.3 Production and Detection of Rydberg Atoms

As we do it, the production of Rydberg atoms requires two photons, and is greatly simplified by the presence of the trapping lasers. The Rb atoms are excited from the ground $5s_{1/2}$ state to the $5p_{3/2}$ state via the trapping lasers. Although the $5p_{3/2}$ state has a lifetime of 27 ns, the atoms in the trap are continuously absorbing and re-emitting photons to produce a steady-state population of atoms in the $5p_{3/2}$ state, generally equal to one-half the total trap population for our trap. Thus we can excite directly to the Rydberg states from the $5p_{3/2}$ state with a single additional photon,

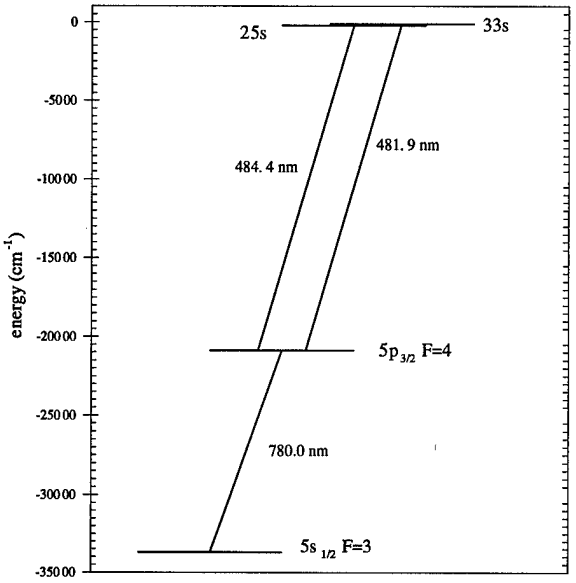

Figure 2.5: Laser frequencies used to prepare the initial atomic states in the magneto-optical trap for study. The 780nm lasers are CW diode lasers, while the 480nm lasers are pulsed dye lasers. The arrival of the pulsed dye lasers signals the beginning of the interaction period in the absense of a static field tuning pulse. The states accessed are for the experiment described in Chapter 3.

as shown in Fig. 2.5.

From the $5p_{3/2}$ state, the atoms were excited to Rydberg states using pulsed dye lasers producing $\sim$ 6 ns pulses of $\sim$ 482 nm light at a 20 Hz repetition rate. The dye lasers were used to produce atoms in states with principal quantum numbers $21 < n < 50$. These states are accessible from the $5p_{3/2}$ state with photons between 484 and 480 nm. The ionization limit lies 20,875 cm^{-1} above the $5p_{3/2}$ state, corresponding to one 479 nm photon. Lasers of several different configurations were used for state preparation. If multiple initial states were required, the laser pulses were roughly overlapped in space and time using a polarizing beamsplitter. The Rydberg lasers

were also focused onto the trap volume. The measured beam waist diameter at the focus is 129±20 μm for the geometry used in these experiments. The pulsed lasers typically transfer up to 10% of the $5p_{3/2}$ population into a given initial state.

Efficient excitation of trapped atoms into Rydberg states is hampered by their low temperature. The finite lifetime of an excited atomic state contributes to the width of an optical transition. This width, $\delta\nu_n$, is given in Rb by

$$\delta\nu_{n,l} = \frac{1}{2\pi\tau_{n,l}} = \frac{1}{2\pi\tau_o(n*)^\alpha}, \tag{2.7}$$

where the parameters τ_o and α are:

	s	p	d	f
τ_o (ns)	1.43	2.76	2.09	0.76
α	2.94	3.02	2.85	2.95

Table 2.1: Lifetime parameters for Rb using Eq 2.7[48].

For the $25d$ state, $\delta\nu_{25d} = 9.25$ μs. The width of the $5p_{3/2}$ state, which has a lifetime of 27 ns, is 5.9 MHz and also contributes to the width of the optical transitions. As such, the natural widths of the excitation processes we use are essentially given by the width of the 5.9 MHz width of the $5p_{3/2}$ state.

At low pressures, the natural linewidth is broadened by the Doppler width of the

transition, which results in a Gaussian profile of width

$$\delta\nu_D = 7.16 \times 10^{-7}\ \text{Hz} \cdot \nu_o \sqrt{\frac{T}{M}}, \tag{2.8}$$

where ν_o is the center frequency of the transition, T is the temperature of the gas in question, and M is the mass in atomic mass units[46]. At room temperature, Eq. 2.8 gives $\delta\nu_D \approx 1$ GHz, far in excess of the radiative widths. For Rb atoms at 140 μK, this gives $\delta\nu_D \approx 200$ kHz for a $25d$ Rydberg state, which is smaller than the natural width of the transitions. Thus, the frequency of a dye laser exciting a Rydberg state in a MOT must be much more accurate than one used to excite a room temperature vapor in order for excitation to occur. The MOT Doppler width is far more narrow than the pulsed laser linewidths, and therefore mode structure of the laser will play an important role in the stability of the excitation signal. This problem prompted the development of the short-cavity dye laser discussed in Sec. 2.3.1.

2.3.1 Dye Lasers

Three separate configurations of dye lasers were used in the experiments described in the following chapters. These are the Hänsch[49], the Littman[50], and the short-cavity (single-mode) Littman[51]. The lasers differed primarily in their geometric configurations, power output, and linewidths. However, each of the lasers used LD-473 laser dye, mixed with methanol at a concentration between 400 and 600 mg/L.

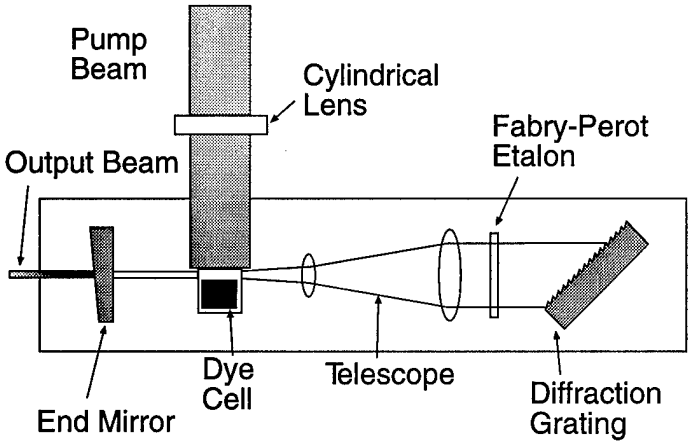

Figure 2.6: Diagram of a Hänsch cavity laser, used in several of the experiments described. The pump laser beam, in this case 354.7 nm light from a frequency-tripled Nd:YAG laser, passes through a cylindrical lens and is focused just inside the dye cell. Light emitted from the relaxing dye molecules forms the gain medium between the diffraction grating on the right and the partially reflecting mirror on the left. The telescope expands the output from the dye cell which serves to illuminate more lines on the grating and reduce the intensity. The optional etalon may be inserted once the cavity is lasing, and serves to reduce the linewidth of the laser.

This provided a reasonable excitation efficiency to the desired Rydberg states for each configuration used. Additionally, all lasers utilized harmonics of a Continuum YG661 Nd^{3+} doped $Y_3Al_5O_{12}$ (Nd:YAG) laser for pumping. The Nd:YAG laser produces 600 mJ/pulse of 1064 nm light at a repetition rate of 20 Hz. Each $\sim$ 5 ns pulse is sent through a pair of KDP harmonic generating crystals to produce light at 532 nm (130 mJ/pulse) and 354.67 nm (60 mJ/pulse).

Hänsch Cavity Lasers

The Hänsch cavity configuration utilizes a cylindrical lens to focus the pump beam into a narrow line which excites molecules flowing through a 10 mm long dye cell, as

shown in Fig. 2.6. Light radiated by the dye molecules travels outward transversely to the pump beam. The laser cavity is formed by a partially reflecting mirror (usually a 3° wedge window) and a diffraction grating. The total cavity length is generally quite long, about 30 cm, providing for very few (4-6) light passes during the time the dye is active. This requires that the dye provide high gain for the desired wavelength. A telescope is placed between the dye cell and the diffraction grating in order to illuminate more lines on the grating. Additionally, the telescope collimates the light incident on the grating and reduces its intensity.

The diffraction grating is mounted such that the Littrow order is reflected back through the telescope into the laser cavity. In such a configuration, linewidths of approximately 1 cm^{-1} are easily achieved, with powers reaching 0.5 mJ/pulse. To achieve a narrower linewidth, a Fabry-Perot etalon is placed in the laser cavity between the telescope and the diffraction grating. This substantially reduces the linewidth, to approximately 3 GHz, or 0.1 cm^{-1}. Although the total output power is reduced, the power available for excitation of an atom generally increases with the etalon in place as less of the light is outside the linewidth of the driven transition. As a result, shot-to-shot variation in the signal is substantially reduced with an etalon in place. In general, Hänsch lasers tend to work best for the lower Rydberg states (lower in energy than the 27s state), where their high power provides good excitation, and their relatively poor linewidth is not too severe a penalty.

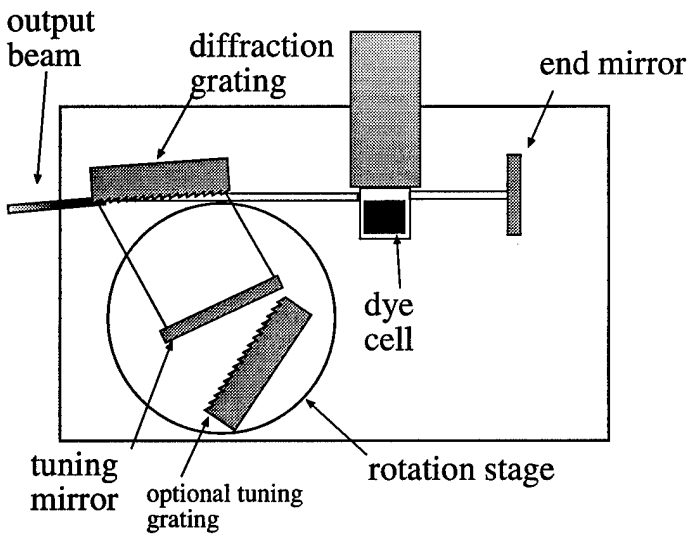

Figure 2.7: Schematic diagram of a Littman cavity laser. The pump beam again is focused just inside the dye cell. Light emitted from the dye molecules forms the gain medium between the tuning end mirror on the right and the tuning mirror on the left. In some cases, a second diffraction grating is used as the tuning element, replacing the tuning mirror.

Littman Cavity Lasers

The Littman cavity configuration also utilizes a cyclindrical lens to illuminate a line of dye molecules flowing in a 10 mm long dye cell. Light radiated by the dye molecules travels outward towards a highly reflective end mirror which forms one end of the laser cavity. Light travelling the opposite direction strikes a diffraction grating at grazing incidence ($\theta_0 \approx 89°$). Light diffracts from the grating and continues towards a tuning mirror placed on a high-precision rotating mount, which is used to feed back light of the appropriate wavelength, as shown in Fig. 2.7. Light on the return trip is further dispersed by the grating, which enhances the separation between different wavelengths in the cavity. For a given angle of incidence, Θ_i, and diffraction angle,

Θ_d, the wavelength of the laser light is given by

$$\lambda = \frac{d}{m}[\sin(\Theta_i) + \sin(\Theta_d)], \tag{2.9}$$

where d is the spacing of the grating, and m is the order of the diffracted light.

Because the light oscillating in the laser cavity strikes the tuning grating twice in a round trip, the grating chosen for use in the cavity must have reasonable single pass efficiency, as the net efficiency of the cavity will depend on the square of the grating efficiency. All Littman lasers used in these experiments used 3600 line/mm gratings manufactured by American Holographics specifically for use in grazing incidence dye lasers. At the wavelengths used, these gratings have single pass efficiencies between 5 and 10%, depending on the angle of incidence, and provided the light is polarized perpendicular to the grooves. The laser output is the zero order reflection from the grating.

The Littman cavity configuration produces spectrally narrow output, generally having linewidths less than 3 GHz, and of reasonable power (typically 150 μJ/pulse). However, their linewidth can be improved using a modification shown in Fig. 2.7. In this configuration, the tuning mirror is replaced with a second diffraction grating. This tuning grating is mounted such that the Littrow order is reflected back into the cavity. Because gratings can have efficiencies approaching 60% for visible light reflected into the Littrow order, there is not a significant loss in cavity efficiency,

but the linewidth of the output can be substantially narrowed with this additional frequency-dispersive element placed in the cavity. Care must be taken not to insert the grating into the cavity backwards, so that its dispersion cancels that of the first grating. Further, using a piezo-electric transducer (PZT) controlled optical mount to position the tuning grating allows extremely precise tuning of the laser to the required state. This feature is especially useful when exciting states of high principal quantum number or when exciting states in electric fields, where the spacings between adjacent states can be quite small.

The output of the Littman or Hänsch laser may be amplified using a single-pass, transversely-pumped dye amplifier. Amplified lasers typically have a factor of 10 or more power than their non-amplified oscillator output, without significant penalty to the laser linewidth.

Short-Cavity Design Littman Lasers

The short-cavity design grazing incidence laser was the product of the desire to have a continuously tunable pulsed dye laser. In order to continuously tune a laser cavity without mode hops, one must change the physical length, L, of the cavity, such that the relation $\lambda = 2 \times L/N$, is always true (here N represents the mode number of the cavity). Because the Hänsch and Littman cavity lasers described above have a very ill-defined optical axis, it is difficult to determine the actual cavity length, and as such, these lasers tend to run in multiple longitudinal modes. There were two

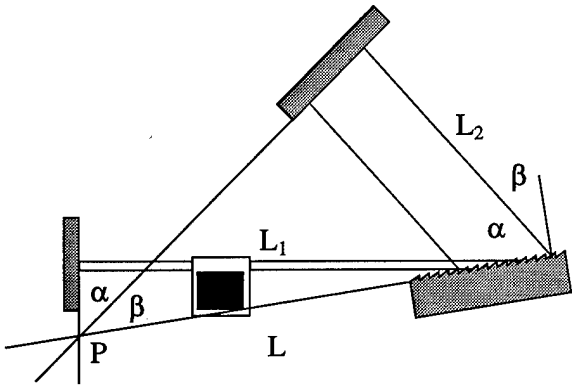

Figure 2.8: Arrangement of the pivot point of a dye laser which allows for continous mechanical tuning of the laser in a single mode. By rotating the tuning mirror around the axis defined by the intersection of the planes of the end mirror and the grating surface, the cavity changes such that the output wavelength defined by Eq. 2.9 and the cavity length change in the same manner. This is easily seen as the cavity length, $L_1 + L_2 = L\sin\alpha + L\sin(\alpha+\beta)$, has the same functional form as Eq. 2.9.

problems that therefore had to be overcome to produce a single-mode pulsed dye laser: continuous scanning of the cavity length and producing a well-defined optical axis. The first problem was solved by Liu and Littman, when they discovered that by pivoting the tuning mirror of a Littman configuration laser about a certain axis the cavity length will change continously as one changes the angle of the tuning mirror. This axis is defined by the intersection of the surface planes of the end mirror, the tuning mirror, and the diffraction grating[52], This is shown in Fig. 2.8. Should a second grating be used instead of the tuning mirror, this relationship does not quite hold.

To better define an optical axis, a longitudinal pump configuration was adopted. By tightly focusing the pump light onto the dye cell, an effective pinhole is introduced

into the laser cavity, providing a well-defined axis. Finally, the overall cavity length was dramatically shortened. This separates the cavity modes further in frequency and allowed light within the cavity to complete several round trips within the duration of the pump pulse, which was necessary as the smaller cavity and longitudinal pumping resulted in much lower single-pass gains than the transversely-pumped designs[51]. A convenient side-effect of the lower single-pass gain of the longitudinally pumped laser is the elimination of the majority of the amplified stimulated emission (ASE) present in the transversely-pumped lasers. Linewidths of these lasers can approach the transform limit of the pump pulse. General information on lasers of this design may be found in Littmann[53], Corless, *et. al.*[54], and references therein.

In order to achieve more stable excitation of the trapped atoms into Rydberg states, a short-cavity Littman dye laser (SCDL) was constructed. The laser design is shown in Fig. 2.9, and is adopted from [51]. A detailed equipment list follows in Table 2.2.

The design attempts to minimize misplacement of the pivot point by centering the rotation stage beneath the platform on which the remaining optics are mounted. By fixing the pivot point to a marked position on the baseplate, accurate visual alignment can be made. Small adjustments to the position of the end mirror are made with a PZT, which serves to fine tune the cavity length. The minimal ASE of the longitudinal pump configuration makes it necessary to insert a microscope slide in the cavity between the dye cell and the diffraction grating during initial alignment.

Assembly	Company	Part Number	Description
Rotation Stage	Oriel	13021	Large precision rotator
	Oriel	13085	2.75" Rotator top adaptor, English thread
End Mirror	CVI	TLM1-500-0-0537	0.5" High power mirror, $\lambda_{center} = 500$ nm
Gratings	American Holographic		10x25x10 Al coated, 3600 l/mm
	American Holographic		10x25x10 Al coated, 2400 l/mm
Focusing Lens	Newport	SPX-031	500mm PCX quartz lens
Dye Cell	NSG Precision Cells	T-506	2mm path length micro dye cell
Opto-mechanics	Newport	MM-100 (x2)	1"x1" optic mount
	Newport	MM-200	2"x2" optic mount
	Newport	BP-1 (x2)	1" base plate
	Newport	BP-2 (x2)	2" base plate
	Thorlabs	AE0505D08	Dual Stack piezo-electric transducer
	New Focus	9783	Micro mirror mount
Dye Pump	Cole-Parmer	H-07144-05	Continuous-duty Motor and controller system
	Micropump	H-07002-25	0.017 ml/rev pressure loaded (D) pump head

Table 2.2: Main components used in the assembly of the short-cavity dye laser used in the experiments.

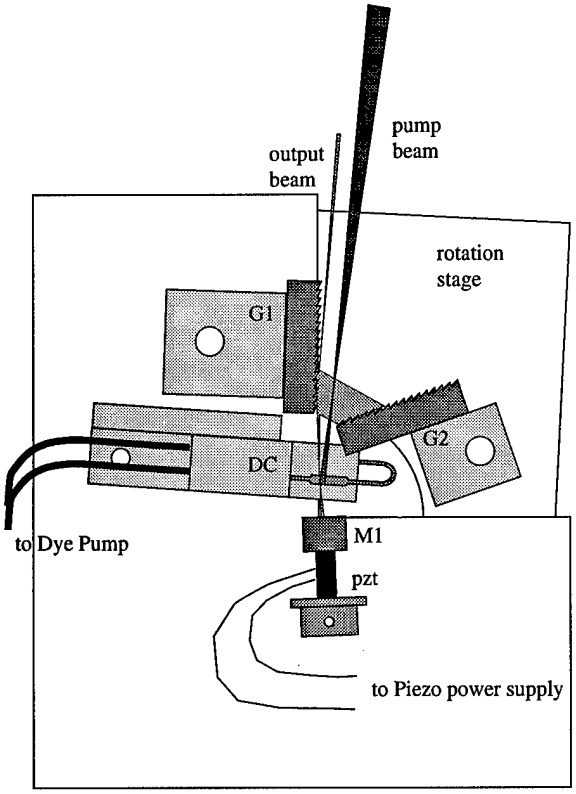

Figure 2.9: Schematic drawing of the short-cavity dye laser used in these experiments. The pump beam is directed down into the cavity at a slight angle, and is focused in front of the dye cell as shown. The faces of the dye cell are tilted with respect to the other surfaces of the cavity to prevent etaloning. For intial alignment, a microscope slide is placed between the dye cell and G1.

By aligning the slide and the end mirror to form a resonator cavity, a beam is created with which one may align the remaining optics. When it is apparent that the main cavity is lasing (in addition to the resonator), the microscope slide is removed. Small adjustments in the tilt of the tuning grating will then bring the cavity into lasing, compensating for the slight change in the optical axis caused by removing the slide. Further optimization of the cavity generally includes adjustments of the incidence angle of the first grating and slight displacements of the pump beam. Care should

be taken not to insert the slide into the pump beam, as this will make alignment on removal of the slide much more difficult due to displacement of the pump beam.

There are several details requiring special attention. First, the pump beam should range from 500 to 650 μJ per pulse. Pump powers in excess of these numbers will quickly burn holes in the dye cell surface and can damage the gratings via reflections. Second, it is a good idea to focus the pump beam in front of the dye cell, to further avoid damaging the cell. For a nominal 600 μJ/pulse pump beam, the focus should be located about 1.5 cm in front of the cell. Third, it is important to polarize the pump beam in the plane of the table (orthogonal to the grooves of the grating, or π-polarization), as the efficiency of the grating is much better for π-polariztion than for σ-polariztion. Fourth, care should be taken to ensure a good transverse beam profile. The pump beam profile determines the transverse mode of the dye laser, and also forms the virtual pinhole that accurately defines the optical axis of the cavity. As a result, the pump beam should not be steered into the cavity using a microscope slide, as this will create a second pinhole in the dye cavity, which can damage the grating should this second beam focus onto its surface. Finally, it is also easier to direct the pump beam into the dye cell with a slight descent. This makes directing the output beam easier, as the two beams can often come out such that they are very close together. Directing the pump beam down into the dye cell increases the separation while not affecting the beam quality.

The output of the SCDL will generally exhibit large fluctuations in intensity,

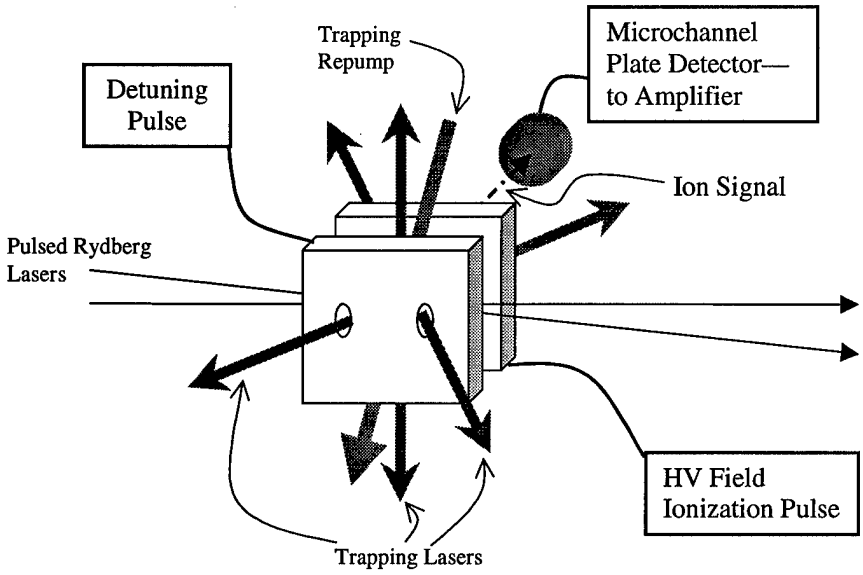

Figure 2.10: Schematic of atomic trap, including trapping lasers. Also shown are the field plates, used for selective field ionization of final state atoms, and the pulsed dye lasers used for initial state preparation.

which are minimized by sending the output through two transversely-pumped dye amplifiers, the second of which is saturated. The resulting beam exhibits a time-averaged linewidth capable of completely separating the $|m_j = 1/2|$ and $|m_j = 3/2|$ levels of the $30p_{3/2}$ state at an electric field of 20 V/cm; the states are separated by about 250 MHz, implying a linewidth of less than 500 MHz.

2.3.2 Electric Field Generation

As shown in Fig. 2.10, the trap volume was located approximately midway between a pair of vertical copper plates spaced 1.909 cm apart. These plates provide a means for introducing non-zero electric fields to the atoms in the trapped volume. This is done

in several ways. The first is the application of a slowly rising high voltage ionizing field pulse, typically rising between zero and 500 to 2000 V/cm in about 1 μs. Secondly, a tuning field may be applied to Stark shift the energies of the various Rydberg states into and out of resonance. This may be done by pulsing small voltages onto the plates (typically less than 50 V/cm) with fast risetimes ($\approx$ 10 ns), or by varying the potential difference between the plates with a static voltage.

The ionizing pulse and the static field voltages are applied to the field plate farthest from the detector (see Sec. 2.3.3). The pulse is produced by charging a 1.0 μF capacitor with an HP 2612B DC power supply. A trigger pulse triggers a silicon-controlled rectifier (SCR), which dumps the stored charge through the primary coil of an ILC model T228 transformer. The pulse is amplified by a factor of about 70. The high voltage side of the secondary coil is attached to the field plate farthest from the detector, while the low voltage side is attached to a DC power supply (Kepco APH500M) used to provide a static field offset. The signal is sent into the chamber through one pin of a eight pin Varian UHV high-voltage feedthrough.

Fast-risetime tuning field voltages are sent to the field plate closest to the detector. Because the voltages applied to this plate do not pass through the transformer, they are capable of carrying much higher frequency components, and therefore may have extremely fast risetimes. As such, application of these pulses is used to accurately control interaction times for the atoms in the trap volume.

The field plates each have two 0.375 inch holes drilled through them at a 45°

angle to allow the trapping beams to pass. The holes are covered with a fine copper mesh composed of twenty 0.00127 inch copper wires per inch. This is intended to improve field homogeneity between the plates while allowing ample clearance for the trapping lasers. In the center of the plate nearest the detector there is an array of 0.020 inch diameter holes providing an exit for the ions produced by the field ionization pulse.

2.3.3 Charged particle detection

Due to the low binding energies of Rydberg states of atoms, modest electric fields are capable of stripping the valence electron from the atom. The required ionization voltage is determined by the state of the atom, and its magnitude is proportional to $1/16n^4$. The difference in the threshold ionization voltage between adjacent states is often sufficient to differentiate between these atomic states. Application of a ramped pulse will ionize the highest states earliest in time. By placing a charged particle detector in the direction of travel of either the electrons or ions produced, we can measure the time dependence of the signal to determine which states were present in the trapped volume. As mentioned in Sec. 2.3.2, we detect the ions produced by the pulse. We do this with a dual microchannel plate (MCP) detector placed to the left of the field plates. After the ions pass through the small holes in the field plates they strike the front MCP, across which is a potential difference of between 600 and 1000 V. Photons or charged particles incident on the front face of the MCP will

induce a rush of electrons down the channels. An avalanche of electrons with a voltage dependant gain of between 600 and 6000 will then impinge on the second plate, which repeats the process. The electrons from the second plate strike a collector which then sends the current through a Varian shielded HV feedthrough before being amplified by a Hewlett-Packard 462A or MiniCircuits ZDL-500 amplifier. The output of this amplifier is then monitored on a Tektronix 2440 oscilloscope. A SRS Model SR250 gated integrator measures the signal collected at a specific time corresponding to a given Rydberg state and sends the result to a microcomputer. The microcomputer averages the signal for a given set of conditions over many shots of the laser, changes the conditions such as tuning voltage or resonance interaction time, and stores the results for later retrieval and analysis.

Chapter 3

Quasistatic Resonant Dipole-Dipole Interactions

3.1 Introduction

Resonant energy transfer collisions, in which the total internal energy of the colliding partners remains constant, have long been studied in Rydberg atoms [4, 10]. Two reasons for this are the particularly large dipole moments found in Rydberg atoms, resulting in correspondingly large cross sections, and the rich Stark structure found in the atoms, which allow one to tune energy levels into and out of resonance. The relative velocity of the colliding partners determines a characteristic collision time, and correspondingly, the width of these resonances. One would expect, therefore, that the width of the resonance would scale inversely with the relative velocity of the colliding atoms [11]. In fact, a $v^{-3/2}$ scaling is expected. Previous experiments using velocity selected atomic beams [55, 56] have demonstrated this to be true for a broad range of conditions.

However, there are situations where the assumptions inherent in this description break down. In particular, observations of line broadening in a dense room temperature Rydberg gas by Raimond *et. al.* [57] require the use of a quasistatic, rather than a dynamic, description of the processes occuring in the experiment. This occurs when the spatial separation of the atoms is small enough that the average interatomic interaction is observable. When these distances are comparable, it becomes necessary to consider three- and four-body collisions. While our densities do not quite reach those of Raimond *et. al.*, our experiments are performed in a magneto-optical trap, or MOT, at temperatures less than 300 μK where the atoms under study move only a small fraction of their separation during the time scale of the experiment. Any interactions observed between atoms will therefore depend on the essentially constant relative spacing, and one can expect that more than one atom might be considered for interaction with a given partner. This results in a situation analagous to an amorphous solid, where the energy levels of the individual atoms form energy bands due to the many-atom interactions.

The nature of the many-body interaction in a resonant energy transfer reaction is not totally understood for a dense, frozen Rydberg gas. Recent studies have left several questions unanswered [58, 59]. Specifically, they have not examined the time dependence of the energy transfer process, and have measured line-broadening only over a limited range of densities. In this chapter we shall attempt to clarify the many-atom, non-binary mechanism for energy transfer in such a system. We shall then

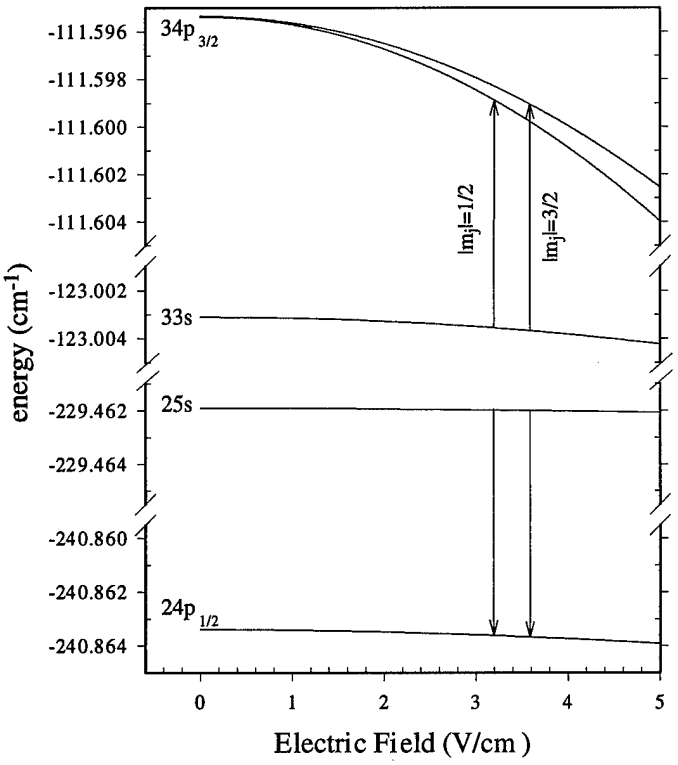

Figure 3.1: Energy levels of Rb as a function of electric field showing the resonant energy transfer interactions of Eq. 3.1

present the results of resonant energy transfer experiments performed on Rydberg atoms prepared in a MOT which corroborate the many-body picture of resonant energy transfer reactions in a cold, dense Rydberg gas.

3.2 Description of Energy Transfer Process

We start our explanation by considering an energy resonance for a two-atom collision system in ^{85}Rb. In this two-atom picture, we are investigating the reaction of two Rb

atoms

$$25s_{1/2} + 33s_{1/2} \rightarrow 24p_{1/2} + 34p_{3/2}, \tag{3.1}$$

which we assume to take place at room temperature. The collision is resonant at the electric fields $E = 3.0$ and 3.4 V/cm for the $|\, m_j \,| = 1/2$ and $|\, m_j \,| = 3/2$ levels of the $34p_{3/2}$ state, as seen in Fig. 3.1. Recalling Eq. 1.15, the cross section for such a binary collision is

$$\sigma = \frac{\mu\mu'}{v} \approx b^2. \tag{3.2}$$

Here μ and μ' represent the $25s$-$24p$ and $33s$-$34p$ electric dipole moment matrix elements, while v is the collision velocity, and b is the impact parameter. In atomic units, $\mu = 492ea_0$ and $\mu' = 126ea_0$. Likewise, we recall from Eq. 1.16 the collision linewidth $\Delta\nu$ is the inverse of the collision duration τ

$$\Delta\nu = \frac{1}{\tau} = \frac{v^{3/2}}{\sqrt{\mu\mu'}} = \frac{v}{\sqrt{\sigma}}. \tag{3.3}$$

Applying Eqs. 3.2 and 3.3 at $T = 300$ K, we calculate $\sigma = 10^{-8}$ cm^2 and $\Delta\nu = 380$ MHz, while at $T = 140$ μK, typically found in our MOT, we find $\sigma \approx 10^{-5}$ cm^2 and $\Delta\nu \approx 10$ kHz. Finally, in our MOT, we have a typical density of atoms in the initial state of $\rho_0 = 1 \times 10^9$ atoms/cc, and they are $N_0 = 10^7$ in number. We can

then calculate the average interatomic spacing,

$$r_0 = \left(\frac{3}{4\pi\rho_0}\right)^{1/3}, \tag{3.4}$$

finding that $r_0 \approx 6.2$ μm, notably less than the impact parameter calculated from the two-body cross section ($b = \sqrt{\sigma} \approx 30$ μm). At this density, as noted by Anderson *et. al.* [58] and Mourachko *et. al.* [59], the effects observed are clearly not due to a purely binary collision.

The collision velocity for a binary collision at 140 μK is given by

$$v = \sqrt{\frac{8kT}{\pi M}} = 26 \text{ cm/s}, \tag{3.5}$$

where M is the reduced mass of the colliding Rb atoms. This implies the atoms move approximately 0.5 μm, or 0.08 b during the 2 μs course of our experiment. It is therefore likely that in a 140 μK gas, the process described by Eq. 3.1 is quasistatic in nature [60] and is not a collision. We are therefore faced with the problem of describing the resonant energy transfer process which is occurring in a different manner.

3.2.1 Resonant Energy Transfer in a Quasistatic Picture

In order to represent the quasistatic resonant energy transfer process analagous to the room temperature collision given by Eq. 3.1, we must make some simplifying

assumptions. We start by assuming there are $N_0 = N_{25s} + N_{33s}$ atoms in the trap volume, with the additional restriction that $N_{25s} \approx N_{33s}$. We further assume the atoms to be motionless, and separated by distances r_{ij}, such that $\overline{r_{ij}} = r_0$. In short, we have a random distribution of atoms with a mean spacing such that we measure a density

$$\rho_0 = \frac{3N_0}{4\pi r_{trap}^3}, \tag{3.6}$$

where r_{trap} is the radius for the entire volume of trapped atoms.

Given this situation, the simplest approach to take would be to view the process much as one would an interaction betwen lattice sites in a solid, essentially the resonant analog of the work of Raimond, *et al* [57]. That is, we would expect to observe a binary resonance between atoms separated by the average spacing, r_0. For $r_0 = 6.2$ μm, we find $\Delta\nu = 240$ kHz, which is still far smaller than the observed widths of ~ 5 MHz.

For a distribution of atomic spacings as discussed above, there will be some atoms, N_c, spaced closer than a distance $r_c \ll r_0$. These pairs will have couplings strong enough to interact via Eq. 3.1 at detunings up to $\mu\mu'/r_c^3$ away from resonance. Given a typical distribution of separations, one would expect only a small fraction of atoms to have separations less than r_c, i.e. $N_c/N_0 < 0.01$. As noted by Anderson *et al.*[58] and Mourachko *et al.*[59],this number of atoms is too small to explain the magnitude of signals observed, as will be shown in Sec. 3.4.1.

Anderson *et al.* formulated the following simple model to explain the observed resonance phenomena. In addition to the resonant dipole-dipole interaction of Eq. 3.1, there are also two other dipole-dipole interactions which are always resonant. These are

$$25s_{1/2} + 24p_{1/2} \rightarrow 24p_{1/2} + 25s_{1/2}, \tag{3.7}$$

and

$$33s_{1/2} + 34p_{3/2} \rightarrow 34p_{3/2} + 33s_{1/2}. \tag{3.8}$$

These have interaction strengths

$$\frac{(\mu')^2}{r^3} \quad \text{and} \quad \frac{(\mu)^2}{r^3}, \tag{3.9}$$

respectively, and are the same interactions which are responsible for suppression of superradiance[61] and the self-broadening of resonance lines[60]. Those few pairs of atoms spaced closer than r_c will undergo the resonant transfer defined by Eq. 3.1 far off resonance, by up to $\mu\mu'/r_c^3$, which will lead to a larger linewidth. Those few atoms will then oscillate between the initial ($25s$ and $33s$) and final ($24p$ and $34p$) states with frequency $\mu\mu'/r_c^3$, on average spending half their time in the final states. While in the final states, the atoms may interact with other neighboring atoms in the $25s$ and $33s$ states via Eqs. 3.7 and 3.8, at rates given by Eq. 3.9. This cycle is repeated many times over the course of an experiment, allowing the p state population to diffuse

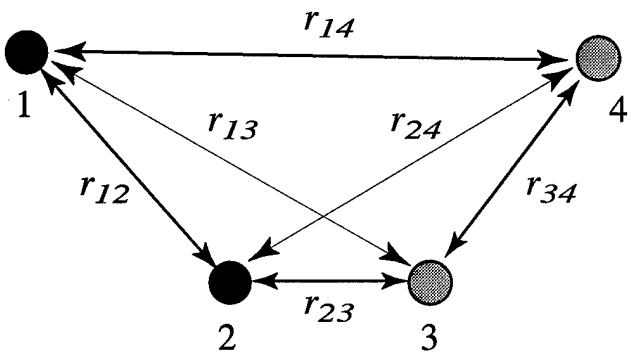

Figure 3.2: Diagram of atoms and typical spacings used in the four atom description of the resonant energy transfer process. The atoms are numbered 1 to 4 from left to right, and are initially in the states s, s, s', and s', respectively. The distances in microns between atoms are: $r_{12} = 2.3$, $r_{13} = 3.47$, $r_{14} = 4.3$, $r_{23} = 1.5$, $r_{24} = 3.17$, $r_{34} = 2.1$, and are chosen to represent a typical distribution of neighboring atom spacings. The lighter shaded atoms are meant to represent the atoms initially in the s' state.

away from the close atom pair, much like products in catalyzed chemical reactions move away from the initial reaction sites[62].

3.2.2 Resonant Energy Transfer in a Four-Atom System

If we examine the process outlined above in the simplest possible non-binary interaction, we see that the three processes of Eqs. 3.1, 3.7, and 3.8 are intertwined. Let us start by considering a static binary interaction between atom 2, which we excite to the $25s$ (or s) state, and atom 3, which we have excited to the $33s$ (or s') state, as shown in Fig. 3.2. The atoms are spaced by a typical nearest-neighbor separation of $r_{23} = 1.5$ μm. We form the wavefunction for this two-atom system by taking the ordered direct product of the individual atomic wavefunctions, i.e. $|\Psi\rangle = |ss'\rangle$, which we will call the molecular state of the system. In the absence of coupling, the energy

of this system will be $W_i = W_s + W_{s'}$. We now introduce the dipole-dipole coupling between the atoms, which we denote

$$\chi_{23} = \frac{\mu\mu'}{r_{23}^3} = 17 \text{ MHz}, \tag{3.10}$$

and which transfers atom 2 to the $24p$, or p, state and atom 3 to the $34p$, or p' state at the electric field for the resonance for the energy transfer interaction of Eq. 3.1, which we define as zero detuning. Away from resonance, the detuning is given by $\Delta = W_f - W_i$, where $W_f = W_p + W_{p'}$ is the energy of the final molecular state. The time-independant Schrödinger equation for this system is

$$\begin{pmatrix} 0 & \chi_{23} \\ \chi_{23} & \Delta \end{pmatrix} \begin{pmatrix} ss' \\ pp' \end{pmatrix} = W \begin{pmatrix} ss' \\ pp' \end{pmatrix}, \tag{3.11}$$

which has the energy levels shown in Fig. 3.3.

We now construct a model incorporating the four atoms shown in Fig. 3.2. The spacing between atoms 2 and 3 is less than the spacing between the remaining atoms, as is noted in the figure. We again form the molecular state of the system, which will initially be $sss's'$. Ignoring the weak prime-unprime couplings such as $s' - p$, there are six approximately degenerate states. In the absence of any couplings between the

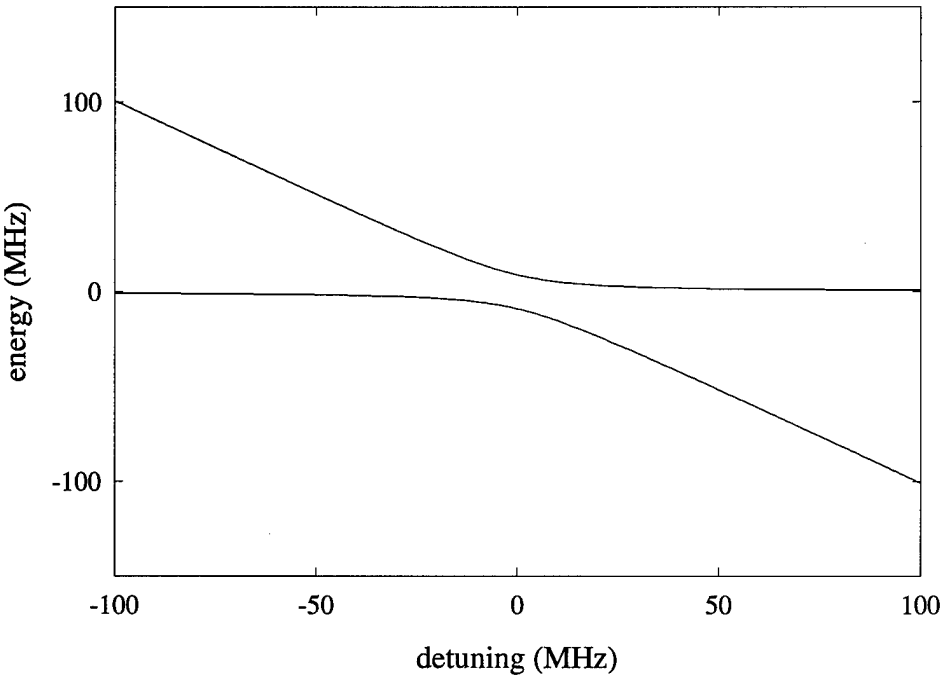

Figure 3.3: Energy levels for a two atom quasistatic interaction. The anticrossing formed at the resonance is of magnitude $\chi_{23} = 17$ MHz for the 1.5 μm spacing used in the calculation.

atoms, the time-independent Schrödinger equation is

$$W|\Psi\rangle = H_0|\Psi\rangle, \tag{3.12}$$

where

$$|\Psi\rangle = \begin{pmatrix} sss's' \\ sps'p' \\ spp's' \\ pss'p' \\ psp's' \\ ppp'p' \end{pmatrix}. \tag{3.13}$$

The energies of these states, which we label with subscripts $a - g$, are

$$W_a = 0 \quad W_b = \Delta \quad W_c = \Delta \quad W_d = \Delta \quad W_e = \Delta \quad W_g = 2\Delta. \tag{3.14}$$

Experimentally, we selectively field ionize atoms in the atomic state p'. Therefore, each of the molecular states other than $sss's'$ may be detected by our apparatus. However, the final molecular state $ppp'p'$ will produce a signal twice as large as that of the other molecular states. If we can find a way of coupling the first and last molecular states, we will have a method of producing more than one p' atom for a single close pair of ss' atoms. In other words, we can produce a larger signal than would be expected from the number of close atoms, and will have produced p-state excitation away from the site of the close atoms.

Couplings in the four atom system

We now introduce the effects of the the dipole-dipole energy transfer resonance of Eq. 3.1 into our four-atom system. If only the closest pair of atoms are coupled by the reaction of Eq. 3.1, the Hamiltonian for the system becomes

$$H_1 = \begin{pmatrix} 0 & 0 & \chi_{ac} & 0 & 0 & 0 \\ 0 & \Delta & 0 & 0 & 0 & 0 \\ \chi_{ac} & 0 & \Delta & 0 & 0 & 0 \\ 0 & 0 & 0 & \Delta & 0 & \chi_{ac} \\ 0 & 0 & 0 & 0 & \Delta & 0 \\ 0 & 0 & 0 & \chi_{ac} & 0 & 2\Delta \end{pmatrix}, \tag{3.15}$$

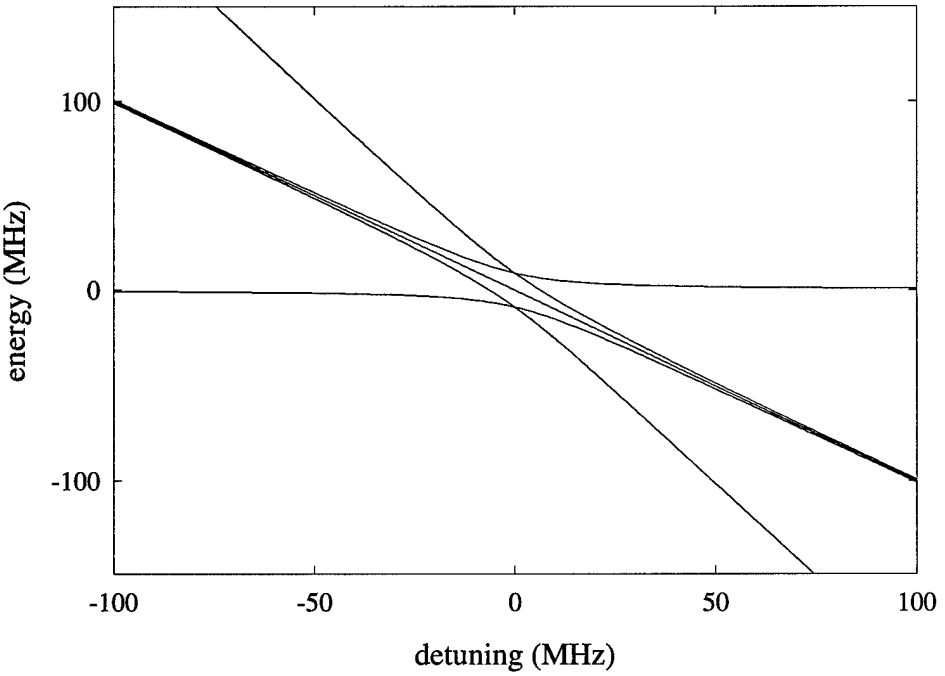

Figure 3.4: Energy levels for a four atom quasistatic interaction with only one coupling. Notice the coupling only partially lifts the degeneracy of the system near the resonance.

where $\chi_{ac} = \mu\mu'/r_{23}^3$ is the coupling between atoms 2 and 3, which connects the molecular states a to c (and also d to g). This interaction has two significant results. First, the initially prepared molecular state, $sss's'$ is no longer an eigenstate of the Hamiltonian, as is seen in Fig. 3.4. In other words, the prepared state evolves in time according to how it maps onto the new eigenstates of the total Hamiltonian. The prepared state will map onto the states $(sss's' \pm spp's')/sqrt(2)$. The partial lifting of the degeneracy of the molecular states will, after some allowed interaction time t_{int}, result in population in a molecular state which will allow us to observe atoms in the final atomic state p'. The measured signal for this process will be proportional to the

number of atoms, N_c, spaced close enough to interact. Were all such processes within the atomic trap perfectly coherent and all close atoms spaced by the same amount, we should observe beating in the final state population with a frequency χ_{ac}.

Having seen the effect of a single interaction, we now introduce the remaining dipole-dipole interactions, including those represented by Eqs. 3.1, 3.7, and 3.8. These are given by

$$\chi_{bd} = \frac{\mu^2}{r_{12}^3}, \tag{3.16}$$

$$\chi_{ae} = \frac{\mu\mu'}{r_{13}^3}, \tag{3.17}$$

$$\chi_{ad} = \frac{\mu\mu'}{r_{14}^3}, \tag{3.18}$$

$$\chi_{ab} = \frac{\mu\mu'}{r_{24}^3}, \tag{3.19}$$

$$\chi_{bc} = \frac{(\mu')^2}{r_{34}^3}. \tag{3.20}$$

The Hamiltonian for this system is given by

$$H = \begin{pmatrix} 0 & \chi_{ab} & \chi_{ac} & \chi_{ad} & \chi_{ae} & 0 \\ \chi_{ab} & \Delta & \chi_{bc} & \chi_{bd} & 0 & \chi_{ae} \\ \chi_{ac} & \chi_{bc} & \Delta & 0 & \chi_{bd} & \chi_{ad} \\ \chi_{ad} & \chi_{bd} & 0 & \Delta & \chi_{bc} & \chi_{ac} \\ \chi_{ae} & 0 & \chi_{bd} & \chi_{bc} & \Delta & \chi_{ab} \\ 0 & \chi_{ae} & \chi_{ad} & \chi_{ac} & \chi_{ab} & 2\Delta \end{pmatrix}. \tag{3.21}$$

The solutions to this Hamiltonian are shown in Fig. 3.5, which clearly shows the complicated nature of the interaction. There are several things to note; first, all

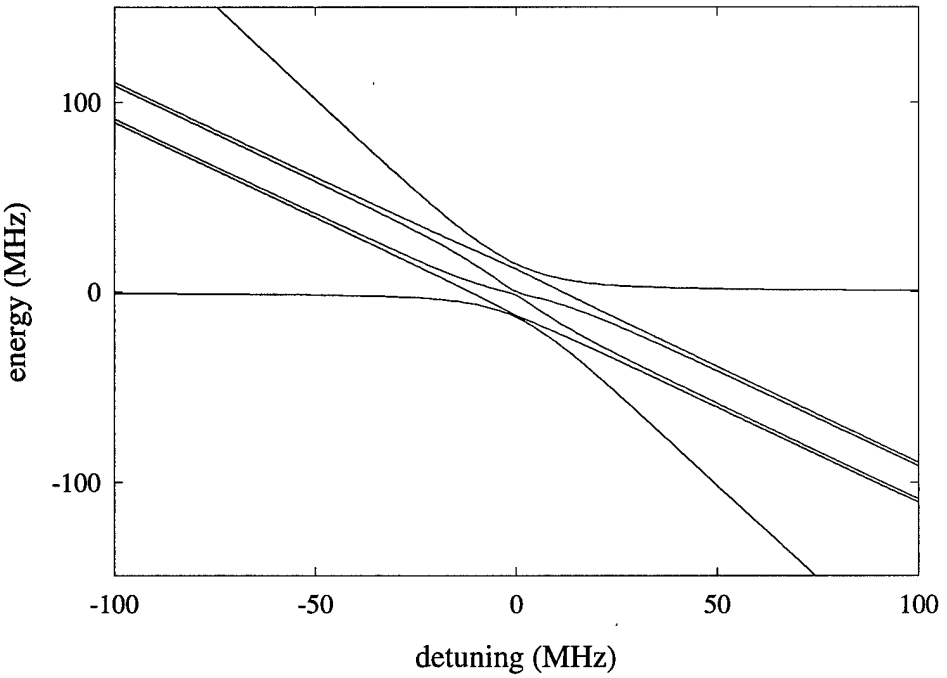

Figure 3.5: Energy levels for a four atom quasistatic interaction with all single-tranisition couplings. The couplings completely lift the degeneracy of the system and demonstrate a ladder-like structure in the area of the resonance.

degeneracies are lifted, even at large detunings. Second, note the band-like structure within the resonance. As the system sits near resonance, a given state will oscillate in the region of this structure. If the oscillations are strong enough, the population effectively climbs the ladder, ending up in a state which projects strongly onto $ppp'p'$ and thus provides transfer to the final p' atomic in excess of the number of close atom sites. Finally, notice the overall width of the resonance has increased from Fig. 3.4. The Hamiltonian of Eq. 3.21 includes all of the single-transition couplings. Having outlined a basic model to provide some insight into the physical phenomena, we can now look more closely at the experiment.

3.3 Experiment description

The energy resonance we studied, which for two atoms has the form given by Eq. 3.1, was observed in a magneto-optical trap [33], as described in Chap. 2. The Rb atoms in the trap were excited from the ground $5s_{1/2}$ state to the $5p_{3/2}$ state via the trapping lasers. From there, the atoms were excited to the Rydberg states using two Hänsch-style pulsed dye lasers (see Sec. 2.3.1, producing $\sim$ 6 ns pulses at a 20 Hz repetition rate, as shown in Fig. 2.5. The arrival of the laser pulses into the region of trapped atoms marks the beginning of the interaction period.

The laser pulses were roughly overlapped in space and time using a polarizing beamsplitter, and transferred approximately 10% of the overall trap population to each of the initial Rydberg states. Population transfer into the initial states was controlled by placing neutral density filters in the beam paths, before or after they were overlapped.

During some of the experiments, an additional pulsed dye laser, tuned to the 780 nm hyperfine transition, was sent into the chamber a few nanoseconds before the blue laser pulses arrive. This served to approximately double the number of atoms in the $5p_{3/2}$ state, thereby increasing both the number and the density of Rydberg atoms in the trap. When this method was used, an additional broad background signal was present due to resonant collisions with thermal atoms in the chamber.

Once we produced the initial states in the trap, we allowed them to interact in a

static field before applying a 10 ns risetime detuning pulse of about 10 volts, followed by a 1 μs risetime high voltage pulse to selectively field ionize those atoms in the final $34p_{3/2}$ state. We averaged this signal over many shots of the laser, during which time we used a computer-controlled digital-to-analog converter (DAC) to scan either the static field or the delay between the arrival of the pulsed lasers and the fast detuning pulse, i.e. the allowed interaction time t_{int}.

3.4 Data acquisition and analysis

In order to characterize the behavior of the energy transfer, several types of data were collected. In the first set of data, we scanned the static field across the resonances, allowing the interactions to proceed for 4.86 μs. These gave us information on the scaling of the width of the resonances as the density of atoms in the initial states was varied. In the second set of scans, we held the static field at the value corresponding to the peak of the $|m_j| = 3/2$ resonance, while scanning the interaction time between 0 and 4.85 μs, allowing us to monitor the time evolution of the signal at various densities of initial states. Finally, we looked at the time evolution of the entire resonance signal at two different densities to observe variations in the lineshape as a function of the allowed interaction time.

For the first two sets of data, both the overall and relative population of atoms in the initial states was varied. To vary the relative initial population in either the $25s_{1/2}$

or the $33s_{1/2}$ state, a neutral density filter was placed in the path of the appropriate pulsed dye laser. The overall population was changed in two ways. In the first, a pulsed dye laser tuned to the Rb $F = 2 \rightarrow 3$ transition was focused on the trap such that it arrived a few nanoseconds before the Rydberg lasers. This resulted in a temporary increase in the number of atoms in the $5p_{3/2}$ state, and gave an overall increase of a factor of two in the number of atoms in the initial states. In the second method, a neutral density filter was placed in the path of the repumping laser. This decreased the number of atoms in the $5p_{3/2}$ state, and therefore the number of atoms in the initial states by a factor corresponding to the attenuation of the filter. We now discuss each set of data individually.

3.4.1 Resonance scans and linewidth scaling with density

The result of each of the resonance scans was a set of linewidths corresponding to the $|m_j| = 1/2$ and $|m_j| = 3/2$ resonances. We used a non-linear least squares fit to a Lorentzian lineshape to determine these linewidths. The computer routine fit for both linewidths simultaneously, using the equation

$$f = y_0 + \frac{\alpha}{1 + \left(\frac{x-x_1}{\beta_1}\right)^2} + \frac{a}{1 + \left(\frac{x-x_2}{\beta_2}\right)^2}. \tag{3.22}$$

The fit parameters $2\beta_1$ and $2\beta_2$ are the full-widths at half maximum for the resonances, while x_1 and x_2 are the peak locations. Looking at Fig. 3.6, one can see that the

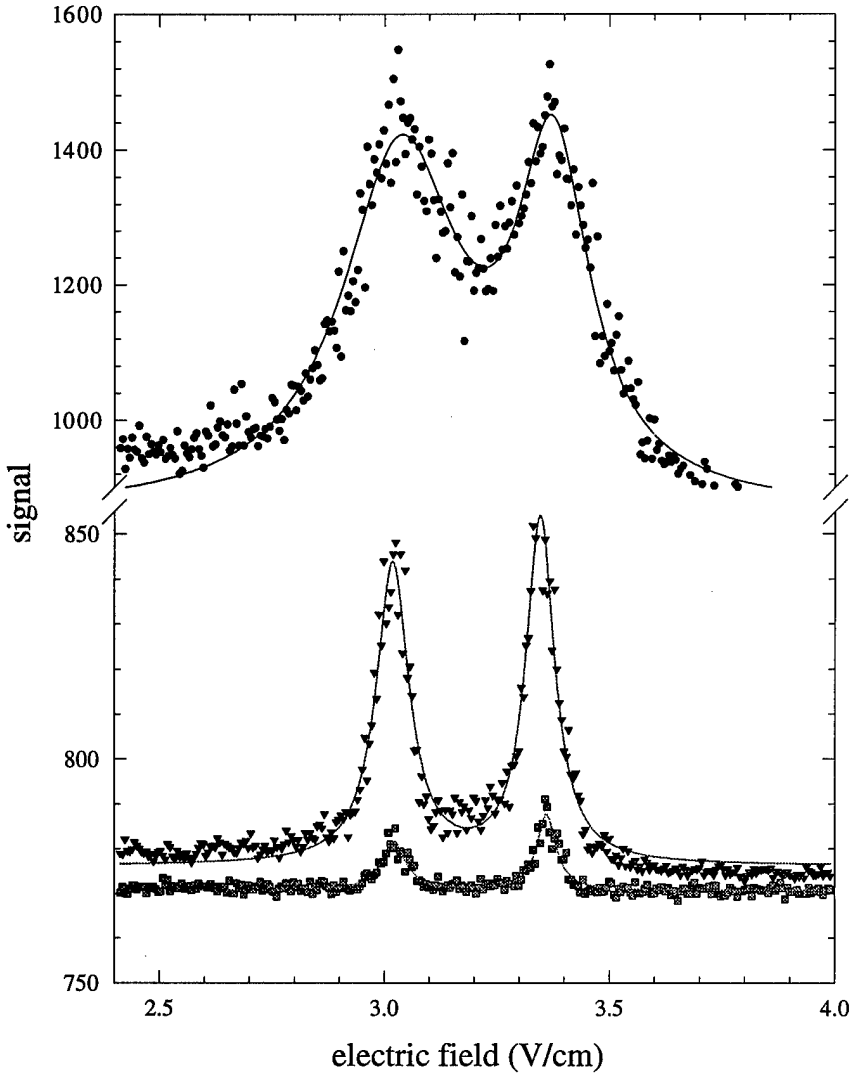

Figure 3.6: Energy transfer resonances measured for initial atomic state densities of 1.01×10^9 (circles), 1.81×10^8 (triangles), and 3.22×10^7 atoms/cc (squares). Solid lines indicate fits to dual-Lorentzian lineshapes with an overall offset. The apparent discrepancy in the widths of the $|m_j| = 1/2$ and $3/2$ resonances is due to the difference in the polarizabilites of the states. Measured average widths are 8.33, 1.25, and 0.93 MHz, respectively. The bottom data set (squares) is magnified by a factor of 6.64 relative to the other scans. Estimated peak population transfer is estimated at 25%.

resonances do not have a perfectly Lorentzian lineshape. However, the fits result in an accurate determination of the resonance widths. Note also that the characteristic deviations from a Lorentzian profile predict values too small near resonance, and predict values too large in the wings of the resonance.

The measured resonance widths ranged from 910 kHz to 8.4 MHz, as the density of the system increased from 3×10^8 to 2×10^{10} atoms/cc. Taking advantage of our ability to spatially sample the electric fields in the trapping region by moving the trap, we are able to measure an upper limit to the field inhomogeneity of about 0.003. For the measured interaction, this leads to a broadening of 0.20 MHz in the resonances. The variation in magnetic field strength experienced across the spatial extent of the trap will also contribute to the broadening of the resonances. The typical magnetic field gradient is $dB/dz = 14$ G/cm, leading to a resonance broadening of approximately 0.55 MHz for a typical 750 μm trap. We expect transform broadening due to the finite interaction time [63, 64] to contribute an additional 0.13 MHz to the resonance broadening, making the total experimental contribution to the linewidth 0.88 MHz, not too different from our observed minimum width of 0.91 MHz.

We have also investigated the change in linewidth as we alter the density in each of the initial atomic states individually. These results are shown in Fig. 3.7. The results demonstrate that the alteration of the relative density of one initial state have a much smaller effect on the width of the resonance, which we might expect from differentially scaling the interatomic spacings.

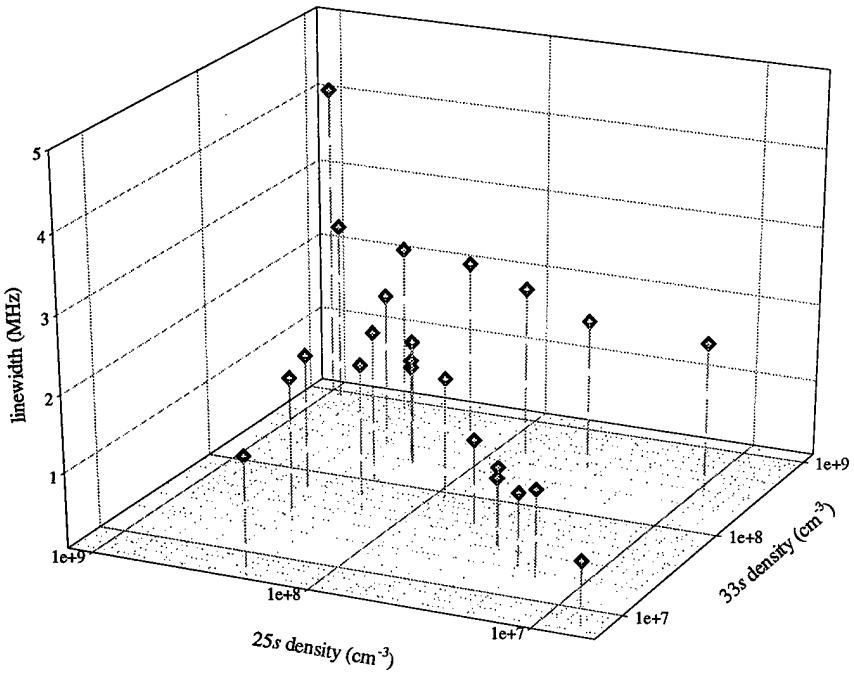

Figure 3.7: Resonance widths as a function of the density of each initial atomic state. Note the strong dependence on the density when both states are changed, while altering the density of only one state results in smaller changes in the observed linewidth.

3.4.2 Signal development with allowed interaction time

Initial investigation into the time characteristics of these dipole-dipole resonances characterized the behavior as consistent with the transform broadening seen by Thompson, *et al.* [64] in their experiments on resonant collisions in potassium. While we have observed transform broadening in this system, the growth of the resonant signal as a function of allowed collision time showed a somewhat different picture than might be expected.

Figure 3.8 shows a pair of these interaction time scans for two different initial

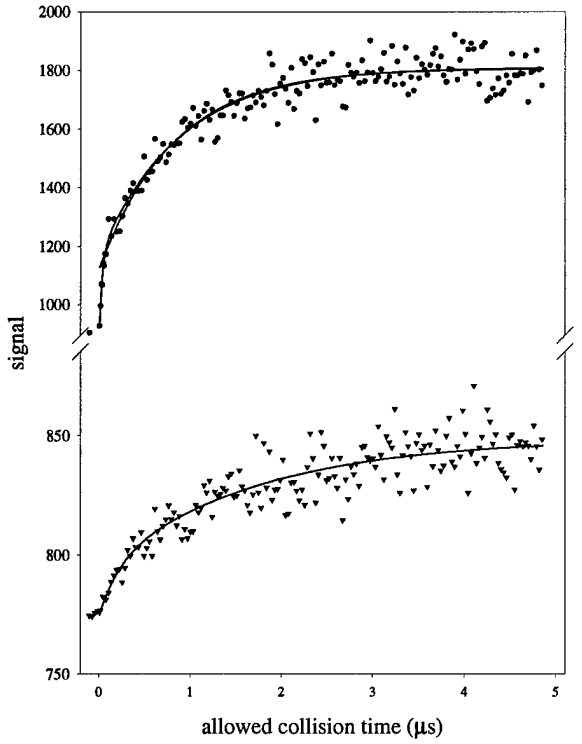

Figure 3.8: On-resonance signal evolution as a function of allowed interaction time for two different initial state atomic densities: 1.07×10^9 (circles) and 3.37×10^7 atoms/cc (triangles). Notice the sharp onset of signal for the higher density, consistent with rapid diffusion of p' excitation from the large number of closely spaced s' atoms. Only one-third of the data points are plotted for clarity. Peak population transfer is estimated at 25%.

state densities. The scans were fit to a dual exponential growth function:

$$f = y_0 + \alpha\left(1 - e^{-\beta_1 t}\right) + a\left(1 - e^{-\beta_2 t}\right). \tag{3.23}$$

The two characteristic growth times for these processes range from 140 ns and 4.8 μs to 1.35 μs and 60 μs, respectively. As can be seen in Fig. 3.8 (a), the majority of the on-resonance signal has built up in the first few hundred nanoseconds for the dense system, implying a characteristic width for the collisions on the order of 1.3×10^6 s^{-1}.

More interesting, the dual exponential nature of the signal growth appears to imply both a fast and a slow resonant process, consistent with the picture of multiple couplings between molecular states outlined in Section 3.2.1. The characteristic width of the slow process appears to be as low as 70 $\times 10^3$ s^{-1}.

On (or near) resonance, one would expect that the evolution of the signal would be dominated by the close atom couplings, χ_{ac} from Sec. 3.2.2, which can be as large as 100 MHz. For the closest of these close atoms, the remaining atoms in the four atom system will be close enough that the other couplings will be larger than the detuning. While this occurs in less than a percent of the total atoms, it is likely that the strengths of the interactions will lead to extremely rapid rates. We also see evidence of the weaker couplings, once we have saturated the strong interactions, in the slow risetime after a few hundred nanoseconds. Further from resonance, we would not expect that this difference should be so great, and we might also expect that the rate of signal increase should be less, implying that it is possible that we should see a time dependence in the lineshapes. We investigate that possibility in the next section.

3.4.3 Time dependance of lineshapes

The enhanced p' atom production near resonance for short times seen in Section 3.4.2 has interesting implications on the overall lineshape as observed for different interaction times. For a given interaction time, t_{int}, the overall level splitting will have the form shown in Fig. 3.5, but it is probable that the magnitudes of the individual

avoided crossings will change, becoming larger as more of the weaker couplings are able to occur. This should allow us to make some general statements about how the lineshape changes with interaction time. At small detunings, we know that we shall observe an increase in the rate of p' atom production at short interaction times, $t_{int} < \chi_{ac}$. At larger detunings, however, it is clear that the larger separations should dramatically decrease the transfer rate to the rate defined by the slower couplings. Thus we should not see a marked increase in the p' atom production rate at larger detunings, and the signal off-resonance will not increase as rapidly as we increase the interaction time. As a result, we expect that at short times we should see narrower resonances than at longer times, where the large-detuning signal can build up, contrary to observations of transform broadening, which predicts resonances will only get wider with decreasing interaction time[63].

To verify that this was indeed the case, a series of resonance scans was taken at various allowed interaction times, with the results shown in Figs. 3.9 and 3.10. Note the rapid growth of the signal on-resonance seen in Fig. 3.8 for higher density systems. This is consistent with our analysis above. The time dependence of the linewidth is more clearly seen in Fig. 3.10. Here the first scan of the series is partially transform broadened. As the interaction time increases, the linewidth decreases proportional to $1/t_{int}$. However, after a few hundred nanoseconds the linewidth begins to increase, as we might expect from our description of the multi-atom couplings in Sec. 3.2.2.

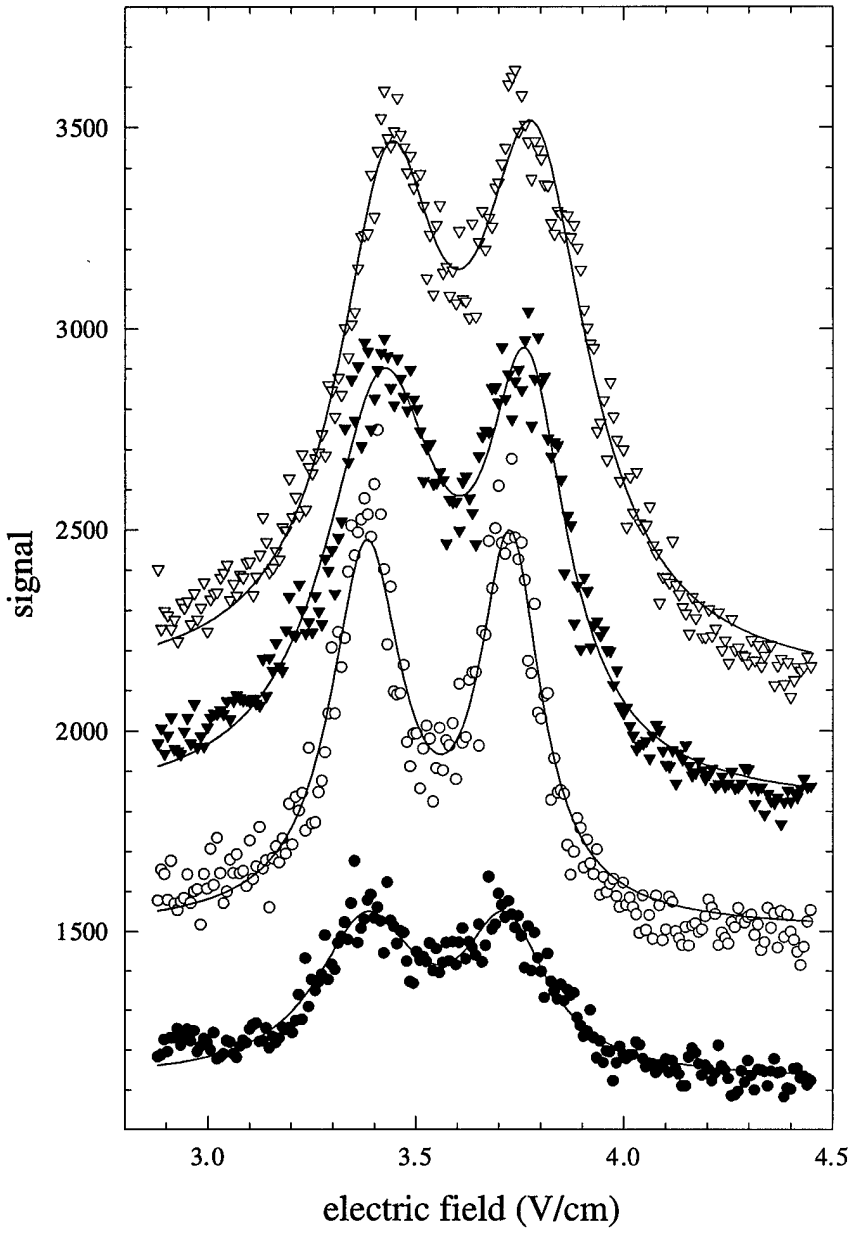

Figure 3.9: Series of resonance scans showing the behavior of the energy transfer resonances as a function of allowed interaction time. The series is taken with a constant initial state atom density of 6.62×10^8 atoms/cc, with no evidence of saturation broadening. The scales are identical for all traces, but each trace is offset for clarity. Solid lines indicate fits to Lorentzian lineshapes. Fit values are shown in Fig. 3.10. The traces are offset for ease of viewing, and the allowed interaction times are, from bottom to top: 81 ns, 360 ns, 650 ns, and 1.78 μs. Peak population transfer for the longest resonance is 17.4±5.6%.

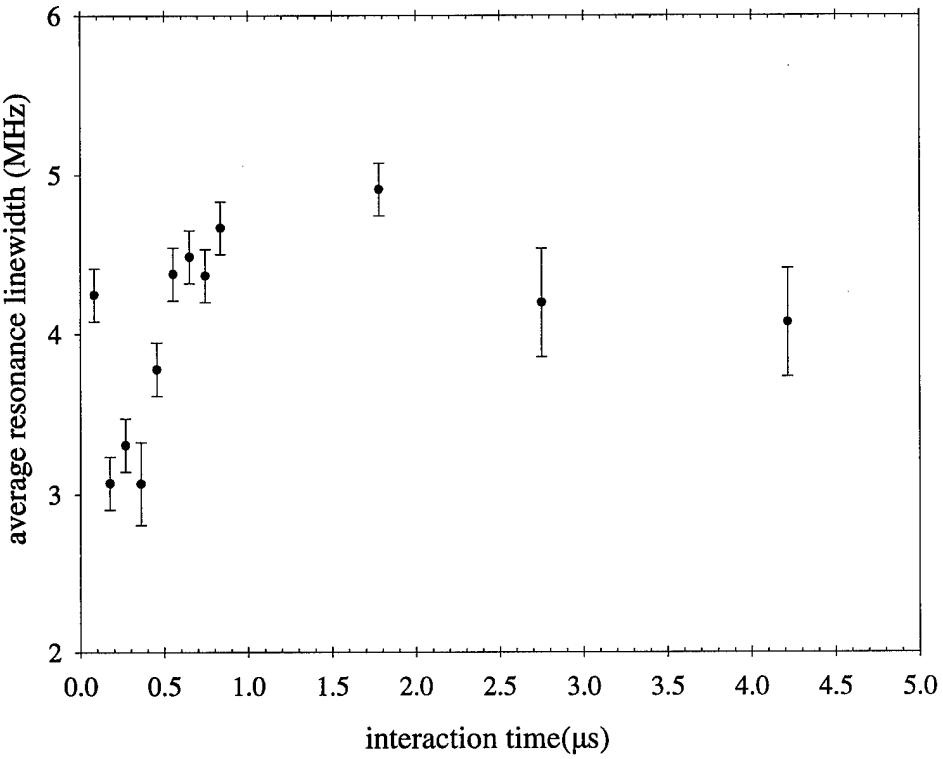

Figure 3.10: Plot of fit values for resonance widths as a function of allowed interaction time. The initial state density for all scans was 6.62×10^8 atoms/cc. The first data point is transform broadened. The increase in the widths at longer times is due to more efficient transfer of p' excitation from closely spaced ss' pairs near resonance.

3.5 Summary

We have shown here how the resonant energy transfer process in a frozen Rydberg gas can be formulated in a quasistatic picture. Specifically, we have demonstrated how couplings between molecular states influence the energy eigenstates of the system. We have investigated the dependance of the frequency characteristics of the interaction on the allowed interaction time and the density of atoms in the initial states. Experimental data demonstrate that this formulation of the interaction is reasonable.

Finally, the dependance of the observed signal on allowed interaction time shows good qualitative agreement with our model. In the next chapter, we will investigate a set of resonances with different characteristics and determine how well the interaction picture we have developed here holds up to the new data.

Chapter 4

A Series of Dipole-Dipole Interactions: n Dependence

4.1 Introduction

In order to further test the model developed in Sec. 3.2, we sought to investigate a resonant interaction with somewhat different characteristics. The interaction discussed in Chap. 3 was selected to minimize any experimental broadening effects, while also yielding the narrowest possible resonances. For this experiment, we chose to focus on determining how changes in the dipole matrix elements affect the characteristics of the interaction process. Additionally, we wanted interactions with large dipole matrix elements. A series of resonant processes met these two criteria. For two Rb atoms this series has the form

$$np_{3/2} + np_{3/2} \rightarrow ns + (n+1)s. \tag{4.1}$$

	Resonance Position in V/cm		
Initial np	$\|m_j\| = 1/2 + 1/2$	$\|m_j\| = 1/2 + 3/2$	$\|m_j\| = 3/2 + 3/2$
26	52.2	55.0	58.4
27	39.7	42.0	44.6
28	30.3	32.0	34.1
29	23.3	24.6	26.1
30	17.9	18.9	20.1
31	13.8	14.5	15.5
32	10.6	11.2	11.9
33	8.1	8.5	9.0

Table 4.1: Resonant Electric Fields for $np_{3/2} + np_{3/2} \rightarrow ns + (n+1)s$ dipole-dipole interactions.

For each n, there is a set of three resonances due to the fine structure splitting of the $np_{3/2}$ level. The experiments discussed in the remainder of the chapter examine the $|m_j| = 3/2 + 3/2$ resonance. The experimentally measured resonant fields for $n = 26$ to 33 are given in Table 4.1. We shall describe this interaction first in terms of a simple quasistatic binary interaction, adopting our conventions from Chapter 3. We recall the detuning from resonance is defined by the energy difference of the initial and final energies of the molecular states, i.e. $\Delta = W_f - W_i = (W_{ns} + W_{(n+1)s}) - (W_{np} + W_{np})$. We also set the energy of the states at resonance to be zero. In this binary picture, two atoms in the initial state are separated by a distance r and the

resonant dipole-dipole interaction strength between the two atoms is given by

$$\chi_{\text{binary}} = \frac{\mu\mu'}{r^3}, \tag{4.2}$$

where μ and μ' are the $np - ns$ (or $p - s$) and $np - (n+1)s$ (or $p - s'$) dipole matrix elements, respectively. These are listed in Table 4.3 (in Sec. 4.3), along with values of χ for a typical nearest neighbor spacing of 1.5 μm.

4.1.1 Multi-atom description of np resonances

Recalling our discussion of Sec. 3.2.1, we realize that the process of Eq. 4.1 is not truly binary in nature, but rather is better described by a multi-atom interaction between molecular states. For a multi-atom system, there are two additional dipole-dipole interactions which are resonant at all electric fields,

$$np_{3/2} + ns \rightarrow ns + np_{3/2}, \text{ and} \tag{4.3}$$

$$np_{3/2} + (n+1)s \rightarrow (n+1)s + np_{3/2}. \tag{4.4}$$

These interactions have strengths between atoms i and j separated by r_{ij} given by

$$\frac{\mu^2}{r_{ij}^3}, \text{ and } \frac{(\mu')^2}{r_{ij}^3}. \tag{4.5}$$

We now seek to formulate the Hamiltonian for a four-atom system, as we did in

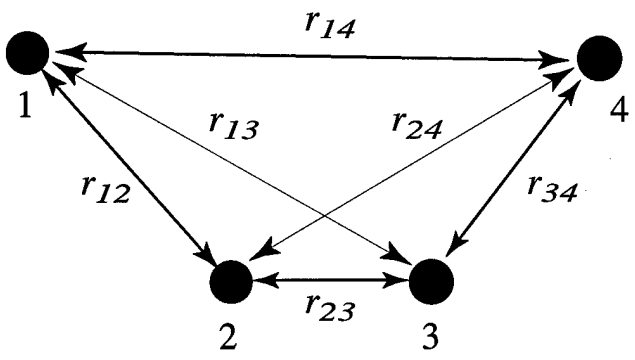

Figure 4.1: Diagram of atoms and typical spacings used in the four atom description of the resonant energy transfer process. The atoms are numbered 1 to 4 from left to right, and are initially all in the p state. The distances in microns between atoms are: $r_{12} = 2.3$, $r_{13} = 3.47$, $r_{14} = 4.3$, $r_{23} = 1.5$, $r_{24} = 3.17$, $r_{34} = 2.1$, and are chosen to represent a typical distribution of neighboring atom spacings.

Sec. 3.2.2. We again assume that we have four atoms at fixed positions in space, with separations as shown in Fig. 4.1. We continue by forming the possible molecular states of the system via the ordered direct product of the wavefunctions of the individual atoms. At this point, we notice a significant difference from the system discussed in Chap. 3; in that experiment, there were four distinct atomic states which took part in the interaction, while here we have only three. This limits the number of possible states of the system, as the two distinct initial atomic states forces a certain symmetry on the molecular wavefunction of the system. The resonant transfer process of Eq. 4.1 (which we can write as $pp \rightarrow ss'$)has no such limitation. This dramatically increases the number of possible molecular states.

Given the experimentally produced initial molecular state of $pppp$, we find there are 19 approximately degenerate molecular states for this system. These are listed

below, grouped by the number of atoms in the p state, and labeled in the ordered basis in which we refer to them (i.e. the molecular state (r) is the 14th element of the basis):

$$(a)pppp, \left\{ \begin{array}{ccc} (b)ppss' & (g)pss'p & (l)sps'p \\ (c)pps's & (h)ps'sp & (m)s'psp \\ (d)psps' & (j)spps' & (n)ss'pp \\ (e)ps'ps & (k)s'pps & (q)s'spp \end{array} \right\}, \text{ and } \left\{ \begin{array}{cc} (r)sss's' & (t)ss'ss' \\ (u)ss's's & (v)s'sss' \\ (x)s'ss's & (y)s's'ss \end{array} \right\}. \quad (4.6)$$

This increased number of molecular states also adds to the number of couplings included in the Hamiltonian. Using the basis defined above, the Hamiltonian becomes:

$$\begin{pmatrix}
-4\Delta & \frac{\mu\mu'}{r_{34}^3} & \frac{\mu\mu'}{r_{34}^3} & \frac{\mu\mu'}{r_{24}^3} & \frac{\mu\mu'}{r_{24}^3} & \frac{\mu\mu'}{r_{23}^3} & \frac{\mu\mu'}{r_{23}^3} & \frac{\mu\mu'}{r_{14}^3} & \frac{\mu\mu'}{r_{14}^3} & \frac{\mu\mu'}{r_{13}^3} & \frac{\mu\mu'}{r_{13}^3} & \frac{\mu\mu'}{r_{12}^3} & \frac{\mu\mu'}{r_{12}^3} & 0 & 0 & 0 & 0 & 0 & 0 \\
\frac{\mu\mu'}{r_{34}^3} & -2\Delta & 0 & \frac{\mu^2}{r_{23}^3} & 0 & 0 & \frac{(\mu')^2}{r_{24}^3} & \frac{\mu^2}{r_{13}^3} & 0 & 0 & \frac{(\mu')^2}{r_{14}^3} & 0 & 0 & 0 & \frac{\mu\mu'}{r_{12}^3} & 0 & \frac{\mu\mu'}{r_{12}^3} & 0 & 0 \\
\frac{\mu\mu'}{r_{34}^3} & 0 & -2\Delta & 0 & \frac{(\mu')^2}{r_{23}^3} & \frac{\mu^2}{r_{24}^3} & 0 & 0 & \frac{(\mu')^2}{r_{13}^3} & \frac{\mu^2}{r_{14}^3} & 0 & 0 & 0 & 0 & 0 & \frac{\mu\mu'}{r_{12}^3} & 0 & \frac{\mu\mu'}{r_{12}^3} & 0 \\
\frac{\mu\mu'}{r_{24}^3} & \frac{\mu^2}{r_{23}^3} & 0 & -2\Delta & 0 & \frac{(\mu')^2}{r_{34}^3} & 0 & \frac{\mu^2}{r_{12}^3} & 0 & 0 & 0 & 0 & \frac{(\mu')^2}{r_{14}^3} & \frac{\mu\mu'}{r_{13}^3} & 0 & 0 & \frac{\mu\mu'}{r_{13}^3} & 0 & 0 \\
\frac{\mu\mu'}{r_{24}^3} & 0 & \frac{(\mu')^2}{r_{23}^3} & 0 & -2\Delta & 0 & \frac{\mu^2}{r_{34}^3} & 0 & \frac{(\mu')^2}{r_{12}^3} & 0 & 0 & \frac{\mu^2}{r_{14}^3} & 0 & 0 & 0 & \frac{\mu\mu'}{r_{13}^3} & 0 & 0 & \frac{\mu\mu'}{r_{13}^3} \\
\frac{\mu\mu'}{r_{23}^3} & 0 & \frac{\mu^2}{r_{24}^3} & \frac{(\mu')^2}{r_{34}^3} & 0 & -2\Delta & 0 & 0 & 0 & \frac{\mu^2}{r_{12}^3} & 0 & 0 & \frac{(\mu')^2}{r_{13}^3} & \frac{\mu\mu'}{r_{14}^3} & 0 & 0 & 0 & \frac{\mu\mu'}{r_{23}^3} & 0 \\
\frac{\mu\mu'}{r_{23}^3} & \frac{(\mu')^2}{r_{24}^3} & 0 & 0 & \frac{\mu^2}{r_{34}^3} & 0 & -2\Delta & 0 & 0 & 0 & \frac{(\mu')^2}{r_{12}^3} & \frac{\mu^2}{r_{13}^3} & 0 & 0 & \frac{\mu\mu'}{r_{14}^3} & 0 & 0 & 0 & \frac{\mu\mu'}{r_{14}^3} \\
\frac{\mu\mu'}{r_{14}^3} & \frac{\mu^2}{r_{13}^3} & 0 & \frac{\mu^2}{r_{12}^3} & 0 & 0 & 0 & -2\Delta & 0 & \frac{(\mu')^2}{r_{34}^3} & 0 & \frac{(\mu')^2}{r_{24}^3} & 0 & \frac{\mu\mu'}{r_{23}^3} & \frac{\mu\mu'}{r_{23}^3} & 0 & 0 & 0 & 0 \\
\frac{\mu\mu'}{r_{14}^3} & 0 & \frac{(\mu')^2}{r_{13}^3} & 0 & \frac{(\mu')^2}{r_{12}^3} & 0 & 0 & 0 & -2\Delta & 0 & \frac{\mu^2}{r_{34}^3} & 0 & \frac{\mu^2}{r_{24}^3} & 0 & 0 & 0 & 0 & \frac{\mu\mu'}{r_{23}^3} & \frac{\mu\mu'}{r_{23}^3} \\
\frac{\mu\mu'}{r_{13}^3} & 0 & \frac{\mu^2}{r_{14}^3} & 0 & 0 & \frac{\mu^2}{r_{12}^3} & 0 & \frac{(\mu')^2}{r_{34}^3} & 0 & -2\Delta & 0 & \frac{(\mu')^2}{r_{23}^3} & 0 & \frac{\mu\mu'}{r_{24}^3} & 0 & \frac{\mu\mu'}{r_{24}^3} & 0 & 0 & 0 \\
\frac{\mu\mu'}{r_{13}^3} & \frac{(\mu')^2}{r_{14}^3} & 0 & 0 & 0 & 0 & \frac{(\mu')^2}{r_{12}^3} & 0 & \frac{\mu^2}{r_{34}^3} & 0 & -2\Delta & 0 & \frac{\mu^2}{r_{23}^3} & 0 & 0 & 0 & \frac{\mu\mu'}{r_{24}^3} & 0 & \frac{\mu\mu'}{r_{24}^3} \\
\frac{\mu\mu'}{r_{12}^3} & 0 & 0 & 0 & \frac{\mu^2}{r_{14}^3} & 0 & \frac{\mu^2}{r_{13}^3} & \frac{(\mu')^2}{r_{24}^3} & 0 & \frac{(\mu')^2}{r_{23}^3} & 0 & -2\Delta & 0 & 0 & \frac{\mu\mu'}{r_{34}^3} & \frac{\mu\mu'}{r_{34}^3} & 0 & 0 & 0 \\
\frac{\mu\mu'}{r_{12}^3} & 0 & 0 & \frac{(\mu')^2}{r_{14}^3} & 0 & \frac{(\mu')^2}{r_{13}^3} & 0 & 0 & \frac{\mu^2}{r_{24}^3} & 0 & \frac{\mu^2}{r_{23}^3} & 0 & -2\Delta & 0 & 0 & 0 & \frac{\mu\mu'}{r_{34}^3} & \frac{\mu\mu'}{r_{34}^3} & 0 \\
0 & 0 & 0 & \frac{\mu\mu'}{r_{13}^3} & 0 & \frac{\mu\mu'}{r_{14}^3} & 0 & \frac{\mu\mu'}{r_{23}^3} & 0 & \frac{\mu\mu'}{r_{24}^3} & 0 & 0 & 0 & 0 & 0 & 0 & 0 & 0 & 0 \\
0 & \frac{\mu\mu'}{r_{12}^3} & 0 & 0 & 0 & 0 & \frac{\mu\mu'}{r_{14}^3} & \frac{\mu\mu'}{r_{23}^3} & 0 & 0 & 0 & \frac{\mu\mu'}{r_{34}^3} & 0 & 0 & 0 & 0 & 0 & 0 & 0 \\
0 & 0 & \frac{\mu\mu'}{r_{12}^3} & 0 & \frac{\mu\mu'}{r_{13}^3} & 0 & 0 & 0 & 0 & \frac{\mu\mu'}{r_{24}^3} & 0 & \frac{\mu\mu'}{r_{34}^3} & 0 & 0 & 0 & 0 & 0 & 0 & 0 \\
0 & \frac{\mu\mu'}{r_{12}^3} & 0 & \frac{\mu\mu'}{r_{13}^3} & 0 & 0 & 0 & 0 & 0 & 0 & \frac{\mu\mu'}{r_{24}^3} & 0 & \frac{\mu\mu'}{r_{34}^3} & 0 & 0 & 0 & 0 & 0 & 0 \\
0 & 0 & \frac{\mu\mu'}{r_{12}^3} & 0 & 0 & \frac{\mu\mu'}{r_{14}^3} & 0 & 0 & \frac{\mu\mu'}{r_{23}^3} & 0 & 0 & 0 & \frac{\mu\mu'}{r_{34}^3} & 0 & 0 & 0 & 0 & 0 & 0 \\
0 & 0 & 0 & 0 & \frac{\mu\mu'}{r_{13}^3} & 0 & \frac{\mu\mu'}{r_{14}^3} & 0 & \frac{\mu\mu'}{r_{23}^3} & 0 & \frac{\mu\mu'}{r_{24}^3} & 0 & 0 & 0 & 0 & 0 & 0 & 0 & 0
\end{pmatrix} \tag{4.7}$$

While certainly unwieldy, we can numerically diagonalize this Hamiltonian for a given detuning to determine the energy levels of the system, as we did in Chap. 3.

The results of this calculation for the $26p$ and $30p$ system are presented in Fig. 4.2. The separations used are identical to those listed in Fig. 4.1, and as those used in calculating Fig. 3.5. Several items are of note. First, the increased number of molecular states has led to a much more complicated picture than for the $ss' \rightarrow pp'$

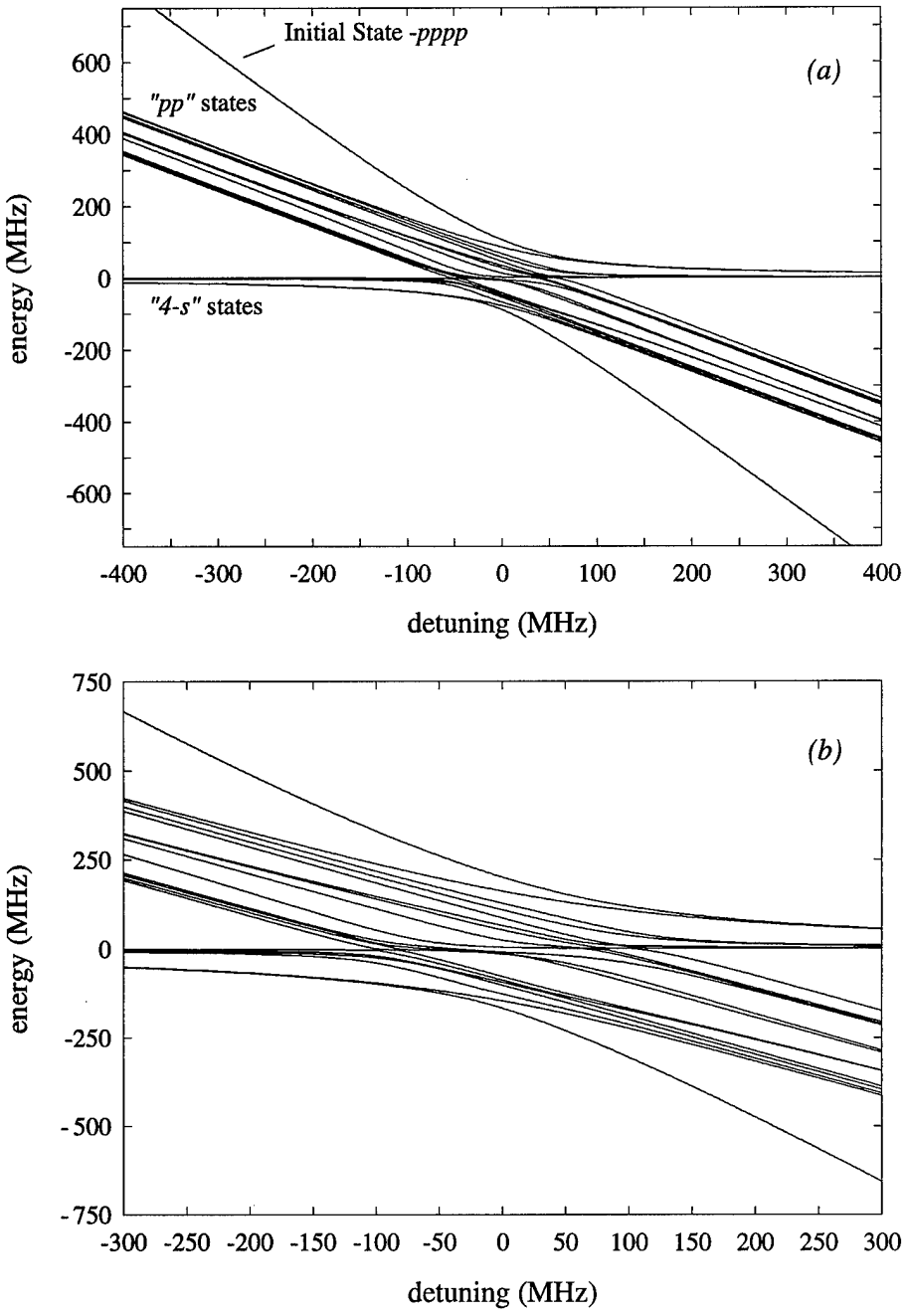

Figure 4.2:
(a) Energy levels of the 4-atom Hamiltonian from the $26p + 26p \rightarrow 26s + 27s$ resonance as a function of detuning from resonance. Spacings used in the calculation are identical to those of Fig. 4.1. *(b)* Same as *(a)*, but for the $30p + 30p \rightarrow 30s + 31s$ resonance.

resonance. However, the initially prepared state (*pppp*) is still somewhat isolated from the remaining states, as was the case for the $ss' \rightarrow pp'$ interaction. The central band of states correspond to the group of 12 states in Eq. 4.6 that have two atoms in the p state, while the states that tend towards zero energy at large detunings are those with no p-state atoms. The width of the crossing is significantly larger than that of Fig. 3.5, as we might expect from the larger dipole moments.

With this picture of the energy resonant dipole-dipole interactions in mind, we now turn our attention to the experimental data. Our investigations in this chapter will focus on several measurements, with the goal of determining how these characteristics of the resonances scale with the principal quantum number n. We repeat our measurements of the resonance widths as a function of density, confirming some of our observations from Sec. 3.4.1. We also measure the signal development on resonance, as in Sec. 3.4.2. We shall start, however, by discussing our measurent of population transfer caused by slewing across the resonance with a ramped electric field.

4.2 Adiabatic Population Transfer

The problem of how a system behaves near an avoided crossing of energy levels was solved independently by Landau and Zener to explain data describing slow atomic collisions[65, 66, 67]. The theory they developed has since been used to describe a wide variety of processes, including field ionization of Rydberg atoms[68, 69] and ionic

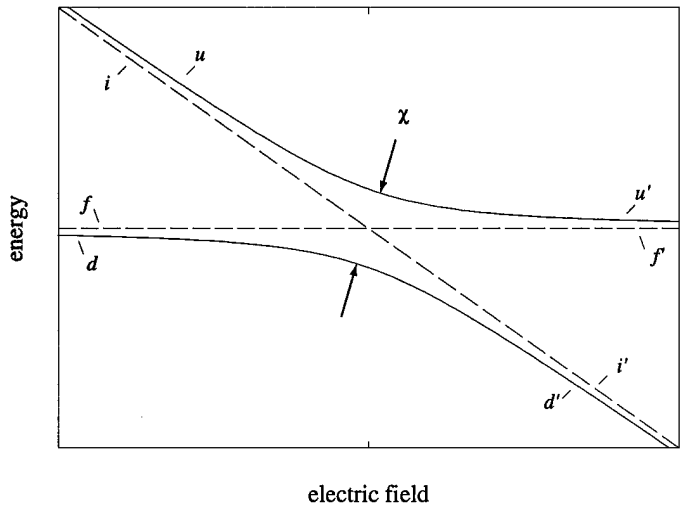

Figure 4.3: Diagram of a representative avoided level crossing. In the absence of any coupling between the two states labelled i and f (dashed lines), they cross at some electric field E_c. The presence of a coupling of strength χ (an off-diagonal term in the Hamiltonian) between the two states removes the degeneracy such that the two levels repel each other. The eigenfunctions of the complete Hamiltonian are labeled u and d (solid lines).

recombination in atomic collisions[70]. The essential result of the theory allows one to determine the magnitude of an avoided crossing by measuring the dependence of the population transfer between states on the rate at which the crossing is traversed. We shall briefly outline the key results of the Landau-Zener theory and then discuss our measurements of population transfer in the resonant dipole-dipole interactions of Eq. 4.1.

4.2.1 Landau-Zener Theory

Landau-Zener theory describes the behaviour of a quantum mechanical system in the presence of an avoided crossing such as the one pictured in Fig. 4.3. In the absence of

coupling, the eigenstates of the system are $|i\rangle$ and $|f\rangle$, which have energies $W_i(E)$ and $W_f(E)$. These are often called the asymptotic states of the system. With coupling of strength $\chi = 2|\langle i|V|f\rangle|$, the Hamiltonian may be written as

$$H(E) = \begin{pmatrix} w_i(E) & \frac{\chi}{2}e^{-i\phi} \\ \frac{\chi}{2}e^{i\phi} & w_f(E) \end{pmatrix}, \tag{4.8}$$

where

$$w_i(E) = W_i(E) + \langle i|V|i\rangle \ , \tag{4.9}$$

$$w_f(E) = W_f(E) + \langle f|V|f\rangle \ , \text{ and} \tag{4.10}$$

$$\frac{\chi}{2}e^{-i\phi} = \langle i|V|f\rangle \ . \tag{4.11}$$

By diagonalizing this Hamiltonian, we obtain the energies of the new eigenstates $|u\rangle$ and $|d\rangle$. We are interested in calculating the probability of remaining on curve $|u\rangle$ (i.e. moving from u to u') as the field is changed from one side of the avoided crossing to the other. If we make a few assumptions (see Ref. [70] for a discussion of these), we can solve the problem in a straightforward manner using the time-dependent Schrödinger equation. The result is known as the Landau-Zener formula, and is given by

$$P(u \to u') = 1 - P(u \to d') = 1 - e^{-2\pi\Gamma}, \tag{4.12}$$

where

$$\Gamma = \frac{\chi^2}{4\left(\frac{dw}{dE}\frac{dE}{dt}\right)_{E=E_c}} = \frac{\chi^2}{4w'\dot{E}}. \tag{4.13}$$

Here we have used the shorthand $w(E) = w_1(E) - w_2(E)$. We henceforth refer to the slew rate dE/dt as $\dot{E}$, and the differential slope at the avoided crossing $(dw/dE)_{E=E_c}$ as w' to simplify the notation.

The basic result can be summed up as follows: the faster the atoms move through the resonance, the more likely they will follow the asymptotic states of the system and traverse the crossing diabatically. If the atoms move through the crossing slowly enough, they will remain on the curve $|u\rangle$ and traverse the crossing adiabatically. Another important point of note is that if we measure the fractional population transfer from one state to another as a function of the crossing traversal rate (or slew rate), we can extract information about the coupling strength, χ, using Eq. 4.12. The advantage of this method of measuring the interaction strength is that we have avoided any potential inhomogeneous broadening effects, as we are simply following the adiabatic energy levels of the coupled system. For a two level system, the process is relatively straightforward, as we have shown. Now we turn our attention to our experiment, in which we measure the population transfer as a function of the slew rate across the resonant dipole-dipole interactions described by Eq. 4.1 and pictured in Fig. 4.2

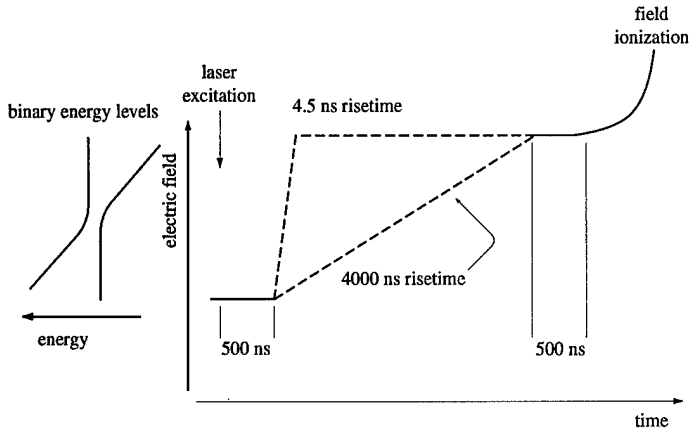

Figure 4.4: Timing diagram for the population transfer measurements. The electric field starts at a value below the resonant field. After laser excitation to the initial state, the field is linearly ramped through the resonant field, and the population field ionized. The maximum and minimum risetimes used are shown. The simplified energy levels are shown as a guide to the size of the pulse, which was a minimum of 5 times the width of the resonance measured in Sec. 4.3.

4.2.2 Population Transfer Measurements

The energy resonance we studied, which for two atoms has the form given by Eq. 4.1, was observed in a magneto-optical trap, as described in Chap. 2. The Rb atoms in the trap were excited from the ground $5s_{1/2}$ state to the $5p_{3/2}$ state via the trapping lasers. From there, the atoms were excited to the $np_{3/2}, |m_j| = 3/2$ Rydberg state using a doubly-amplified short cavity Littman-style pulsed dye laser (see Sec. 2.3.1), similar to the process shown in Fig. 2.5. The final excitation process is done at an electric field slightly below the resonant field.

We then produce the electric field pulse which takes us through the resonant electric field, in a manner similar to that shown in Fig. 4.4. The linear risetime pulse is produced by a Hewlett-Packard 8112A pulse generator, and is connected to

the field plate closest to the detector (see Sec. 2.3.2 and Fig. 2.10). The atoms are selectively field ionized and the resulting ions detected with a microchannel plate detector. The field ionization pulse ionizes atoms from all three states involved in the resonance process. The ion signals are amplified and monitored with a Tektronix 2440 oscilloscope, which averages the signals from 256 shots of the laser and downloads the resulting trace to a computer. The areas under the curves for the np and ns states were numerically integrated and the resulting signal levels used to calculate the fractional population transfer. Several averaged traces were collected for each slew rate. For each data point collected at a given slew rate, a nominial "background" trace was collected using a 4.5 ns risetime pulse. This was used to monitor the initial state population relative to other data sets.

Figure 4.5 shows two traces taken with pulse risetimes of 4.5 ns and 4.0 μs. The increase in $26s$ population with the longer risetime (slower slew rate) is quite noticeable, as is the appearance of signal due to the $27s$ state, despite its partial overlap in time with the $26p$ signal. We desire to measure the fractional population transfer, denoted here as Q, as a function of electric field. We determine this fraction experimentally by measuring

$$Q(\dot{E}) = \frac{N[ns] + N[(n+1)s]}{N[np] + N[ns] + N[(n+1)s]}, \tag{4.14}$$

where $N[n\ell]$ represents the integrated signal due to the state $n\ell$. Since the np and

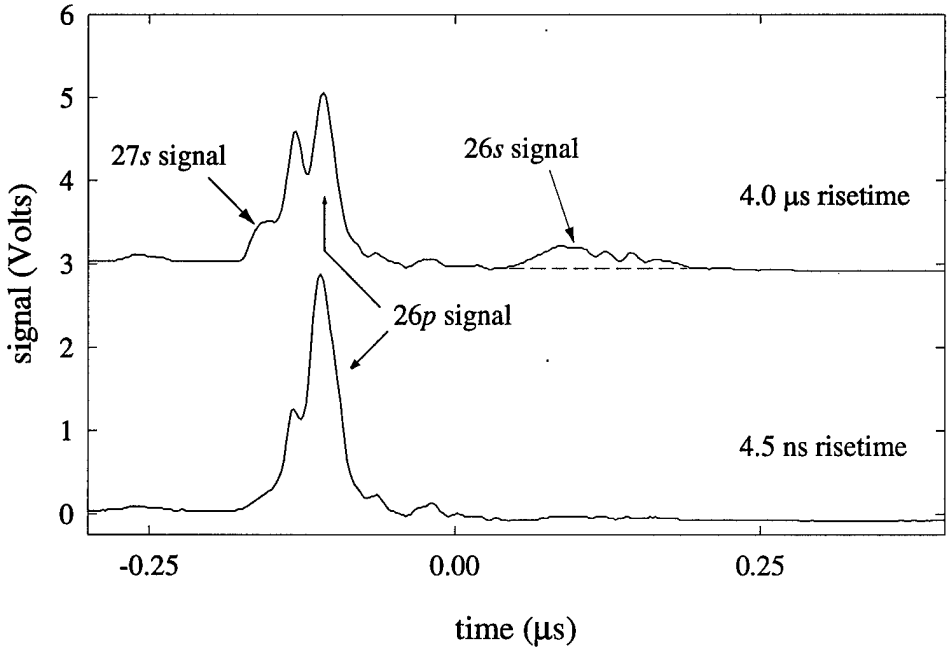

Figure 4.5: Sample oscilloscope traces to illustrate the measurement of population transfer. The top trace was taken with a 4.0 μs risetime pulse, while the lower trace had a 4.5 ns risetime pulse. The peaks are labeled by state, with the dotted line below the $26s$ state signal is meant to demonstrate the time extent of its signal. The area under each curve is measured to determine the fractional population transfered from the $26p$ state. These traces are taken at the highest density measured.

$(n+1)s$ signals are partially overlapped in time, we measure these two signals together, and the ns signal separately. Noting $N[ns] = N[(n+1)s$ from detailed balance, we then find

$$Q(\dot{E}) = \frac{2N[ns]}{N[ns] + \{N[np] + N[(n+1)s]\}} \tag{4.15}$$

The outcome of a set of measurements for $n = 26$ is shown in Fig. 4.6. The small circles on the left hand side are the population transfer measurements from the 4.5 ns risetime background data. Their mean value, effectively the minimum measurable population transfer Q_{min} due to black body radiation induced tranfer, is represented

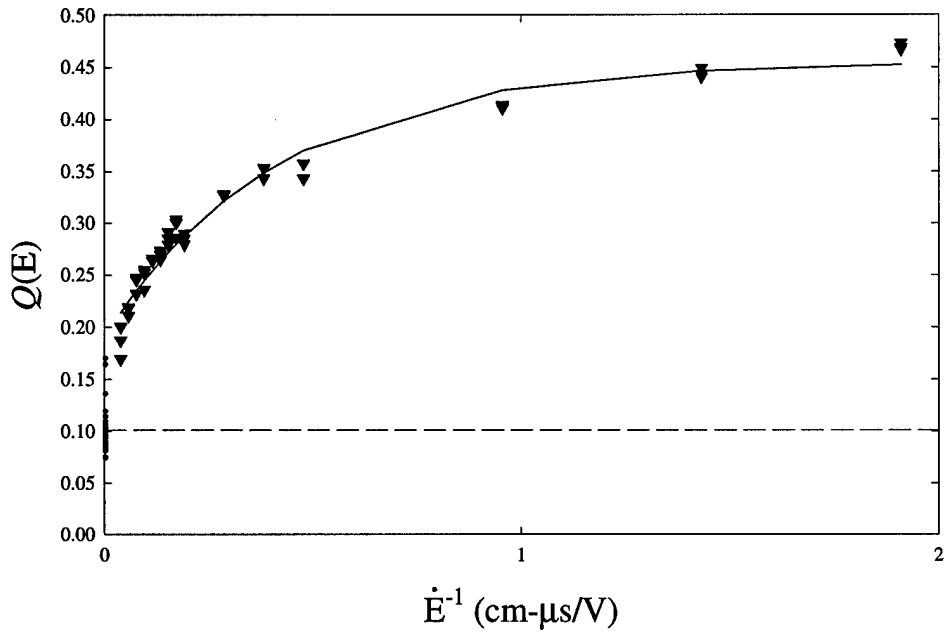

Figure 4.6: Slew rate dependence of population transfer for $26p$ data at the highest measured density. The data are plotted against the reciprocal slew rate. The triangles represent individual data points. The solid curve represents a fit to Eq. 4.16 modified with a fixed baseline offset, while the dashed line is the average of the population transfer for the highest slew rate. The small circles are the background data measurements, whose mean is used to determine the nominal zero transfer, here at $Q \approx 0.1$, denoted by the solid line.

by the dashed line. The solid curve represents a non-linear least-squares fit to the function

$$Q(\dot{E}) = Q_{\max} - \eta \exp\left\{-\frac{\pi\kappa^2}{2w'\dot{E}}\right\}, \tag{4.16}$$

in which $Q_{\max}$ is allowed to vary to account for maximum population transfers which are less than one (typical values are about 0.4), while η accounts for the non-zero minimum population transfer.

Several possible functional forms were attempted before we decided on Eq. 4.16. A strict Landau-Zener function (i.e. Eq. 4.12) was unable to deal with the limited change

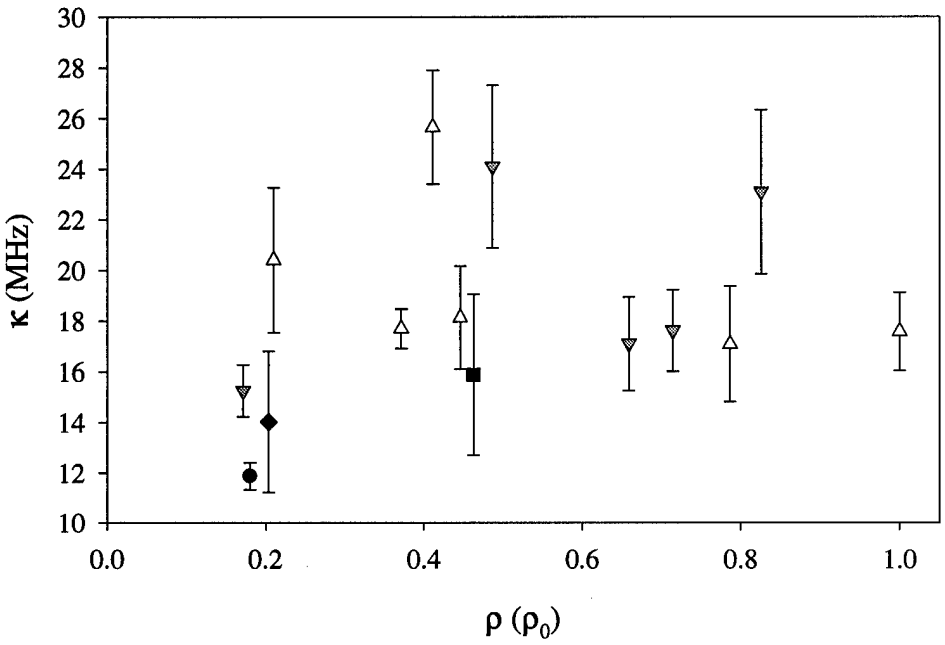

Figure 4.7: All measured values for the fit parameter κ from Eq. 4.16 as a function of n and the relative density ρ. The symbols represent the following: white triangles, $26p$; black circles, $27p$; black squares, $28p$; black diamonds, $29p$; and grey triangles, $30p$. The data are also presented in Table 4.2.

in Q. We attempted to deal with this by scaling either the maximum probability (from 1 to a variable parameter $Q_{\max}$) or the minimum probability (from 1 to a variable parameter η) independently, but these also systematically resulted in poor fits. Finally, we attempted to fit the data to the average of a set of Landau-Zener probabilities at a scaled set of frequencies. This still resulted in relatively poor fits. As such, we fit the data using the three adjustable parameters above, which resulted in a reasonable representation of all data sets taken.

The fit parameter κ has units of frequency, and in the Landau-Zener model would represent the coupling between the two levels which form the avoided crossing. Given

ρ (ρ_0)	κ MHz	$Q_{\max}$	η	$Q_{\min}$
1.000	17.596 ± 1.5	0.455	0.260	0.101
0.786	17.105 ± 2.3	0.390	0.080	0.273
0.446	18.150 ± 2.0	0.390	0.280	0.056
0.411	25.660 ± 2.3	0.470	0.370	0.147
0.371	17.720 ± 0.8	0.420	0.250	0.071
0.210	20.420 ± 2.9	0.448	0.301	0.069
0.180	11.875 ± 0.5	0.543	0.488	0.045
0.463	15.896 ± 3.2	0.490	0.260	0.169
0.204	14.029 ± 2.8	0.322	0.161	0.101
0.826	23.108 ± 3.2	0.514	0.165	0.311
0.714	17.638 ± 1.6	0.389	0.145	0.220
0.659	17.119 ± 1.8	0.324	0.094	0.192
0.486	24.108 ± 3.2	0.220	0.076	0.131
0.172	15.253 ± 1.0	0.343	0.234	0.068

Table 4.2: Fit parameters κ, η, $Q_{\max}$, and $Q_{\min}$, along with error in determining κ for all $np_{3/2} + np_{3/2} \rightarrow ns + (n+1)s$ population transfer measurements.

the complicated nature of the energy levels as shown in Fig. 4.2, it is unclear exactly what κ physically represents. Despite this, we report the measured values of κ here (as well as $Q_{\max}$ and η), as an effective means of characterizing all data sets taken. We also estimated the error in determining a value of κ which accurately characterized the data for a given set of conditions. The error bars are a gross estimate; we varied the value of κ at a fixed percentage from the measured value, and tried to fit the data varying only the remaining parameters. The values quoted are rounded up from twice the largest acceptable change.

The fit values $Q_{\max}$, η, and κ for all np measurements are given in Table 4.2. There

are several points of note about the data. First, the relative density, ρ/ρ_0, is found by dividing the measured average initial state signal, taken from the background scans at a given set of conditions, by the effective volume of the interaction region. The resulting value is then scaled to a reference density. The reference density was taken by saturating the signal from the $26p$ inital state at a trap density of 7.52×10^9 atoms/cc with a diameter of 1.161 mm. The effective volume of the interaction is given by the intersection of the cylinder formed by the waist of the pulsed dye laser and the sphere of the trap. Second, the maximum measured population transfer for all data was 0.58, taken with a 9 μs risetime pulse, or at a slew rate of $\dot{E} = 0.233$ V/(cm·μs). Finally, the data for κ appear to be relatively constant, with all values effectively grouped around a mean value of 18.3 MHz, with little apparent dependence on density or n. This is somewhat surprising, as in a simple binary system, we would expect the coupling to vary linearly with density, due to the r^{-3} dependence of the dipole-dipole coupling. Likewise, we would expect the data to vary with n as the dipole moments vary as n^2, and the dipole-dipole coupling by n^4.

4.3 Scaling of Resonance Widths

In Chapter 3, we demonstrated that the widths of the dipole-dipole resonance varied as a function of the density of atoms in the initial state. As a part of our investigation

Initial np	μ (ea_0)	μ' (ea_0)	χ (MHz)
26	614.19	590.67	104.7
27	668.03	642.34	123.8
28	724.13	696.17	145.5
29	782.49	752.16	169.8
30	843.12	810.32	197.1
31	906.00	870.64	227.6
32	971.14	933.12	261.5

Table 4.3: Dipole matrix elements and typical close atom couplings for the $np_{3/2} + np_{3/2} \rightarrow ns + (n+1)s$ resonances.

of the system of dipole-dipole interactions described by Eq. 4.1,

$$np_{3/2} + np_{3/2} \rightarrow ns + (n+1)s,$$

we measured the widths of these resonances as a function of the initial state density. We hope to ascertain n scaling from the data. We expect to see the widths of the resonances change as a function of n, if only due to the changes in the dipole matrix elements, shown in Table 4.3. It is clear from Fig. 4.2 that the energy level spacing for the $30p$ resonance is noticably larger than for the $26p$ resonance, lending credence to this notion.

We chose to focus on two of the resonances, $n = 26$ and $n = 30$, for the measurements. Below $n = 26$, the resonances are at high enough fields that we expect to have problems resolving much change in the linewidth due to broadening from electric

field inhomogeneity. We have measured the field homogeneity to be $\Delta E/E = 0.003$, which implies a minimum measurable width for $n = 26$ of ~ 68 MHz. Above $n = 30$, the resonance fields are sufficiently low to make excitation into the $np_{3/2}, |m_j| = 3/2$ state extremely difficult. There are two reasons for this: first, there is less d-character in the np state at low electric field, and hence less oscillator strength for optical excitation into that state; second, we are unable to resolve the individual $|m_j|$ sublevels with the laser at the resonant fields for the systems above $n = 30$, which means we lose half of the population we produce into the wrong $|m_j|$ sublevel. We also focused on these levels to complement the population transfer data taken in Sec. 4.2.

The experiment is essentially the same as that outlined in Sec. 3.3, with a few minor modifications. As in the last section, the initial state excitation is performed in an electric field. After allowing the atoms to interact for 3.5 μs, we terminated the interaction time with a 4.5 ns risetime pulse of 1.5 to 2 V/cm. At fields below resonance, it is possible we might see small amounts of population transfer to the final states as we cross the resonance, while at fields above the resonance, this pulse simply takes us further from resonance. This effect was most pronounced in the $26p$ data. We control the value of the electric field with a digital-to-analog converter and sweep it across the resonance, averaging the signal at each field over many shots of the laser.

Representative data scans for the $30p$ resonance are shown in Fig. 4.8. The data are taken at relative densities of $0.659\rho_0$ and $0.357\rho_0$ for the top and bottom scans,

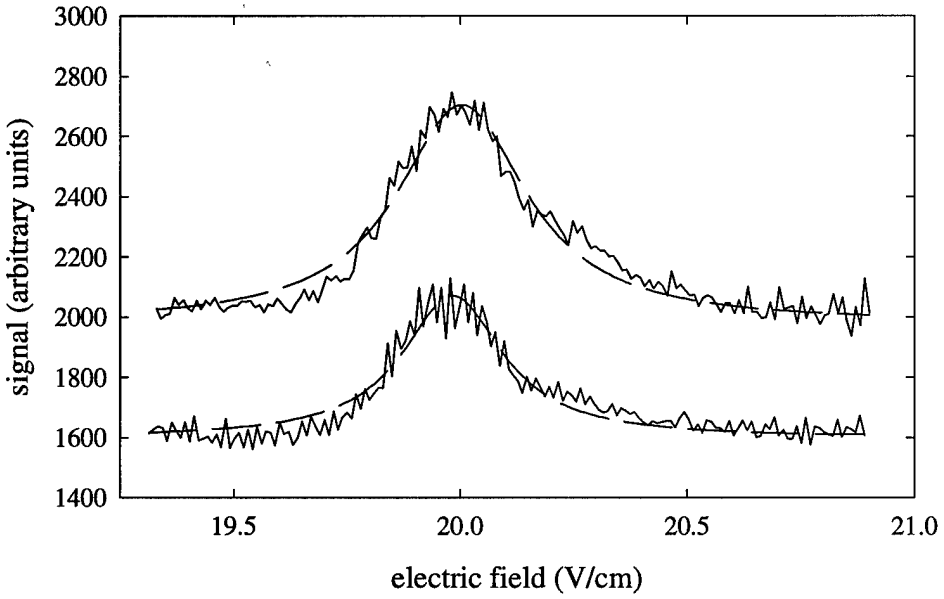

Figure 4.8: Two scans of the $30p$ resonance. These are taken at relative densities of $0.659\rho_0$ (top) and $0.357\rho_0$ (bottom). The dashed lines are the best fits to Lorentzian lineshapes, and have widths of 0.701 Volts (127.9 MHz) and 0.517 Volts (94.3 MHz), respectively. The curves are offset for clarity, and the peak population transfers are 34±15% and 30±15%, respectively.

respectively. The dashed lines indicate fits to a single Lorentzian lineshape

$$f = y_0 + \frac{\alpha}{1 + \left(\frac{E-E_r}{\beta}\right)^2}, \tag{4.17}$$

where α is the area under the peak, E_r is the resonant field, y_0 is an offset to account for the baseline signal level, and β is the FWHM of the peak. We can convert β into energy units using the differential slope of the energy levels, given by $w' = (dw/dE)_{E=E_c} = 182.4$ MHz/(V/cm) for the $30p$ system, and $w' = 204.5$ MHz/(V/cm) for the $26p$ system. The fit values for β in Fig. 4.8 are 0.701 (top) and 0.517 Volts, corresponding to energy widths of 127.9 and 94.3 MHz. The lineshapes shown are

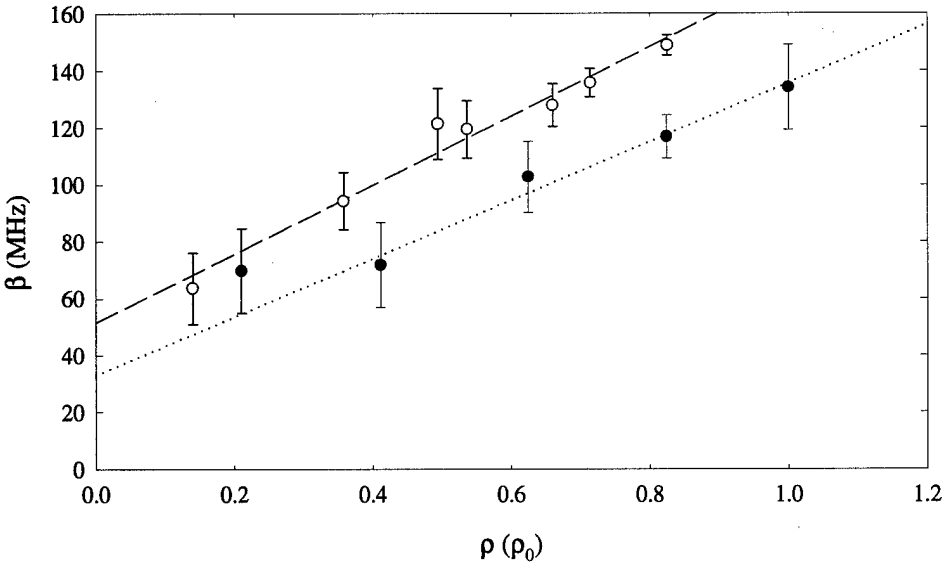

Figure 4.9: Density scaling of resonance widths for $n = 26$ (black circles) and 30 (open circles). All densities are scaled relative to the highest measured density. The dashed line represents a linear fit to the $30p$ data, with $\beta_0 = 51.5$ MHz, and a slope of 121 MHz/(unit relative density). The dotted line is a fit to the $26p$ data, with values 55.5 MHz and 79.3 MHz/(ρ_0), respectively.

typical in that they are noticeably asymmetric. A possible explanation for this effect is that the experimentally produced molecular state changes character as we move across the resonance. Recall that two aligned dipoles will repel each other, while two anti-aligned dipoles attract. At fields below the resonance, we excite atoms to the rupulsive molecular state; avove the resonance, we excite to the attractive state. It is conceivable that the repulsive potential will see a small decrease in the rate at which the $pp \rightarrow ss'$ transition occurs relative to the attractive potential.

The results of all of the measurements made for $n = 26$ (black circles) and 30 (open circles) are shown in Fig. 4.9. The data appear to scale linearly with density, as indicated by the dotted ($n = 26$) and dashed ($n = 30$) lines. The data points are

fit to a linear function

$$\beta = \beta_0 + m(\rho_{rel}), \tag{4.18}$$

where ρ_{rel} is the relative density, and m is the slope of the line in units of MHz/(ρ_0). The slopes and intercepts of these lines are given in Table 4.4, along with the measured linewidths and estimated errors. There were two significant sources of error in measuring the linewidths, in addition to the statistical error due to the fitting procedure. First, for the $n = 26$ data, several of the resonance scans had noticeable population transfer on the low field side of the resonance. This essentially added a shoulder to the line, and increased the error in determining the linewidth for these data. Second, potential inaccuracies in the calculation of the relative density add to the error estimation.

The linear scaling of the width with density is consistent with the expected scaling of all the couplings, but somewhat different than the scaling measured in Chap. 3. This difference could possibly be due to the stark contrast between the energy level pictures offered by our multi-atom interaction models for the two systems, or due to the improved measurement of the relative densities of the initial states in these data.

4.4 On-Resonant Signal Devlopment

We now turn to the development of the resonant signal as a function of the allowed interaction time. As we saw in Sec. 3.4.2, the timescale of the signal growth should tell

n	ρ (ρ_0)	β (MHz)	β_0 (MHz)	m (MHz/ρ_0)
	1.00	134.17 ± 1.50		
	0.82	116.83 ± 0.75		
26	0.62	102.76 ± 1.25	33.0	102.6
	0.41	71.87 ± 1.50		
	0.21	69.76 ± 1.50		
	0.83	148.90 ± 0.35		
	0.71	135.80 ± 0.50		
	0.66	127.88 ± 0.75		
30	0.54	119.53 ± 1.00	51.5	121.0
	0.49	121.43 ± 1.25		
	0.36	94.33 ± 1.00		
	0.14	63.65 ± 1.25		

Table 4.4: Measured values for the resonance widths and density scaling values for the $26p$ and $30p$ dipole-dipole interactions.

us something about the dynamics of the dipole-dipole interaction. For the $ss' \rightarrow pp'$ system we examined in Chap. 3, the difference between the rate of the resonant process and the always resonant "diffusion" processes caused a fast and slow timescale to emerge in the growth signal. Looking at the energy levels of the $pp - ss'$ system shown in Fig. 4.2 and its Hamiltonian of Eq. 4.7, we would not expect to see this type of behavior, as the always resonant couplings are much closer in magnitude to the resonant coupling than the system of Chap 3.

The data are taken in a manner similar to those in Sec. 3.4.2. The initial states were excited in an electric field corresponding to the peak position of the corresponding resonance measured in Sec. 4.3. At a variable time after the arrival of the laser

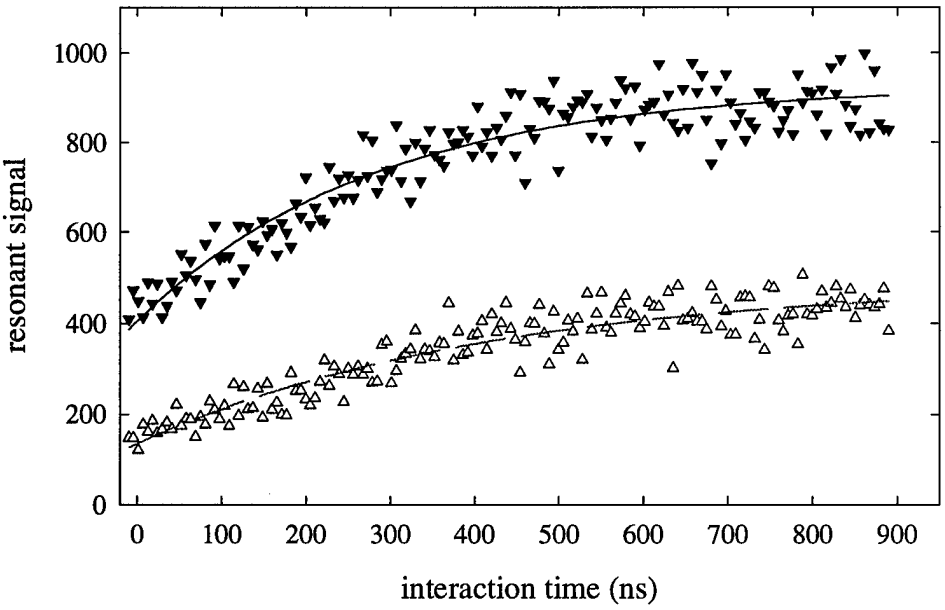

Figure 4.10: Two scans of the on-resonance signal development for the $30p$ resonance. These are taken at relative densities of 0.659 (black triangles) and 0.357 (open triangles). The lines are the best fits to an exponential growth rate, and have values of 3.489×10^6 and 2.415×10^6 s^{-1}, respectively. The two curves are offset for clarity, and the peak population transfers are 35±15% and 30±15%, respectively.

into the interaction region, a 2 V/cm, 4.5 ns pulse was applied to take the system out of resonance. Data were collected and the signal corresponding to each interaction time averaged over many shots of the laser. Two example scans for the $30p$ resonant interaction are shown in Fig. 4.10. The black triangles are the data collected at a relative density of $0.659\rho_0$, while the open triangles are data taken at $0.357\rho_0$. The solid lines are fits to the function

$$f = y_0 + \alpha\left(1 - e^{-\beta_g t}\right), \tag{4.19}$$

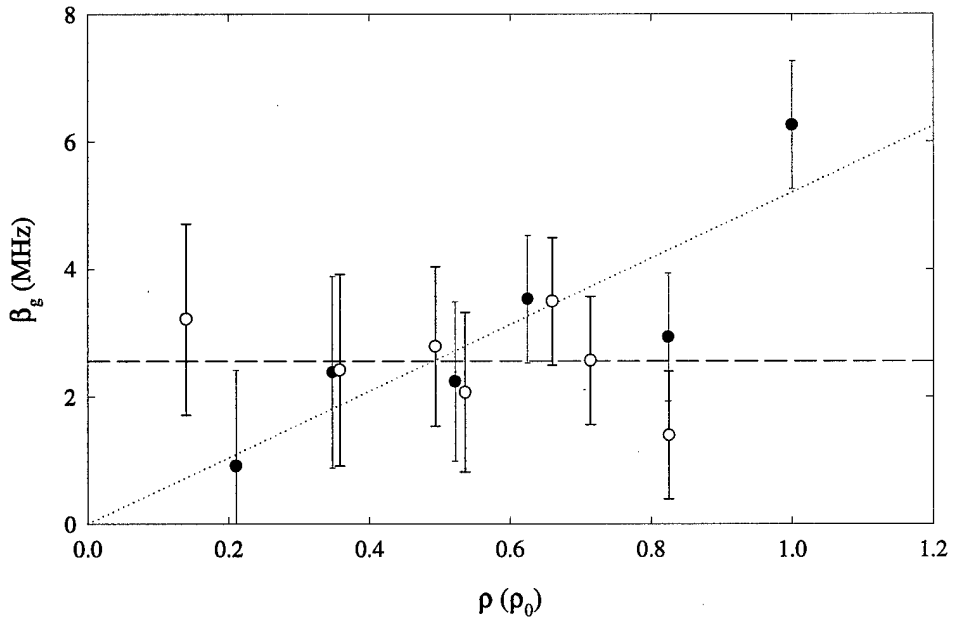

Figure 4.11: Density scaling of on-resonance signal development for $n = 26$ (black circles) and 30 (open circles). All densities are scaled relative to the highest measured density.

where y_0 is the baseline signal, or signal level at $t = 0$, α is the maximum signal height, and β_g is the on-resonance signal growth rate. The fit values for β in Fig. 4.10 are 3.489×10^6 and 2.415×10^6 s^{-1} for the top and bottom curve, respectively. Note that the data are well fit by a single exponential, rather than the two exponentials needed to fit the data in Chap. 3.

The results for all of the measurements made for $n = 26$ and $n = 30$ are presented in Fig. 4.11 and Table 4.5. The data for $n = 26$ show a tendency towards higher growth rate as density is increased, while the data for $n = 30$ are constant. The best fit line for the $n = 26$ data has a slope of 5.21×10^6 $s^{-1}/(\rho_0)$, while the the average value for the $n = 30$ data is 2.56 MHz. The difference in the density scaling of these

n	ρ (ρ_0)	β_g ($\times 10^6$ s^{-1})
	1.00	6.26 ± 100
	0.82	2.93 ± 100
26	0.62	3.53 ± 100
	0.52	2.24 ± 125
	0.35	2.38 ± 150
	0.21	0.91 ± 150
	0.83	1.39 ± 100
	0.71	2.56 ± 100
	0.66	3.49 ± 100
30	0.54	2.07 ± 125
	0.49	2.78 ± 125
	0.36	2.42 ± 150
	0.14	3.21 ± 150

Table 4.5: Measured values for the on-resonant signal growth for the $26p$ and $30p$ dipole-dipole interactions.

values is puzzling, as is the similarity of the measured rates, and bears further study on intermediate values of n. The linear scaling of the β_g with density for the $26p$ resonance is consistent with the expected change in the binary couplings between atoms.

4.5 Summary

In this chapter, we have demonstrated the measurement of adiabatic population transfer in the quasistatic dipole-dipole interactions defined by Eq. 4.1,

$$np_{3/2} + np_{3/2} \rightarrow ns + (n+1)s.$$

We have shown how the application of a quasistatic multi-atom model to this system of resonance leads to a dramatic increase in the number of energy levels in the system. Finally, we further characterized this system of dipole-dipole interactions by measuring the density dependence of the linewidths and on-resonant growth rates for $n = 26$ and 30.

The results of these experiments have been interesting. Our simple binary model of the interactions appears to predict the density scaling behavior for the linewidth and growth rate, but fails to provide us with insight as to the size of the measurements or insight into the adiabatic population transfer measurements. We see that the complex multi-atom model offers potential insight into the difference in behavior of the adiabatic population transfer measurements from the two-level assumption of Landau-Zener theory, but that more study is required to ascertain its role in the observed differences.

Chapter 5

Tensor Polarizability of Rubidium d-states

5.1 Introduction

As discussed in Sect. 2.3, optical transitions are effectively Doppler-free in the MOT. Resonant dipole-dipole interactions are likewise narrowed over thermal measurements, as we have seen in the previous chapters. We can take advantage of this improved resolution to perform measurements of the fine structure splitting in resonances previously temperature broadened, allowing us to investigate resonances at higher n and lower fields.

5.2 Theory

It has long been known that the energy levels of an atom are altered by an electric field[71]. Simply viewed, the presence of an electric field will create an induced

dipole moment in the atom which alters the energy of the charge distribution as (*c.f.* Jackson[12])

$$W = W_0 - \sum_i \frac{1}{2} p_i E_i - \frac{1}{12} \sum_{ij} Q_{ij} \frac{\partial E_i}{\partial x_j} + \cdots, \tag{5.1}$$

where p_i is the induced dipole moment along the i axis, Q_{ij} is the quadrupole moment tensor, and E_i is the electric field along that axis. The induced dipole moment may be written as $p_i = \alpha E_i$, while the quadrupole moment may be similarly parameterized as $\beta(\nabla \mathbf{E})$, a constant value times the gradient of the field. Substituting these values back into Eq. 5.1, we see

$$W_{\text{pol}} = W_0 - \frac{1}{2}\alpha |E|^2 - \frac{1}{2}\beta(\nabla \mathbf{E})^2 + \cdots \tag{5.2}$$

To leading order, our classical calculation predicts the energy shift of a state should be quadratic in field. This is known as the quadratic Stark effect.

A full quantum mechanical treatment of the problem for non-degenerate states involves expanding the Hamiltonian in even powers of the electric field. To leading order, the resulting Hamiltonian for a spin-orbit coupled atomic state in a weak electric field is

$$H = H_{\text{Coul}} + H_{\text{fs}} - \frac{\alpha_0}{2} E^2 - \frac{\alpha_2}{2} E^2 \frac{3m_j^2 - J(J+1)}{J(2J-1)} + \cdots, \tag{5.3}$$

where H_{Coul} represents the Coulomb interaction of the outer (valence) electron

with the remaining ionic core, $H_{\rm fs}$ represents the fine structure Hamiltonian, J is the total angular momentum quantum number, and m_j is its projection along the z-axis. The Coulomb interaction leads to the familiar result that the energy of each state of well-defined ℓ has an energy in zero field of

$$W_{n,\ell} = -\frac{1}{2(n*)^2}, \tag{5.4}$$

where $n* = n - \delta_\ell$ is the effective principal quantum number, and δ_ℓ is the quantum defect of the l state. The fine structure term in Eq. 5.3 may be estimated in Rb by[72]

$$W_{\rm fs}(nd) = \frac{360{\rm cm}^{-1}}{n^3}. \tag{5.5}$$

The expansion above is only valid when the Stark shift of the state is smaller than the energy separation from the adjacent ℓ states. At fields somewhat below this point, however, terms proportional to E^4 and E^6 enter into the expansion.

The two remaining terms in Eq. 5.3, α_0 and α_2, are the scalar and tensor polarizabilities. The scalar polarizability shifts all m_j states by an equal amount, while the tensor polarizability shifts each m_j state by a different amount, splitting the energy level into different sublevels. Khadjavi *et al.* have derived a general expression for these parameters, which relates the polarizabilites to the energy differences between dipole-coupled states and angular factors (6-J symbols). These equations may be

simplified by further assuming that the fine structure splittings are small compared to the separations from adjacent ℓ states, and that the radial matrix elements of the different spin-orbit states of a given ℓ are identical[73] When these assumptions are made, the polarizabilities $\alpha_0(nJ)$ and $\alpha_2(nJ)$ for the nd_J states of Rb are given in atomic units by

$$\alpha_0(n3/2) = \quad \alpha_0(n5/2) = \quad -\frac{4}{15}\mathcal{P} - \frac{2}{5}\mathcal{F} \tag{5.6}$$

$$\alpha_2(n3/2) = \quad \tfrac{7}{10}\alpha_2(n5/2) = \quad \frac{4}{15}\mathcal{P} + \frac{4}{35}\mathcal{F}. \tag{5.7}$$

The terms $\mathcal{P}$ and $\mathcal{F}$ represent the sums

$$\mathcal{P} = \sum_{n'} \frac{|\int R(nd)R(n'p)rdr|^2}{W_{nd} - W_{n'p}}, \tag{5.8}$$

$$\mathcal{F} = \sum_{n'} \frac{|\int R(nd)R(n'f)rdr|^2}{W_{nd} - W_{n'f}}, \tag{5.9}$$

where $R(n\ell)$ denotes the radial wavefunction, and $W_{n\ell}$ the energy of the $n\ell$ state. Taking advantage of Eqs. 5.6 and 5.7, we can simplify notation such that

$$\alpha_0(nd) = \quad \alpha_0(n3/2) = \quad \alpha_0(n5/2), \tag{5.10}$$

$$\alpha_2(nd) = \quad \tfrac{10}{7}\alpha_2(n3/2) = \quad \alpha_2(n5/2). \tag{5.11}$$

With a little thought, we can derive basic information about $\alpha_0(nd)$ and $\alpha_2(nd)$.

The sums in Eqs. 5.8 and 5.9 are dominated by the states nearest the nd state in question. As the energy denominators rapidly increase, the radial matrix elements rapidly decrease with each term. Assuming we are not near a Cooper minimum, the sign of the polarizabilities will be determined by whether the closest states lie above or below the d state in energy. For Rb, the nd state lies just below the $(n+1)p$ state and the nf state. Thus, the denominator of both Eqs. 5.8 and 5.9 will be negative, making $\alpha_0(nd) > 0$ and $\alpha_2(nd) < 0$. The task at hand is to measure tensor polarizabilities, $\alpha_2(nd)$ for a range of nd levels by measuring the splittings of the states.

5.3 Experimental Discussion

We choose to measure the splittings between different $|m_j|$ levels in the nd state of Rb by considering the resonant dipole-dipole interaction

$$nd_{5/2} + nd_{5/2} \rightarrow (n-1)k + (n+1)p_{3/2}, \tag{5.12}$$

for $n = 23$ to 33. We excite the atoms into the intitial state using a single Littman style dye laser, as outlined in Sec. 2.3. The excitation takes place in an electric field, which is varied by a digital-to-analog converter(DAC), and results collected for each set of conditions. Some of the data acquistion made use of the computer program Salsa[6], which averages the entire oscilloscope trace and allows for direct observation

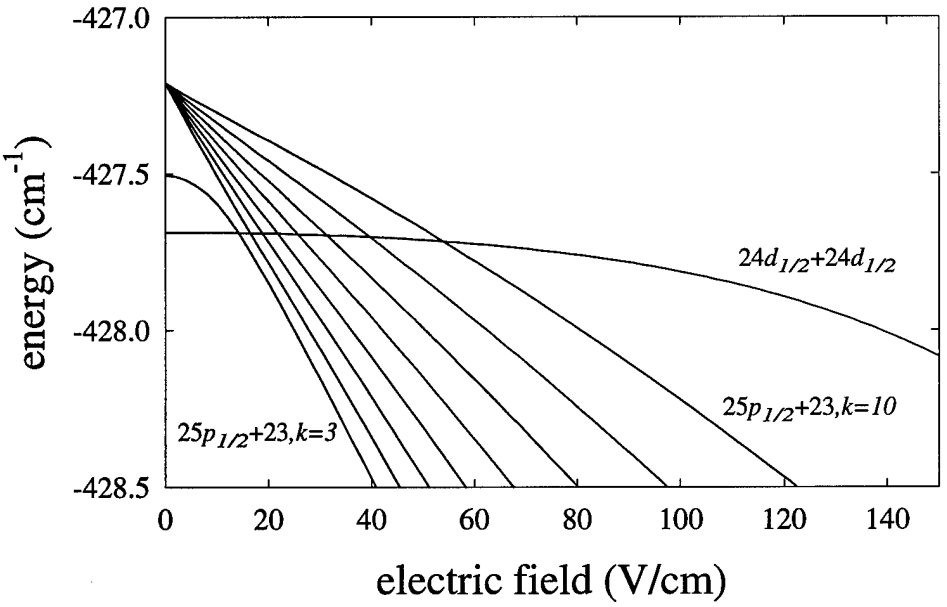

Figure 5.1: Series of dipole-dipole interaction resonances occuring between the $|m_j| = 1/2$ sublevels of the $24d$ and $25p$ states. The upper set of curves are the molecular states $(23, k + 25p)$ for $k = 3$ to 10. The $k = 3$ state is the lowest of that set of curves. The single curve is represents the molecular state $(24d+24d)$.

of variations in the field ionization signal.

If we look at only the $|m_j| = 1/2$ sublevels of the states in Eq. 5.12, we get a series of resonant interactions corresponding to the different $(n-1)k$ manifold states. One of these series is shown in Fig. 5.1. The energies of the composite, or "molecular", states formed by an ordered direct product of the wavefunctions of the initial or final state atoms. This molecular wavefunction is still a solution to the Schrödinger equation, with an energy equal to the combined energy of the two initial state atoms, or the two final state atoms. Fig. 5.1 shows a series of these states as a function of electric field. The resonances occur at the curve crossings. The energy levels were calculated

using the method outlined by Zimmerman[74], in which the Hamiltonian matrix is constructed using the zero-field states as the basis states. Thus the zero-field energies are the diagonal terms of the matrix and the off-diagonal elements are the dipole coupling terms. The off-diagonal terms are of the form $\langle nl|r\cos\theta|n'l'\rangle$; the angular integrals may be evaluated analytically and the radial integrals numerically using the Numerov algorithm. Diagonalizing the matrix determines the energy eigenvalues for a given electric field.

Now let us examine what happens to an individual resonance as we consider the fine structure splittings of the two d states and the p state. The $p_{3/2}$ state will have two fine structure sublevels, $|m_j| = 1/2$ and $|m_j| = 3/2$. Were this the only splitting, we would expect to see a doublet for each resonance. However, we know each $d_{5/2}$ state will have three possible sublevels: $|m_j| = 1/2$, $3/2$, and $5/2$. The initial molecular state should then have six possible non-degenerate sublevels, increasing the number of resonances to twelve for each manifold state.

If we recall Fig. 2.5 and some dipole selection rules for optical transitions in an electric field, we can limit the number of sublevels we populate initially. In an electric field, polarization of the laser parallel to the electric field leads to transitions with $\Delta m_j = 0$, while polarization of the laser orthogonal to the field can only excite transitions with $\Delta m_j = \pm 1$[75]. The trapping lasers which excite the ground state $5s$ atoms to the $5p_{3/2}$ state are circularly polarized, and therefore have polarization components both parallel and perpendicular to the electric field. Thus both $|m_j|$

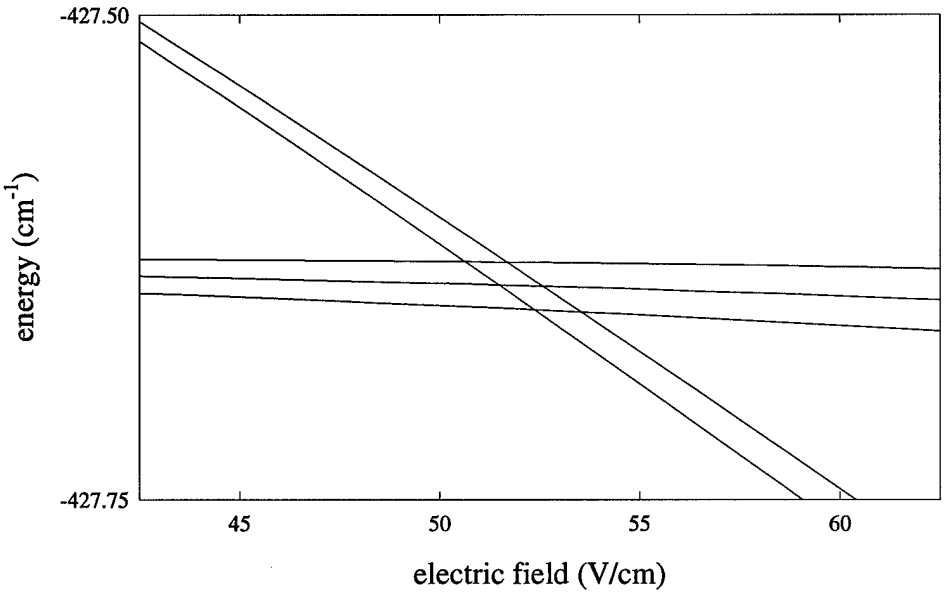

Figure 5.2: Resonances for the system shown in Fig. 5.1 for $k = 9$. Shown are the fine structure sublevels due to the $|m_j|$ splitting in the $24d$ and $25p$ states which form a multiplet structure for the resonance.

sublevels of the $5p_{3/2}$ state will be populated. The Rydberg laser, however, is linearly polarized, and enters the chamber propagating in a direction orthogonal to the electric field in such a way that we may choose its polarization relative to the field. By polarizing the laser parallel to the field, we see from the selection rules above that the laser can only excite atoms into the $|m_j| = 1/2$ and $3/2$ sublevels of the $nd_{5/2}$ state, or into the three molecular states $|m_j| = 1/2, 1/2$, $|m_j| = 1/2, 3/2$, or $|m_j| = 3/2, 3/2$. Remembering that we have no control over the final state, we know we should see a splitting in the final $np_{3/2}$ state. This means there should be six possible resonances for each manifold state, two sets of three, as seen in Fig. 5.2. Observing a set of resonances in a room temperature (300K) collision will show a set of four resonance

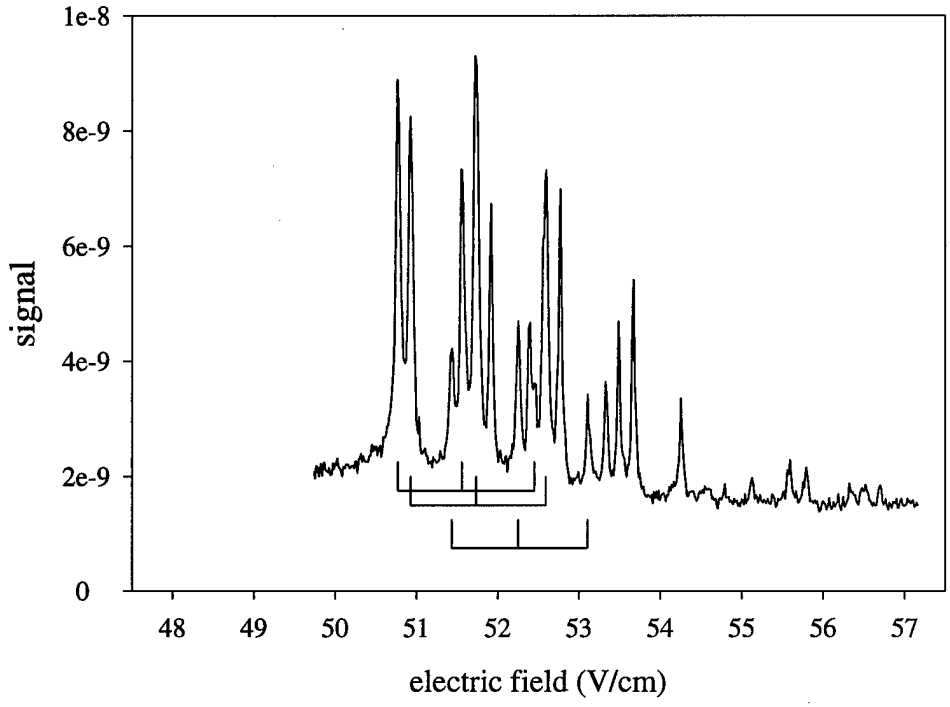

Figure 5.3: Observed resonances for the $24d(|m_j|=\frac{1}{2},\frac{3}{2})$ + $24d(|m_j|=\frac{1}{2},\frac{3}{2})$ $\rightarrow$ 23,9 + $25p(|m_j|=\frac{1}{2},\frac{3}{2})$ dipole dipole interaction. The lines below the data show the resonances which share the same final state which are used to measure the splittings in the $24d$ fine structure sublevels.

peaks consistent with this picture, as observed by Veale[72].

As discussed in the previous chapters, the linewidths of energy resonant dipole-dipole interactions are substantially reduced in a MOT. We would expect, then, to be able to resolve the six individual peaks.

As seen in Fig. 5.3, there are more than 15 individual peaks that we can see. This apparent increase in structure is due to our earlier neglect of the $|m_j|$ sublevels of the $23, 9$ manifold state. The sublevel splitting of the manifold states is rather significant in Rb. In fact, the $|m_j| = 5/2$ manifold states effectively separate into two separate

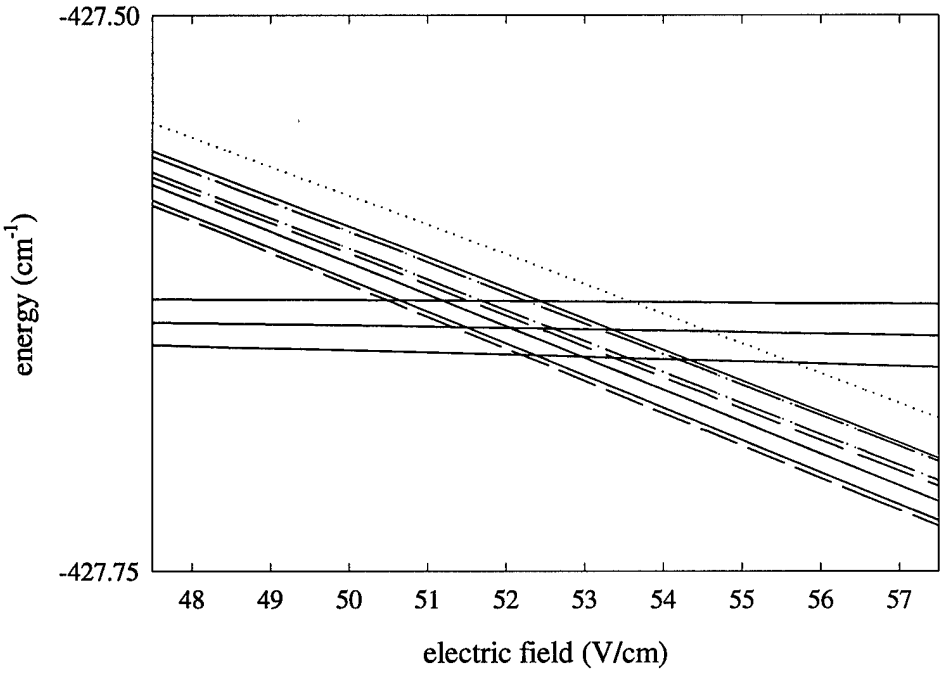

Figure 5.4: Molecular states for the system shown in Fig. 5.1 for $k = 9$. The three solid, nearly horizontal lines are the initial states, while the final states have the large negative slope. Shown are the fine structure sublevels due to the $|m_j|$ splitting in all the atomic states, which form a more complicated multiplet structure for the resonance than seen in Fig. 5.2 The final states are grouped by line type as follows: solid line, $p, |m_j| = 1/2 +$ spin up Stark state; short dashed line, $p, |m_j| = 3/2 +$ spin up Stark state; dotted line, $p, |m_j| = 1/2 +$ spin down Stark state; long dashed line, $p, |m_j| = 3/2 +$ spin down Stark state;

manifolds: one of states with $|m_l| = 3$ which behaves essentially hydrogenic, and one with states of $|m_l| = 2$ which has a larger core coupling and displays the familiar anticrossing behavior[74]. Including the fine structure states of the $23, 9$ manifold state should drastically increase the number of possible resonances.

Looking at Fig. 5.4, we clearly see that inclusion of these sublevels increases the number of potential resonances to 18. The remaining resonances qualitatively agree with the data given the instrumental linewidth, which does not allow us to resolve

peaks closer than about 0.1 V/cm. The stick structure at the bottom of Fig. 5.3 identifies the first three of the six observed triplets with the same final states. Some resonances are identified with two triplets, in which case they were not used in calculating the polarizability.

Given that we have identified the peaks in the multiplet as resulting from fine structure splitting in the initial and final states, we now can measure the splittings between the $|m_j|$ sublevels of the nd states.

5.4 Data Analysis

Several manifold resonances were recorded for each n investigated. Measuring the peak separations for states of known common final states allowed us to determine the $|m_j|$ splitting at a given electric field. Using Eq. 5.3, it is apparent that a measured splitting, ΔE between the $|m_j| = 1/2 + 1/2$ and $|m_j| = 1/2 + 3/2$ states relates to $\alpha_2(nd)$ by

$$\alpha_2 = \frac{10}{3}\frac{\Delta W}{|E_r|^2}, \tag{5.13}$$

The crux of the problem is determining how to convert the measured field splitting into an energy splitting, which is essentially an algebra problem. The energy of the final molecular state at a field E is given by $W_{(p,k)}(E) = W_{(p,k)}(0) - kE - \alpha_p/2E^2$, where α_p is the total polarizability of the np sublevel which is in the final state. The difference in energy between the field of the first peak at a field E_0 and the second

peak, at a field $E_0 + \Delta E$, is given by

$$\Delta W_{(p,k)} = -(k + \alpha_p E_0)\Delta E - \frac{\alpha_p}{2}(\Delta E)^2, \tag{5.14}$$

To find the splitting at E_0, we must subtract out the change in energy change of the second nd sublevel. This energy difference is given by

$$\Delta W_{(nd)} = -2E_0(\alpha_0 + \frac{\alpha_2}{2})\Delta E - (\alpha_0 + \frac{\alpha_2}{2})(\Delta E)^2. \tag{5.15}$$

We see that it is impossible to solve for $\Delta W = \Delta W_{(p,k)} - \Delta W_{(nd)}$ without knowing the value of α_2, as it is given to leading order in ΔE by

$$\Delta W = -(k + \alpha_p E_0 - 2\alpha_0 E_0)\Delta E - \alpha_2 E_0 \Delta E + \mathcal{O}[(\Delta E)^2]. \tag{5.16}$$

We note that the α_2 term is much smaller than the remaining terms, in fact, it is generally less 5% of the other values. We solve for the energy difference by ignoring the term proportional to α_2, and adjusting our error estimate to account for this systematic error in the measurement process. We then calculate α_2 using Eq. 5.13.

We can calculate $W'_{p,k}$ by diagonalization of the Stark matrix as described above. We then make a series of measurements for each n, k combination, and average over the measurements to determine the value for $\alpha_2(nd)$. The number of measurements available decreases the statistical error bars significantly, to typically less than 5% of

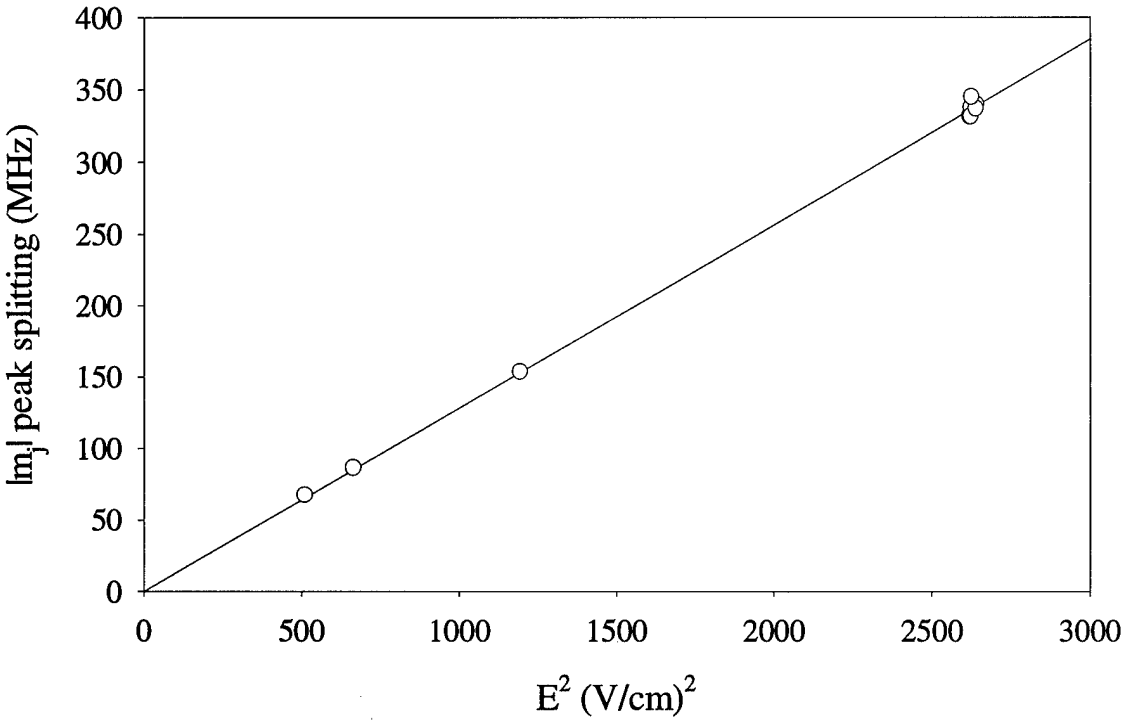

Figure 5.5: Measured energy splittings between $|m_j|$ sublevels for resonances with the $24d$ state. The line is a linear fit through the data points with slope 0.129 MHz/(V/cm)^2.

the measured value, with the highest nd measurements typically having the largest statistical errors. This is due to the limitation that we measure the splittings in fields such that the fine structure splitting is small. We can ensure that we operate in this regime by verifying that the energy splitting is quadratic in the electric field. Figure 5.5 shows that this holds, using data from the $24d$ measurements as an example.

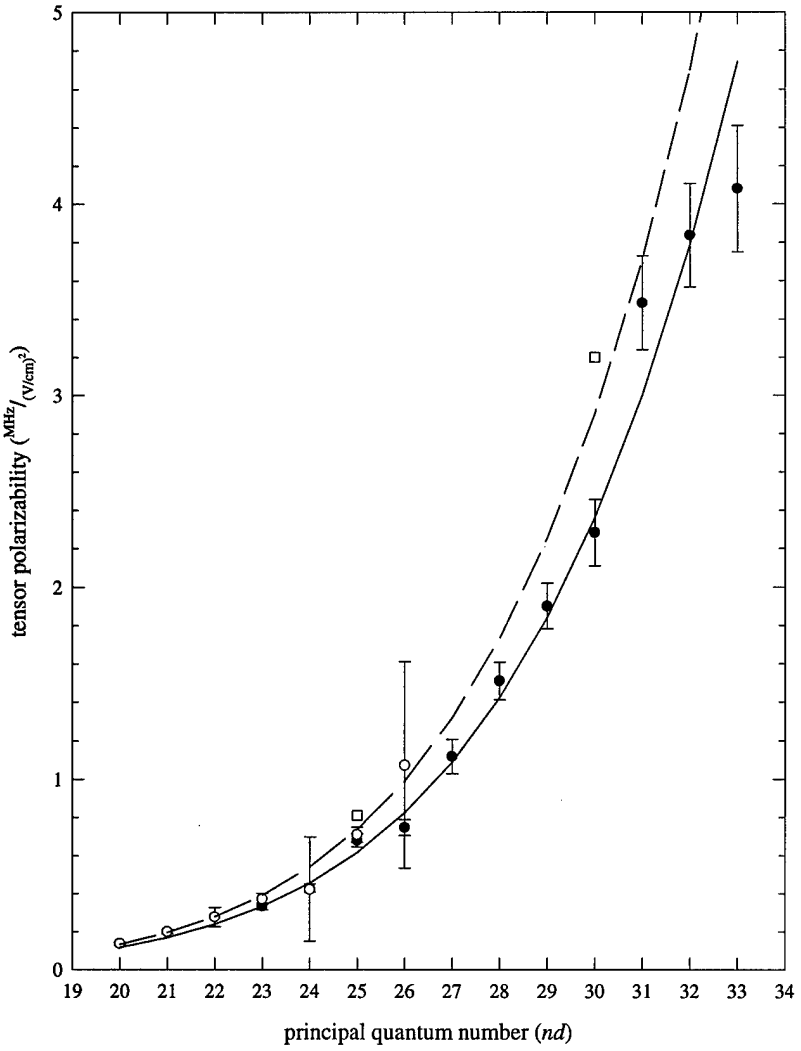

Figure 5.6: Measured values for $\alpha_2(nd)$ with errors. Also shown are the values to a least-squares fit to the data (solid line) and a numerical calculation using Eq. 5.6 (dashed line). Open circles are measurements from Veale[72] with error bars as indicated. Open squares are measurements from O'Sullivan[76].

nd	α_2 (measured)	α_2 (fit)	α_2 (calculated)	From Ref.[72]	From Ref.[76]
23	0.3338 ± 0.0177	0.3324	0.3912	0.373(30)	
24	0.4300 ± 0.0226	0.4559	0.5411	0.423(274)	
25	0.6800 ± 0.0348	0.6169	0.7376	0.710(40)	0.81(1)
26	0.7475 ± 0.0414	0.8243	0.9923	1.073(537)	
27	1.1187 ± 0.0889	1.0889	1.3190		
28	1.5102 ± 0.0980	1.4232	1.7330		
29	1.9018 ± 0.1179	1.8417	2.2550		
30	2.2833 ± 0.1725	2.3617	2.9050		3.2(1)
31	3.4849 ± 0.2441	3.0027	3.7100		
32	3.8364 ± 0.2699	3.7874	4.6990		
33	4.0802 ± 0.3292	4.7417	5.9060		

Table 5.1: Measured values for $\alpha_2(nd)$ with errors. Also shown are the values to a least-squares fit to the data and a numerical calculation using Eq. 5.6, as well as values from Refs. [72] and [76].

5.5 Results

The results of the experiment are presented in Table 5.1 and Fig. 5.6. From Eq. 5.6, we expect that the polarizability of a Rydberg state will scale as $(n^2)^2/(n^{-3}) = n^7$. We performed a least-squares fit of the data to the function $f(n) = a \cdot (n*)^7$, where $n* = n - \delta_l = n - 1.347157$. The fit value for a was 0.1415 Hz/(V/cm)^2.

The data show a consistent offset from measurements by Veale[72] and O'Sullivan and Stoicheff[76], who used a Doppler-free two-photon spectroscopic method, as shown in Fig. 5.6. Reported values from this study are also presented in Table 5.1. This discrepancy could be due to the dependance of the measured energy splitting on the accuracy of the slopes of the final atomic states.

The errors quoted include estimates of several sources of potential error. The first is error caused by inaccuracies in determining the positions of the splittings, such as misidentifying a fine structure peak or poor determination of the peak center. It also includes error caused by not accounting for the differential slope of the $d_{5/2}$ $|m_j|$ sublevels. Finally, it includes the limitation inherent making measurements at lower and lower fields for higher n resonances, such as an inability to resolve all of the fine-structure peaks at the lower field resonances.

5.6 Summary

Measurements of the energy splittings of the $nd_{5/2}$ states of Rb have been made in a MOT, taking advantage of its improved resolution of the narrow dipole-dipole interaction resonances. Data show a consistent offset of 15 to 35measurements of O'Sullivan and Stoicheff. Further study should provide determination of the source of this offset.

Chapter 6

Summary and Future Directions

We have presented the results of a series of experiments investigating resonant dipole-dipole interactions between Rydberg atoms produced in a magneto-optical trap. The extremely low kinetic energies of the atoms implies that during the time of these interactions, they move only a small fraction of their average spacing. As such, we considered the processes to be quasistatic in nature and treated the individual atoms as frozen in space. The long range of the dipole-dipole interaction prompted us to consider the possibility that multiple atoms are involved in the resonance process. The inclusion of these additional atoms and their corresponding couplings introduced significant complexity into our characterization of the system, and appears to cause such observed properties as the broadening of the resonance lines as the density of atoms is increased. We demonstrated measurement of adiabatic population transfer in a series of dipole-dipole interactions, and attempted to characterize the nature of these resonances more completely than had been done to date. These data indicate more clearly the complex, multi-atom nature of the resonances we have observed, and

point to the necessity of further experiments and theoretical work to understand the details of the interactions.

Several intriguing experiments come immediately to mind. The asymmetry in the lineshapes of the $pp \rightarrow ss'$ resonances indicate that one might be able to take advantage of the differing characteristics of the attractive and repulsive molecular states. In essence, one should be able to controllably reduce the collision rate by selectively populating one state or the other. Using radiofrequency fields, one should be able to resonantly switch between the attractive and repulsive states and measure the difference in collision rates. Alternatively, one can run the resonance process we studied in reverse, i.e. compare the properties of the $pp \rightarrow ss'$ interaction with the $ss' \rightarrow pp$ resonant interaction. A further, but much more difficult, experimental possibility entails observing these interactions in an optical lattice. This should have the effect of binning the interatomic spacings in such a manner as to possibly allow one to discern the details of the interactions we have studied.

Bibliography

[1] S. Hawking, *A Brief History of Time: From the Big Bang to Black Holes* (Bantam, New York, 1988), –taken from Introduction by Carl Sagan.

[2] G. Herzberg, *Atomic Spectra and Atomic Structure* (Dover, New York, 1944).

[3] H. A. Bethe and E. A. Salpeter, *Quantum Mechanics of One and Two Electron Atoms* (Academic Press, New York, 1957).

[4] T. F. Gallagher, *Rydberg Atoms* (Cambridge University Press, Cambridge, 1994).

[5] *Rydberg States of Atoms and Molecules*, edited by R. F. Stebbings and F. B. Dunning (Cambridge University Press, Cambridge, 1983).

[6] W. M. Griffith, *Multiphoton Interactions in the Strong Field Regime: Microwave Excitation and Ionization of Rydberg Eigenstates*, Ph.D. thesis, University of Virginia, 1998.

[7] J. A. Dodd, S. J. Lipson, J. R. Lowell, P. S. Armstrong, W. A. M. Blumberg, R. M. Nadile, S. M. Adler-Golden, W. J. Marinelli, K. W. Holtzclaw, and B. D. Green, "Analysis of hydroxyl earthlimb airglow emissions: kinetic model for state-to-state dynamics of OH(v, n)," J. Geophys. Res. **99**, 3559 (1994).

[8] P. S. Armstrong, S. J. Lipson, J. A. Dodd, J. R. Lowell, W. A. M. Blumberg, and R. M. Nadile, "Highly rotationally excited NO(v,J) in the thermosphere from CIRRIS 1A limb radiance measurements," Geophys. Res. Lett. **21**, 2425 (1994).

[9] K. A. Safinya, J. F. Delpech, F. Gounand, W. Sandner, and T. F. Gallagher, "Resonant Rydberg-atom–Rydberg-atom collisions," Phys. Rev. Lett. **47**, 405 (1981).

[10] T. F. Gallagher, "Resonant collisional energy transfer between Rydberg atoms," Phys. Rep. **210**, 319 (1992).

[11] J. R. Veale, W. R. Anderson, M. Gatzke, M. Renn, and T. F. Gallagher, "Line-shape analysis of resonant energy transfer collisions," Phys. Rev. A **54**, 1430 (1996).

[12] J. D. Jackson, *Classical Electrodynamics* (John Wiley & Sons, Inc., New York, 1975).

[13] P. D. Lett, in *The Physics of Electronic and Atomic Collisions, American Institute of Physics Conference Proceedings 360*, edited by L. J. Dubé, J. B. A. Mitchell, J. W. McConkey, and C. E. Brion (AIP Press, New York, 1995), p. 667.

[14] J. D. Miller, R. A. Cline, and D. J. Heinzen, "Photoassociation spectrum of ultracold Rb," Phys. Rev. Lett. **71**, 2204 (1993).

[15] L. P. Ratliff, M. E. Wagshul, P. D. Lett, S. L. Rolston, and W. D. Phillips, "Photoassociative spectroscopy of 1_g, 0_g^+, and 0_g^- states of Na_2," J. Chem. Phys. **101**, 2638 (1994).

[16] W. I. McAlexander, E. R. I. Abraham, N. W. M. Ritchie, C. J. Williams, H. T. C. Stoof, and R. G. Hulet, "Precise atomic radiative lifetime via photoassociative spectroscopy of ultracold lithium," Phys. Rev. A **51**, R871 (1995).

[17] P. L. Gould, P. D. Lett, W. D. Phillips, H. R. Thorsheim, and J. Wiener, "Observation of associative ionization of ultracold laser-trapped sodium atoms," Phys. Rev. Lett. **60**, 788 (1988).

[18] P. D. Lett, P. S. Jessen, W. D. Phillips, S. L. Rolston, C. I. Westbrook, and P. L. Gould, "Laser modification of ultracold collisions: Experiment," Phys. Rev. Lett. **67**, 2139 (1991).

[19] L. Marcassa, S. Muniz, E. de Queiroz, S. Zilio, V. S. Bagnato, J. Weiner, P. S. Julienne, and K. A. Suominen, "Optical suppression of photoassociative ionization in a magneto-optical trap," Phys. Rev. Lett. **73**, 1911 (1994).

[20] M. Walhout, U. Sterr, C. Orzel, M. Hoogerland, and S. L. Rolston, "Optical control of ultracold collisions in metastable xenon," Phys. Rev. Lett. **74**, 506 (1995).

[21] K. A. Suominen, M. J. Holland, K. Burnett, and P. S. Julienne, "Optical shielding of cold collisions," Phys. Rev. A **51**, 1446 (1995).

[22] D. J. Heinzen, in *Atomic Physics 14, American Institute of Physics Conference Proceedings 323*, edited by D. J. Wineland, C. E. Wieman, and S. J. Smith (AIP Press, New York, 1995), p. 369.

[23] T. Walker and P. Feng, in *Measurements of Collisions Beteen Laser-Cooled Atoms*, edited by B. Bederson and H. Walther (Academic Press, San Diego, 1994), Vol. 34, p. 125.

[24] A. Gallagher and D. E. Pritchard, "Exoergic collisions of cold Na*-Na," Phys. Rev. Lett. **63**, 957 (1989).

[25] P. S. Julienne, K. A. Suominen, and Y. Band, "Complex-potential model of collisions of laser cooled atoms," Phys. Rev. A **49**, 3890 (1994).

[26] S. D. Gensemer and P. L. Gould, "Ultracold collisions observed in real time," Phys. Rev. Lett. **80**, 936 (1998).

[27] T. W. Hänsch and A. L. Schawlow, "Cooling of gases by laser radiation," Opt. Commun. **13**, 68 (1975).

[28] D. J. Wineland and H. G. Dehmelt, "Proposed $10^{14}\delta\nu < nu$ laser flourescense spectroscopy on Tl^+ mono-ion oscillator III," Bull. Am. Phys. Soc. **20**, 637 (1975).

[29] D. J. Wineland, R. E. Drullinger, and F. L. Walls, "Radiation-pressure cooling of bound resonant absorbers," Phys. Rev. Lett. **40**, 1639 (1978).

[30] W. Neehauser, M. Hohenstatt, P. Toschek, and H. G. Dehmelt, "Optical-sideband cooling of visible atom cloud confined in parabolic well," Phys. Rev. Lett. **41**, 233 (1978).

[31] W. D. Phillips and H. J. Metcalf, "Laser deceleration of an atomic beam," Phys. Rev. Lett. **48**, 596 (1982).

[32] S. Chu, L. Holberg, J. E. Bjorkholm, A. Cable, and A. Ashkin, "Three-dimensional viscous confinement and cooling of atoms by resonance radiation pressure," Phys. Rev. Lett. **55**, 48 (1985).

[33] E. L. Raab, M. Prentiss, A. Cable, S. Chu, and D. E. Pritchard, "Trapping of neutral sodium atoms with radiation pressure," Phys. Rev. Lett. **59**, 2631 (1987).

[34] C. Cohen-Tannoudji and W. D. Phillips, "New mechanisms for laser cooling," Phys. Today **43**, 33 (1990).

[35] S. Chu, "Laser trapping of neutral particles," Sci. Am. **266**, 70 (1992).

[36] C. C. Bradley and R. G. Hulet, in *Atomic Molecular, and Optical Physics: Atoms and Molecules, Experimental Methods in the Physical Sciences, Volume 29B*, edited by F. B. Dunning and R. G. Hulet (Academic Press, San Diego, 1996), p. 129.

[37] J. Opt. Soc. Am. B **6**, 2020 (1989).

[38] Las. Phys. **4**, 829 (1994).

[39] D. J. Wineland and W. M. Itano, "Laser cooling of atoms," Phys. Rev. A **20**, 1521 (1979).

[40] P. D. Lett, R. N. Watts, C. I. Westbrook, W. D. Phillips, P. L. Gould, and H. J. Metcalf, "Observation of atoms laser cooled below the Doppler limit," Phys. Rev. Lett. **61**, 169 (1988).

[41] J. Dalibard and C. Cohen-Tannoudji, "Laser cooling below the Doppler limit by polarization gradients: Simple theoretical models," J. Opt. Soc. Am. B **6**, 2023 (1989).

[42] A. L. Migdall, J. V. Prodan, W. D. Phillips, T. H. Bergeman, and H. J. Metcalf, "Laser production of a very slow monoenergetic atomic beam," Phys. Rev. Lett. **54**, 2596 (1985).

[43] W. R. Anderson, *Resonant Dipole-Dipole Collisions of Magneto-Optically Trapped Rydberg Atoms*, Ph.D. thesis, University of Virginia, 1996.

[44] C. E. Wieman and L. Holberg, "Using diode lasers for atomic physics," Rev. Sci. Instrum. **62**, 1 (1991).

[45] K. B. MacAdam, A. Steinbach, and C. E. Wieman, "A narrow-band tunable diode laser system with grating feedback, and a saturated absorption spectrometer for Cs and Rb," Am. J. Phys. **60**, 1098 (1992).

[46] W. Demtroder, *Laser Spectroscopy* (Springer-Verlag, Berlin, 1982).

[47] T. Bergeman, G. Erez, and H. J. Metcalf, "Magnetostatic trapping fields for neutral atoms," Phys. Rev. A **35**, 1535 (1987).

[48] F. Gounand, "Calculation of radial matrix elements and radiative lifetimes for highly excited states of alkali atoms using the Coulomb approximation," J. Phys. (Paris) **40**, 457 (1979).

[49] T. W. Hänsch, "Repetitively pulsed tunable dye laser for high resolution spectroscopy," Appl. Opt. **161**, 895 (1972).

[50] M. G. Littman and H. J. Metcalf, "Spectrally narrow pulsed dye laser without beam expander," Appl. Opt. **17**, 2224 (1978).

[51] M. G. Littman, "Single-mode pulsed tunable dye laser," Appl. Opt. **23**, 4465 (1984).

[52] K. Liu and M. G. Littman, "Novel geometry for single-mode scanning of tunable lasers," Opt. Lett. **6**, 117 (1981).

[53] M. G. Littman, "Excimer pumped pulsed tunable dye laser," SPIE Proc. **912**, 56 (1988).

[54] J. D. Corless, J. A. West, J. Bromage, and C. R. Stroud, Jr., "Pulsed single-mode dye laser for coherent control experiments," Rev. Sci. Instrum. **68**, 2259 (1997).

[55] R. C. Stoneman, M. D. Adams, and T. F. Gallagher, "Resonant-collision spectroscopy of Rydberg atoms," Phys. Rev. Lett. **58**, 1324 (1987).

[56] M. J. Renn and T. F. Gallagher, "Ramsey interference fringes in radiatively assisted collisions of K Rydberg atoms," Phys. Rev. Lett. **67**, 2287 (1991).

[57] J. M. Raimond, G. Vitrant, and S. Haroche, "Spectral line broadening due to the interaction between very excited atoms: 'the dense Rydberg gas'," J. Phys. B **14**, 655 (1981).

[58] W. R. Anderson, J. R. Veale, and T. F. Gallagher, "Resonant dipole dipole energy transfer in a nearly frozen Rydberg gas," Phys. Rev. Lett. **80**, 249 (1998).

[59] I. Mourachko, D. Comparat, F. de Tomasi, A. Fioretti, P. Nosbaum, V. Akulin, and P. Pillet, "Many-body effects in a frozen Rydberg gas," Phys. Rev. Lett. **80**, 253 (1998).

[60] H. Margenau and W. W. Watson, "Pressure effects on spectral lines," Rev. Mod. Phys. **8**, 22 (1936).

[61] R. Friedburg, S. R. Hartmann, and J. T. Manassah, "Limited superradiant damping of small samples," Phys. Lett. **40A**, 365 (1972).

[62] J. I. Steinfeld, J. S. Fransisco, and W. L. Hase, *Chemical Kinetics and Dynamics* (Prentice Hall, Englewood Cliffs, 1989).

[63] D. S. Thompson, M. J. Renn, and T. F. Gallagher, "Transform-limited collisions of K Rydberg atoms," Phys. Rev. Lett. **65**, 3273 (1990).

[64] D. S. Thompson, M. J. Renn, and T. F. Gallagher, "Radiatively assisted collisions of K Rydberg atoms," Phys. Rev. A **49**, 219 (1992).

[65] L. D. Landau, Phys. Zh. Sowjetunion. **2**, 46 (1932).

[66] C. Zener, Proc. R. Soc. Lond. A **137**, 696 (1932).

[67] L. D. Landau and E. M. Lifshitz, *Quantum Mechanics: Non-Relativistic Theory*, 3 ed. (Pergammon, New York, 1977).

[68] T. F. Gallagher, L. M. Humphrey, R. M. Hill, and S. A. Edelstein, "Resolution of m_ℓ and m_j levels in the electric field ionization of highly excited d states of Na," Phys. Rev. Lett. **37**, 1465 (1976).

[69] J. R. Rubbmark, M. M. Kash, M. G. Littman, and D. Kleppner, "Dynamical effects at avoided level crossings: A study of the Landau-Zener effect using Rydberg atoms," Phys. Rev. A **23**, 3107 (1981).

[70] D. R. Bates, in *Theoretical Treatment of Collisionss between Atomic Systems*, edited by D. R. Bates (Academic Press, New York, 1962), p. 549.

[71] J. Stark, Ann. d. Phys. **48**, 193 (1915).

[72] J. R. Veale, *Collision Spectroscopy of Rydberg Atoms*, Ph.D. thesis, University of Virginia, 1995.

[73] T. F. Gallagher, L. M. Humphrey, R. M. Hill, W. E. Cooke, and S. A. Edelstein, "Fine-structure intervals and polarizabilities of highly excited p and d states of sodium," Phys. Rev. A **15**, 1937 (1977).

[74] M. L. Zimmerman, M. G. Littman, M. M. Kash, and D. Kleppner, "Stark structure of the Rydberg states of alkali-metal atoms," Phys. Rev. A **20**, 2251 (1979).

[75] D. Suter, *The Physics of Laser-Atom Interactions* (Cambridge University Press, Cambridge, 1997).

[76] M. S. O'Sullivan and B. P. Stoicheff, "Scalar and tensor polarizabilities of ^2D Rydberg states in Rb," Phys. Rev. A **33**, 1640 (1986).